

© 2021 Chenghao Ding

GLOBAL HEAT BALANCE MODEL AND PROBABILITY DISTRIBUTIONS FOR
ATMOSPHERIC RESPONSE

BY

CHENGHAO DING

DISSERTATION

Submitted in partial fulfillment of the requirements
for the degree of Doctor of Philosophy in Nuclear, Plasma, and Radiological Engineering
in the Graduate College of the
University of Illinois at Urbana-Champaign, 2021

Urbana, Illinois

Doctoral Committee:

Professor James F. Stubbins, Chair
Professor Emeritus Clifford E. Singer, Director of Research
Assistant Professor Angela Di Fulvio
Associate Professor Ryan L. Sriver

ABSTRACT

In this work, time series data for global average temperature and ocean heat content are used to calibrate the global heat balance model parameters including climate sensitivity, ocean thermal inertia, and a regional inhomogeneous radiative forcing multiplier.

In this work, separate models are proposed to fit historical natural transients from the El Niño Southern Oscillation (ENSO), volcanic aerosols, and solar variability respectively. Also, a probability distribution of λ , c_{th} , and c_{reg} is found by removing the natural transients out from temperature observations. A new carbon balance model is used to account for departures from equilibrium between atmospheric CO₂ and other reservoirs for anthropogenic carbon emissions. Assuming averages over natural transient effects having zero mean, extrapolation is done to get a probability distribution for future global average temperature.

To my father, mother, and wife for their love and support.

ACKNOWLEDGMENTS

Firstly, I would like to express my deepest gratitude to my advisor, Dr. Singer, for your patience and continuous support throughout my Ph.D. study. This project would not have been possible without your support. Your guidance to my research help me so much that I could not have imagined a better mentor for my Ph.D. study.

I would also like to extend my gratitude to my committee members, Dr. Stubbins, Dr. Sriver, and Dr. Di Fulvio. Your invaluable advice and insightful questions completed this dissertation.

On the other hand, I would like to give thanks to Dr. Perdekamp. He gave me two years' financial support to help me finish my doctoral research. Also, he gave me a lot of suggestions when I worked as teaching assistant in the Physics Department.

My thanks are also for Kristie Stramaski, Becky Meline and Barbara Russell for their help in academic planning and format check of this thesis.

My words will fail to express my heartfelt thanks to my colleagues and friends, Lula Chen, Bei Yang and many other people who have provided countless help, joy, and great company during this journey.

Also, I would like to give most sincere thanks to my parents, Mingyang Ding and Xi-afang Jin. You are the best parents in this world who have provided unconditional love and unswerving courage to me.

Last but not least, I want to give most special thanks to my beloved wife, Jia Zhou. Without your love, understanding, patience, encouragement, I wouldn't have made it this far. Thank you is just not enough to express my gratitude and all the sacrifices you made to help pursue this goal.

TABLE OF CONTENTS

CHAPTER 1	INTRODUCTION	1
CHAPTER 2	BACKGROUND	4
CHAPTER 3	RADIATIVE FORCING	13
3.1	Well-Mixed Greenhouse Gases Radiative Forcing	14
3.1.1	Concentration and Radiative Forcing of CO_2	15
3.1.2	Concentration and Radiative Forcing of CH_4	16
3.1.3	Concentration and Radiative Forcing of N_2O	17
3.2	Contrails, Land Use Change, and Other Well-Mixed Greenhouse Gases	18
3.2.1	Other Well-Mixed Greenhouse Gases	19
3.2.2	Land Use Change	20
3.2.3	Contrails	21
3.3	Volcanoes	22
3.3.1	Large Volcanoes	22
3.3.2	Small Volcanoes	25
3.4	ENSO	27
3.5	Solar Irradiance Variation	28
3.5.1	Grand Minimum, Gleissberg and “Double Gleissberg”	28
3.5.2	Eleven Year Solar Cycle Effects on τ	31
3.6	Historical Adjustable Radiative Forcing	32
3.7	Stratospheric Water Vapor	33
3.8	Radiative Forcing Time Series Data Summary	34
CHAPTER 4	MAXIMUM LIKELIHOOD ESTIMATION	37
4.1	Coordinate Transformation for c_{th} and λ	39
4.2	Corrections to Global Mean Temperature and Ocean Heat Content	40
4.2.1	Corrections to Global Mean Surface Temperature	41
4.2.2	Ocean Heat Content	42
4.3	Prior Probability Distribution for c_{reg}	43
4.4	Integration over Nuisance Parameters	44
4.4.1	Trial Ranges in Orthogonal Coordinates	44
4.4.2	Numerical Integration	45
4.5	Gaussian Fit to Marginal Posterior Probability	48
4.6	3-D Maximum Marginal Probability and Sampling	51

4.6.1	Maximum Marginal Posterior Probability Parameters	52
4.6.2	Random Samples	52
CHAPTER 5 RADIATIVE FORCING AND GLOBAL AVERAGE TEMPERA-		
	TURE EXTRAPOLATIONS	61
5.1	Extrapolate Atmospheric Concentration of Nitrous Oxide and Methane . . .	62
5.2	Extrapolate Atmospheric Carbon Content and Carbon Dioxide Concentration	64
5.3	Major Greenhouse Gases Radiative Forcing Extrapolations	66
5.4	Extrapolations of F and τ for 21 Cases	67
5.5	Cumulative Distribution Function for 98 Samples	68
CHAPTER 6 CONCLUSIONS AND FUTURE WORK		73
CHAPTER 7 REFERENCES		75
APPENDIX A SOLUTION OF GLOBAL HEAT BALANCE EQUATION		81

CHAPTER 1

INTRODUCTION

In the years following recovery of global average temperature from the Santa Maria volcanic eruption in 1902, global average temperature increased by over 1°C . From the Intergovernmental Panel on Climate Change (IPCC) report in 2014 and a recent draft update in 2021, there are lines of evidence that global warming is driven by anthropogenic effects [1, 2].

Emission of greenhouse gases by burning fossil fuel has contributed the most to global warming. People rely on burning coal, oil, and natural gas for electricity and transportation. There have been more than 9 gigatonnes of anthropogenic atmospheric carbon emissions each year since 2010 [3]. The concentration of atmospheric CO_2 has now increased by 30 percent to 410 parts per million (ppm) compared to 1750. However, the 2015 Paris Agreement has reaffirmed the goal of limiting industrial era global temperature increase to well below 2 degrees Celsius, while pursuing efforts to limit the increase to 1.5 degrees. More and more countries have transited energy to replacing fossil fuels with renewable energy sources such as wind and solar energy. While countries like China are taking advantage of nuclear energy as a stable and green energy to cut greenhouse gas emissions, China is nevertheless now the largest emitter of carbon dioxide gas in the world, followed by the United States where a new green deal has been proposed reach a goal of no net anthropogenic carbon emissions by 2050.

However, policy makers can be either too optimistic or pessimistic about climate change because of uncertainty about on much global surface temperature would rise if we keep business as usual or cut emissions from now on. Although varieties of scales of simulations have been done to forecast the future warming trend, large uncertainties still lie in the models. There are many factors affecting the accuracy of estimates of how global average temperature will respond to future changes from atmospheric carbon dioxide and other sources of radiative

forcing and shielding. Here, the term shielding, which is -1 times forcing, is sometimes used when a component of radiative forcing is negative.

In this thesis, I examine this complexity and untangle the human-induced warming from natural variation. A goal is to provide both policymakers and those who must adapt to impacts of global warming a set of formulas for a probability distribution for the future response of global average temperature to changes in radiative forcing.

This work is part of a larger project aimed at examining the implications of climate change, with particular emphasis on implications for energy markets of the depletion of geological resources of fossil fuels and uranium [4, 5, 6, 7, 8, 9]. It updates and replaces a previous examination of probability distributions for climate change outcomes with systematic calibration against historical data [10].

A primary motivation for developing an analytic expression for a joint probability distribution for global heat balance equation parameters is to provide climate change negotiation simulation exercises with estimates of uncertainty of global average temperature extrapolations. A goal is being able to rapidly compute multiple extrapolations based on random samples of a joint probability distribution. Compared to extrapolations using a single set of model parameters [5], this ability will allow investigation of how different simulation participants react to uncertainty estimates. Will some prefer a slower response to policy changes to allow a decade or more [11] for uncertainty to be reduced, while others press harder for prompt action by pointing to the upper end temperature response from samples of the high response end of the probability distribution? If so, what will be the consequences for negotiated policy outcomes?

The methods described here will serve as the basis for future work using updates of probability distributions for historical evolution of contributions to radiative forcing. The working draft IPCC Working Group I Sixth Assessment Report (WG1 AR6) issued in August of 2021 contains impressions of what such updates are likely to look like. However, the draft WG1 AR6 is organized like an extensive review article and lacks full details on annual contributions to radiative forcing and shielding. Thus, for this thesis, literature and data sources available at the time the calculations were done is used. However, WG1 AR6 does contain an extensive summary of relevant literature. Parts of that literature relevant to the

topic of this thesis are summarized in the next chapter.

CHAPTER 2

BACKGROUND

This chapter gives the background for this research topic. It also gives readers a general review about the history and current progress in this research area. Thus, from this chapter, readers will get a basic idea of what are the most difficult challenges and as background for how they will be addressed in the rest of this thesis.

One question that being asked frequently is how global warming will affect nuclear industry globally and in the United States. The 2015 Paris Agreement has set out the target limit of 2 °C warming above pre-industrial levels and in the meantime finding possible ways to curb it further to an increase of 1.5°C. Limiting global warming requires either limiting the total cumulative global anthropogenic emissions of CO₂ and other increases in radiative forcing since the pre-industrial period, using geoengineering methods to limit global warming, or some combination of both. Thus, Singer et al. (2014) [5] examine two approaches to limiting increase of global average temperature to 3°C over a pre-industrial average. (1) Use a transition to approximately 50% of total thermal commercial energy equivalent from nuclear energy to reduce global anthropogenic carbon emissions by 2050 by 50% and then halve them again about every two decades. (2) By applying the solar radiation management (SRM) strategy via continually injecting sulfur into stratosphere, the global average surface temperature can be limited without having to decrease global anthropogenic carbon emissions in the 21st century substantially. However, without SRM, there is very substantial growth in nuclear energy use when and where it remains competitive with other non-fossil-carbon energy sources. The estimated cost of mined uranium nearly doubles from 2020 to 2060. With SRM, the extrapolated wellhead cost of natural gas doubles from 2020 to 2060, to about 4.4 USD₂₀₂₀/GJ, due to depletion of less expensive resources. However, that is not necessarily enough to make nuclear energy competitive for electricity production, especially

in markets within pipeline distance of large now extractable natural gas resources as in the United States. Thus, how on limiting the global average temperature is accomplished can have significant implications for nuclear energy.

Global warming will have different effects in different regions in the world. For example, some coastal cities like New York or San Francisco care more about sea level rising than other inland area like Chicago. Also, more hurricane damage will bring economic loss to cities like New Orleans. Therefore, different stakeholders in the world will have their own thoughts and priorities when facing a carbon cut emission negotiation. However, some regions could even benefit from the climate change which brings loss to other regions. Also, countries like China, which is the current world's largest carbon emitter, has set a goal of net zero carbon emissions by 2060 using massive increases its solar and wind capacity. Other less developed countries don't have the will or the technology necessary to transition from fossil energy to clean energy. Reducing the fossil fuel energy but without equivalent clean energy to fill the gap, the gross domestic product (GDP) must be affected by energy shortage. So, there are uncertainties and problems concerning international cooperation on combatting climate change. Discussions on the funding support and technology consultation on climate change between more developed countries and less developed countries are becoming more and more important. Yang [12] studied the stability against defection of example international agreements on limiting anthropogenic carbon emissions. He accounted for both the impact on economic productivity of climate change and costs of energy decarbonization. In a world divided into sixteen geographic regions, he found no stable agreements that would override incentives for some of the regions to implement SRM before 2060.

Singer and Matchett (2015) [6] report results of simulation experiments with participant groups representing each region in a world divided into six geographic regions. They use physical balance models similar to those of Singer, Milligan, and Rethinaraj (2014) [5] and a simpler economic impact model than used by Yang (2021) [12]. Directed to maximize the net present value of their own region's future GDP, participants in regions more adversely affected by climate change ramped up substantial SRM from 2045–2050.

MacDougall et al. (2020) [13] report results from eighteen simulation models on evolution of atmospheric CO₂ concentrations following a hypothetical future abrupt halt to

carbon emissions. For all of the models, the CO₂ concentration drops gradually after emissions stop, as atmospheric carbon redistributes away from the atmosphere and near-surface ocean. The carbon balance model used in Singer, Milligan, and Rethinaraj [5] contains four different reservoirs for anthropogenic CO₂ emissions into the atmosphere. In that model, the partition of CO₂ between the atmosphere and ocean layers depends only on a physical chemical analysis of solubility. That approach reproduces historically observed increases in prompt retention in the atmosphere of emitted CO₂, but it does not reproduce the results of the MacDoughall et al. exercise. The carbon balance model used by Singer and Matchett (2015) and by Yang (2021) similarly does not reproduce the MacDoughall et al. results.

The IPCC Working Group 1 Fifth and Sixth assessment reports (AR5 and AR6) discuss uncertainties about what they refer to as equilibrium climate sensitivity (ECS), expressed in degrees centigrade. As used in AR5 and AR6, equilibrium climate sensitivity is the industrial era increase in global average temperature for an increase in radiative forcing corresponding to a doubling of the pre-industrial atmospheric carbon dioxide concentration and then relaxation to an equilibrium with that level of radiative forcing. That corresponds to an increase in radiative forcing by a factor of $5.35 \times \ln 2 = 3.71$. There is $1/3.71$ °C of temperature increase per W/m² of radiative forcing of each °C of what these reports refer to as equilibrium radiative forcing. AR5 estimated a likely range of equilibrium climate sensitivity of 1.5–4.5 °C. The term likely means is having a probability somewhere in the range of 66–100%, implying that the probability estimate is itself uncertain. For AR6, the likely range was narrowed to 2.5–4°C. A very likely (90%–100% probability range) estimate from AR6 was 2–5°C.

Before AR6, IPCC the assessments of ECS relied on results from a variety of Earth systems models (ESMs). Multiple runs from a single ESM do provide some indication of uncertainty in ECS because results of multi-decadal runs vary substantially even for the smallest change in initial conditions. The variation of results between models would be no larger if each group followed a precisely reproducible recipe for model construction. The variation in ECS in a multi-model comparison thus depends in part on how much each group departs from a common recipe, and not just on the difference between of physical quantity time-series measurements and model calculations.

AR6 drew on a broader range of inputs than ESM comparison studies to estimate ECS uncertainty ranges. This approach has narrowed the estimated uncertainty range compared to AR5, but the method used to estimate the uncertainty is only described qualitatively in AR6. Part of the uncertainty in ESM is due to uncertainties in radiative forcing estimates. Radiative forcing from CO₂ is the largest component of radiative forcing in absolute value. However, the largest uncertainty range estimates in AR5 and AR6 in W/m² is for tropospheric aerosols.

Reduced complexity climate models are getting attention in assessments of future climate, particularly when combined with economic impact models. Reduced complexity models have advantages in flexibility and computational efficiency, which is very useful when quantifying uncertainty using methods that are potentially independently reproducible. Vega-Westhoff et al. (2019) [14] use the global climate model Hector coupled with a 1-D diffusive heat and energy balance model, i.e. Diffusion Ocean Energy balance CLIMate model (DOECLIM), and a sea-level change module (Building blocks for Relevant Ice and Climate Knowledge; BRICK) that can include contributions from thermal expansion, glaciers and ice caps, and polar ice sheets. There are totally 39 parameters varied in their model. They use global surface temperature, ocean heat uptake, and sea-level change data with prescribed Representative Concentration Pathway (RCP) 8.5 radiative forcing to quantify model uncertainties [14]. They are able to give a tighter constraints on probabilistic projections of global, regional, and local sea-level rise. They found that an upper bound on sea level rise is most affected by climate sensitivity.

Hartin et al. (2015) [15] incorporate a time dependent vertical diffusion model for ocean heating. For shorter-term transient changes in radiative forcing, surface ocean heating and cooling leads to compensating changes in thermal emissions. For longer-term changes in radiative forcing, the temperature perturbation penetrates deeper into the ocean instead of staying near the surface, and there is less compensating change in radiative forcing. Although the dominant underlying physical thermal energy transport process is latitude and longitude dependent advection, the vertical diffusion model allows accounting for the lower global average temperature response from shorter-term transient changes in radiative forcing.

Foster and Rahmstorf [16] examine global mean temperature variation after accounting for three different natural transients: El Niño Southern Oscillation (ENSO), volcanic aerosols, and solar variability. They use a similar approach to Lean and Rind (2008) [17] who use multiple regression analysis on departures response to those factors linear rise with time of global mean temperature.

Lean and Rind (2009) [18] extrapolated global average temperature for five years after the period of their data analysis, accounting for ENSO correlations and solar variability. Over the long term, periods of ENSO and approximately 11 year solar cycle variations vary enough that it is difficult to extrapolate in more detail than the average variability associated with these effects. They show an example of a future repeat of the 1991 Pinatubo volcanic eruption, but do not include a stochastic model future volcanic eruptions.

A flexible but yet accurate volcano model is very useful in this type of analysis. Douglass and Knox (2005) [19] provide a model of the impact of volcanic forcing on global average temperature variation by calibrating historical Aerosol Optical Density (AOD) data, global monthly satellite lower troposphere temperature (TLT) anomaly data, and outgoing long wave radiation data with a first order derivative function with a delay time included in the temperature response. They found the volcano climate sensitivity and response time for the 1991 Mount Pinatubo volcano eruption. This findings implies a negative feedback of Pinatubo to its forcing.

The results in three papers [16, 18, 19] point to an alternative way of separating out the global average temperature effects of short-term transients and gradual evolution over multi-decadal time scales compared to that used in HECTOR. The authors examine and untangle correlations of changes in global average temperature with an index of the ENSO, total solar irradiance (TSI), and changes in aerosol optical depth due to volcanic eruptions. Foster and Rahmstorf provide estimates of proportionality constants between those three parameters and associated temperature changes. They also provide uncertainty range estimates for those parameters. Lean and Rind estimate a four-month lag between ENSO oscillations and changes in global average temperature and a one-month lag between TSI oscillations and global average temperature response. Douglass and Knox provide a detailed analytic analysis of the impact on global average temperate following the 1991 Pinatubo eruption.

The approach used in these papers allows for separating out the global average temperature response to ENSO, the approximately 5.5-year maximum to minimum solar cycle TSI, and large volcanic eruptions. This avoids the need to incorporate a time and space dependent ocean thermal energy transport model in a model designed to extrapolate the response to changes in radiative forcing on a timescale of several decades in the absences of large volcanic eruptions and averaged over responses to ENSO and shorter-term TSI variations.

In combination with results in the Douglass and Knox paper, Ammann and Naveau (2010) [20] provide a mechanism for including a probabilistic model of future large volcanic eruptions in extrapolations of global average temperature, should a need to do that arise. That is of potential interest for extrapolations where anthropogenic stratospheric sulfur injection is reduced in periods of high volcanic aerosol optical depth in order to smooth out impacts on global average temperature. However, volcanic eruptions large enough to have a major impact on global agriculture, like the 1815 Mount Tambora eruption, are rare enough that including a stochastic model of future volcanic eruptions is not likely to be a topic of major interest.

Cheng et al. [21] estimate ocean heat content (OHC) from 1960 to 2015. They found that changes in OHC are relatively small before about 1980. Since then, OHC has increased fairly steadily and, since 1990, has increasingly involved deeper layers of the ocean. They provide the OHC estimate with an unbiased mean sampling error. In their figure 6, they show a total full depth ocean warming of $33.5 \pm 7.0 \times 10^{22} \text{J}$ from 1960 to 2015 with over 87% energy imbalance stored in oceans above 2000m. Compared with IPCC AR5, the new results indicate somewhat greater absorbed energy in ocean during the same period. They also find that the upper ocean is warming more significantly than deeper ocean.

The NASA (National Aeronautics and Space Administration) Goddard Institute for Space Studies has an estimate of global surface temperature change. They provide very useful estimates for global mean temperature changes based on the finding that the correlation of temperature change was reasonably strong for stations separated by up to 1200 km, especially at middle and high latitudes. They have combined land-surface air and sea-surface water temperature anomalies which is called land-ocean temperature index, i.e. L-OTI, for in global average annually relative to 1951–1980 means. From Osborn et al. (2021) [22]

the climatic research unit temperature version 5 (CRUTEM5) global average temperature data estimates are very similar to those from GISTEMP. The CRUTEM5 data also include estimates of percentage of the globe covered by temperature estimates. That is less than 50% before 1905 and ranges from 70% to 86% during the years 1950–2019.

Chan and Huybers (2020) [23] report that the way the sea surface temperatures were measured during World War II (WWII) produced anomalously large estimates of the average of sea surface temperatures globally. Compared to the adjoining years from 1936–1950, all sea surface temperature was estimated to average 0.41°C higher. They conclude that the World War II warm anomaly (WW2WA) is an artifact of observational biases, which is important to be considered when examining decadal variability.

After removing calculated global average change from anthropogenic, solar, and volcanic radiative forcing from the GISTEMP estimates, Schurer et al. [24] report an unforced change in global average temperature of -0.3°C from about 1900 to 1907. This is after attempting to correct for volcanic cooling, which would include that from the 1902 Santa Maria volcanic eruption. They also report an unforced “accelerated warming period,” with a global average temperature anomaly average about $+0.15^{\circ}\text{C}$ from 1937–1944. That is without noting a correction for a WWII sea surface temperature measurement anomaly. They found that deviations $0.022^{\circ}\text{C}/\text{yr}$ slower than the background warming trend from 1880—2000 occurred in about 20% of 5 year periods, 5% of 10 year periods, and only 0.4% of 15 year periods. These results suggest that an analysis that does not account for unforced natural variability other than ENSO will only average over that variability over time scales of less than a decade but may still be useful for extrapolating longer-term trends averaged over that variability.

Using a global circulation model, Sokolov et al. (2009) [25] vary climate sensitivity (S) by varying cloud feedback, ocean thermal inertia by variation an effective vertical diffusion coefficient (K_v) and a multiplier F_{aer} of a specified aerosol loading. They note that “Three properties that are commonly recognized as being major contributors to the uncertainty in simulations of future climate change are the effective climate sensitivity of the system (S), the rate at which heat is mixed into the deep ocean (K_v), and the strength of the aerosol forcing associated with a given aerosol loading (F_{aer}).” They sample a numerically calculated tri-variate posterior probability distribution for those three parameters They show a plot of 400

samples and estimated 90% and 99% confidence contours for the marginal joint distribution for S , and K_v . The mode, mean, and highest edge of the 90% confidence contour in $^{\circ}\text{C}$ are respectively about 2.4, 2.6, and 5.3. The mean and highest edge of the 90% contour for $K_v^{1/2}$ are respectively about 1.6 and 4.2 times the mode. These numbers indicated that the marginal 2-D probability distribution is skewed on the sides of high S and $K_v^{1/2}$, which are positively correlated. These are interesting results, but their complexity and computational burden motivates a search for a more readily reproducible analytic formula for the full tri-variate marginal probability distribution for climate sensitivity, thermal inertia, and efficacy of regionally dependent radiative forcing dominated by tropospheric aerosol shielding.

Marten (2011) [26] discusses the implications of uncertainties in climate sensitivity for extrapolations of three integrated assessment models, FUND (Anthoff and Tol 2010, Anthoff and Tol 2014), DICE (Nordhaus and Boyer 2000 [27]), and PAGE (Hope 2006 [28]). Of these, FUND is of particular interest. That is because it includes probability distributions for two positively correlated parameters related to climate sensitivity and ocean thermal inertia (Anthoff and Tol 2014).

Marten points out the importance of the interaction between physical thermal inertia and economic discount rates in integrated assessment models. Typically, the thermal inertia and economic discounting timescales are both comparable, in the range of a few decades. Thus, discounted net present value and welfare estimates depend not only on an equilibrium approached if radiative forcing is stabilized, but also on the thermal-inertia-dependent path taken to approach that equilibrium.

Ding (2018) [29] reports a maximum likelihood fit for parameters in a global heat balance equation to global average temperature data from 1892—2017. In this work, solar radiative forcing used a three-cosine fit plus two Gaussian functions of time. Volcanic forcing was a continuous function of time based on the temporal derivative of a simple fit to cumulative volcanic radiative shielding. No use was made of the more limited data available at the time on cumulative thermal energy content changes. The global carbon balance model was a simplification of that used by Singer, Milligan, and Rethinaraj (2014) [5]. In view of all of these limitations, no joint probability distribution for global heat balance model parameters was produced. Therefore, in further research reported here, a more complex

model is built to estimate natural transients as well as the uncertainties for model parameters and extrapolation.

CHAPTER 3

RADIATIVE FORCING

Radiative forcing F is estimated in order to solve the following global heat balance equation,

$$c_{th} \frac{d\tau}{dt} = F - \tau/\lambda \quad (3.1)$$

Here F is the difference between radiative forcing (in W/m^2) and radiative forcing in Julian year 1750. τ is the change in global surface mean temperature (in $^{\circ}\text{C}$) from a value that would be in equilibrium with a constant radiative forcing equal to that in 1750. λ (in $^{\circ}\text{C}/(\text{W}/\text{m}^2)$) is called the equilibrium climate sensitivity here. It determines the value the temperature eventually relaxes to if radiative forcing is eventually stabilized. Here c_{th} (in $(\text{W}/\text{m}^2)/(\text{yr}/^{\circ}\text{C})$) is called the thermal inertia parameter. Equation 3.1 tells us how the global surface mean temperature responds to variation of radiative forcing while considering how absorption of excess energy effects oceans. This chapter describes radiative forcing time series estimates and how those estimates are calculated.

IPCC AR5 working group 1 annex-II Table 1 includes the effective radiative forcing (ERF) from 1750 to 2011 for greenhouse gases, ozone (stratospheric and tropospheric), aerosols, land use change, stratospheric water vapor, black carbon on snow, contrails, solar and volcanoes.

Contributions to radiative forcing are divided into two types: slowly evolving and natural transients. Transient effects include impacts on global average temperature due to large volcanic eruptions, changes in global average temperature correlated with the ENSO, and changes in global average temperature correlated with variations in solar irradiance on an approximately 11 year cycle. Before calibrating parameters in the global heat balance equation, the input global average temperature data are corrected by subtracting out the effects on global average temperature from these transients. However, to account for uncertainties

resulting from those natural transients, their temperature responses are multiplied by three different adjustable constants respectively as described in the following chapter. Contributions to more slowly evolving radiative forcing are expressed as differences from their values in reference year 1750. Some anthropogenic contributions to radiative forcing are positive, means that they will cause warming generally. While others are negative, meaning that they will counter the warming trend, such as land use changes albedo effects that reflect more sunlight back to space. Due to uncertainties in the effects of inhomogeneously distributed aerosols, ozone, and black carbon around the globe, an additional adjustable constant c_{reg} multiplying their estimated radiative forcing is included here. Slowly evolving contributions to radiative forcing are added together and then calibrated against the corrected τ by using equation 3.1. This is further discussed in the next chapter.

3.1 Well-Mixed Greenhouse Gases Radiative Forcing

This section describes data sources for historical atmospheric concentrations of CO_2 , CH_4 , and N_2O and how radiative forcing from these gases is calculated. The same method that is introduced in my master thesis [29] is used but with two more years updated: 2018 and 2019. First of all, the exact same Law Dome datasets [30] are used again here. Then, in order to get updates of CO_2 , CH_4 , and N_2O atmospheric concentrations for 2018, and 2019, the most recent National Oceanic and Atmospheric Administration (NOAA) annual greenhouse gas index measurements of CO_2 , CH_4 , and N_2O are used. The two datasets are then joined using the same method as discussed previously [29], in which the Law Dome data is rescaled with NOAA. The radiative forcing formulas for CO_2 , CH_4 , and N_2O are from Butler and Montzka [31].

The NOAA AGGI indexes data include concentrations of CO_2 , CH_4 , and N_2O by middle of Julian year from 1979 to 2019. Concentrations of CO_2 , CH_4 , and N_2O were taken from Law Dome data for years 1750–1978.

3.1.1 Concentration and Radiative Forcing of CO₂

Law Dome ice cores for 1750–1978 [32, 33, 30, 34, 35] and data provided by NOAA from year 1979 to 2019 are used [36]. The data from year 1750–1978 are rescaled by a factor equal to quotient of year 1979 data of Law Dome and NOAA. The rescaling coefficient of CO₂ is 1.007.

For CO₂, the radiative forcing formula is

$$\Delta F = 5.35 \ln(C/C_0) \quad (3.2)$$

where $C_0 = 278$ is a reference value in ppm.

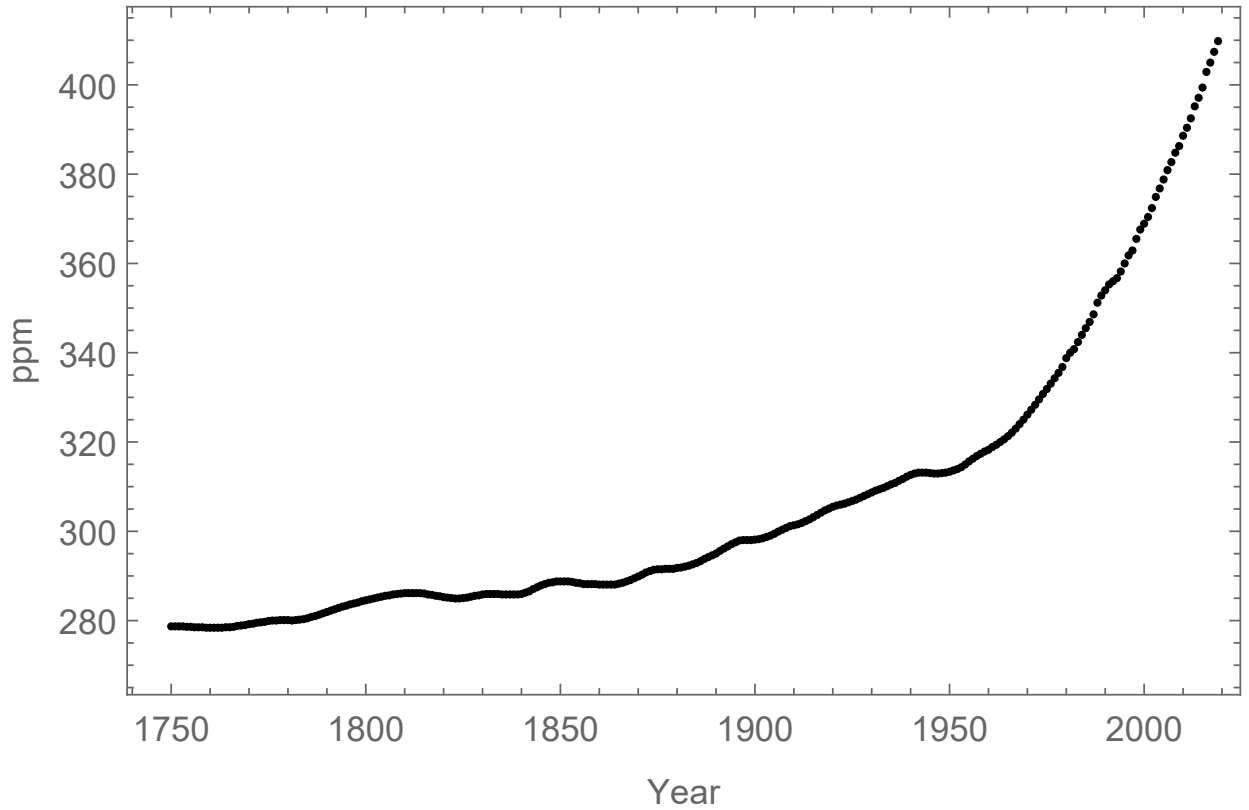


Figure 3.1: Historical CO₂ atmospheric concentration data since 1750.

Figure 3.1 shows the CO₂ atmospheric concentration variation since 1750. The pre-industrial CO₂ atmospheric concentration starts at about 280 ppm. Then, after the industrial revolution, the CO₂ atmospheric concentration kept going up to more than 400 ppm.

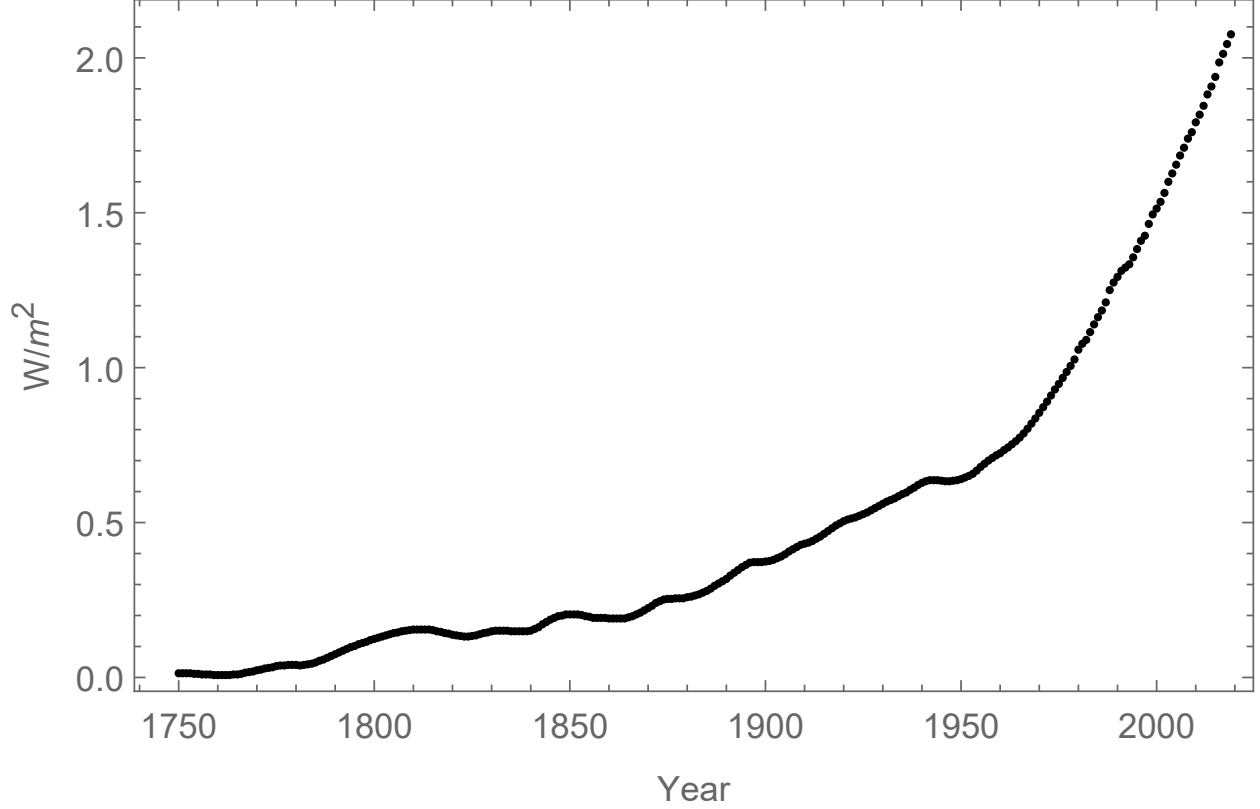


Figure 3.2: CO₂ radiative forcing change with respect to year 1750.

Figure 3.2 shows the corresponding CO₂ radiative forcing relative to base period 1750 level. CO₂ played the most important role in global warming recently.

3.1.2 Concentration and Radiative Forcing of CH₄

Like for CO₂, to avoid discontinuity between 1978 and 1979, the Law Dome CH₄ data from 1750 to 2004 were rescaled to NOAA, and then joined together with NOAA. The rescaling coefficient of CH₄ is 1.066 in our case.

For CH₄, the radiative forcing formula is

$$\Delta F = 0.036(M^{0.5} - M_0^{0.5}) - [f(M, N_0) - f(M_0, N_0)] \quad (3.3)$$

where $M_0 = 722$ and $N_0 = 270$ are reference concentrations in parts per billion (ppb). M is methane atmospheric concentration $\langle \text{CH}_4 \rangle$ in ppb. The function $f(M, N)$ is defined as

follows:

$$f(M, N) = 0.47 \ln [1 + 2.01 \times 10^{-5} \times (MN)^{0.75} + 5.31 \times 10^{-15} M(MN)^{1.52}] \quad (3.4)$$

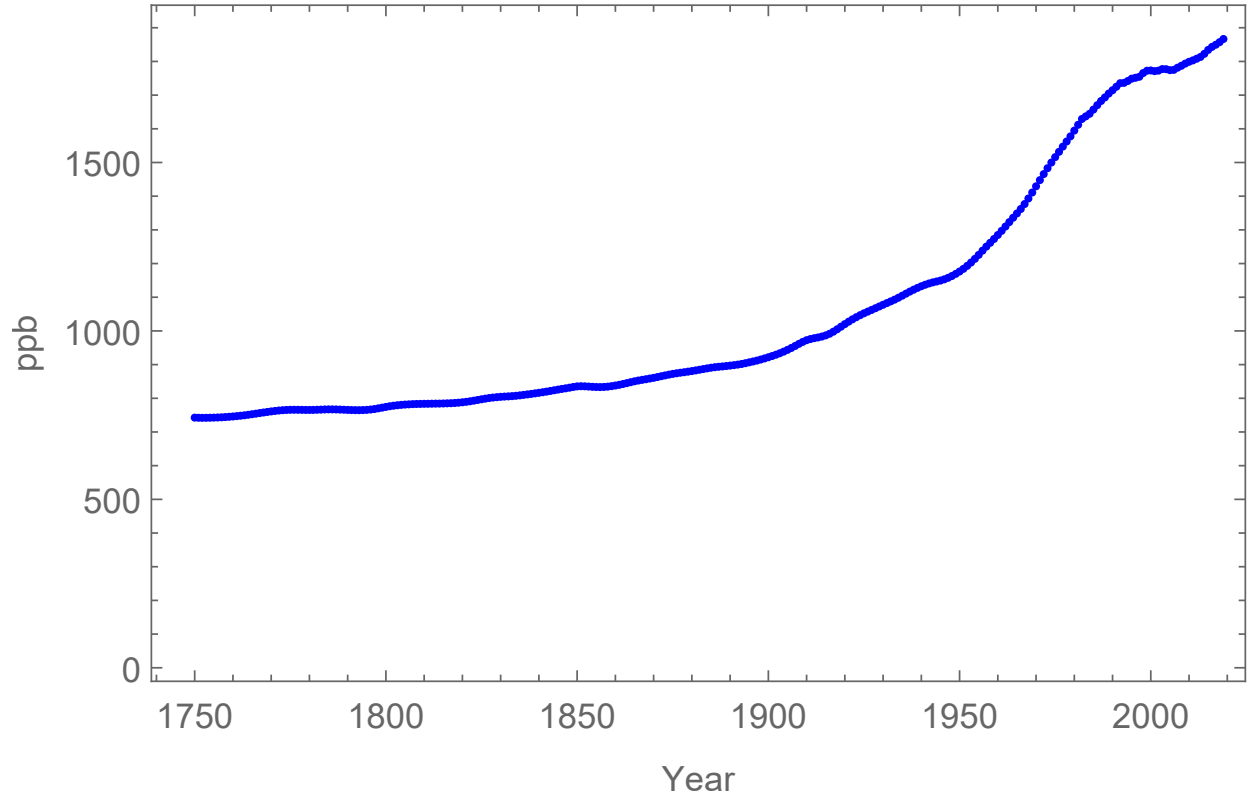


Figure 3.3: Historical CH₄ atmospheric concentration data from 1750.

Figure 3.3 shows that the methane concentration in the atmosphere grew from about 720 ppb in 1750 to more than 1800 ppb at 2019. Figure 3.4 shows that the radiative forcing from methane increased by over 0.5 W/m² compared to that in 1750.

3.1.3 Concentration and Radiative Forcing of N₂O

The historical concentration data of N₂O from Law Dome are rescaled to NOAA. In our case, the rescaling factor for N₂O concentration is 0.996. Figure 3.5 shows the joined Law Dome data and NOAA data of atmospheric concentration of N₂O from 1750 to 2019. For

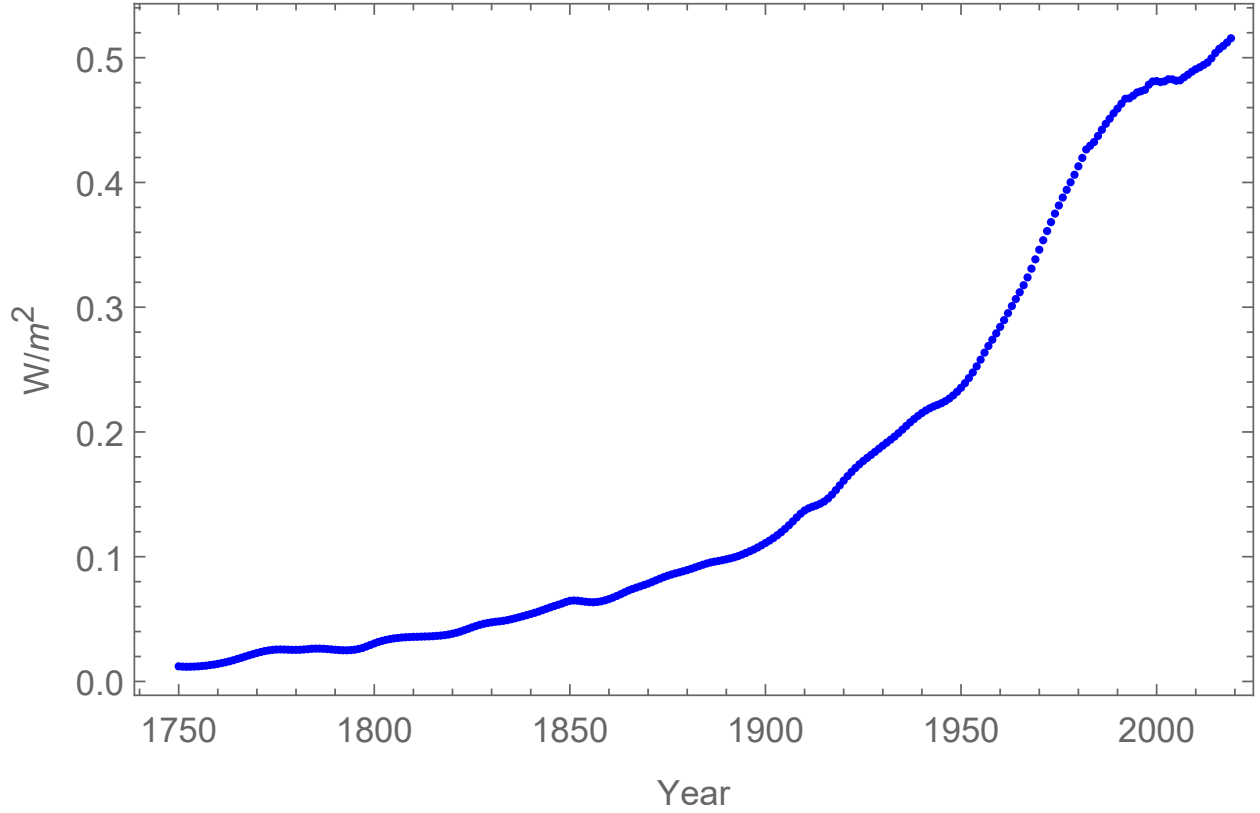


Figure 3.4: CH₄ radiative forcing change with respect to year 1750.

N₂O, the radiative forcing formula is

$$\Delta F = 0.12(N^{0.5} - N_0^{0.5}) - [f(M_0, N) - f(M_0, N_0)] \quad (3.5)$$

N is nitrous oxide atmospheric concentration $\langle N_2O \rangle$ in ppb.

Figure 3.5 shows that the nitrous oxide concentration in atmosphere grew from about 270 ppb at 1750 to more than 330 ppb at 2019. Figure 3.6 shows that the radiative forcing from nitrous oxide increased by over 0.2 W/m² since 1750.

3.2 Contrails, Land Use Change, and Other Well-Mixed Greenhouse Gases

This section discusses radiative forcing variation resulting from contrails, land use change (LUC), and other Well-Mixed Greenhouse Gases (WMGHG) compared to Julian year 1750.

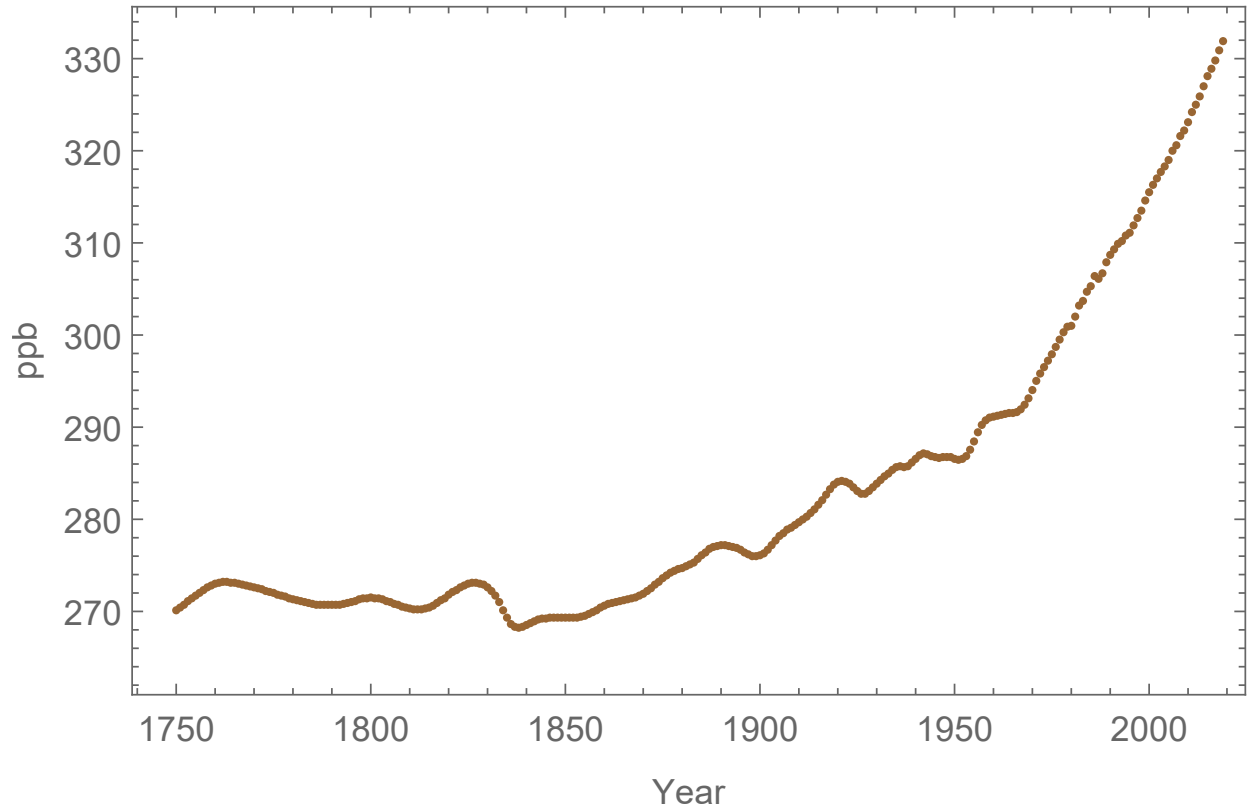


Figure 3.5: Historical N₂O atmospheric concentration data from 1750.

Here, the other WMGHG are all halogen compounds. IPCC AR5 reports extensive studies on the effects on τ from those species. Based on historical IPCC data from 1750 to 2011, their past variations of radiative forcing are discussed, and missing years' values are supplemented from other scientific sources respectively. Radiative forcing for other WMGHG, land use changes, and contrails are shown in figure 3.7.

3.2.1 Other Well-Mixed Greenhouse Gases

Before 1951, very low amounts of chlorofluorocarbons (CFCs) were released into the earth's atmosphere. So, radiative forcing from other WMGHG are approximated as zero from 1750 to 1950. For well mixed greenhouse gases other than CO₂, CH₄, and N₂O, use the NOAA sum of CHC11, CHC12, and 15 minor greenhouse gases from 1979–2019. For earlier times back to 1750, subtract input CH₄ and N₂O forcing from IPCC WMGHG other than CO₂ to get an estimate of forcing from the remaining other WMGHG [31]. Then, rescale that

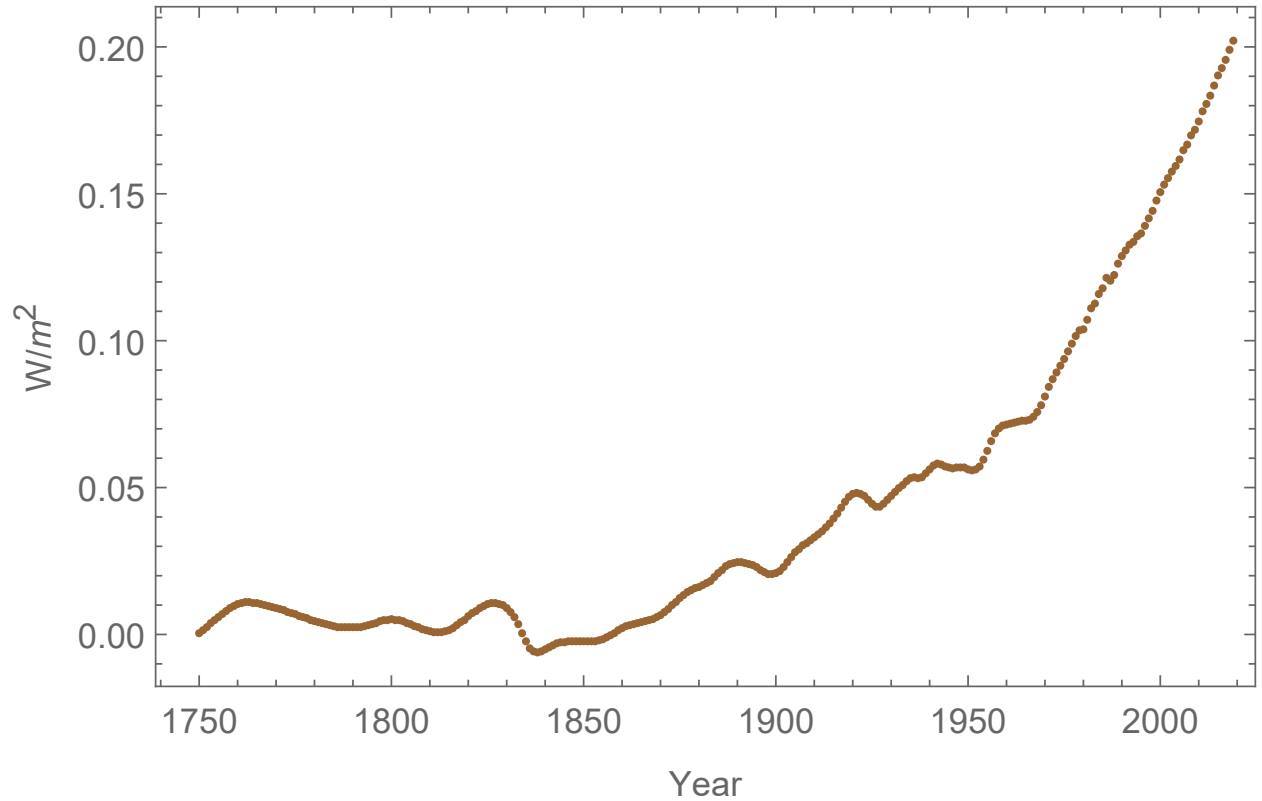


Figure 3.6: N_2O radiative forcing change with respect to year 1750.

result by multiplying by the ratio of the NOAA estimate from 1979 to the result calculated using the IPCC input, and then join the two time series to cover 1951–2019 and with zeros from 1750–1950.

3.2.2 Land Use Change

To extend land use change beyond 2011 through 2019, fit IPCC 2011 inputs with a sum of two logistic functions. This assumes land use change radiative forcing impacts can be approximated as permanent. Rescale the 2012–2019 fitted values by multiplying by the ratio of the IPCC value for 2011 to the fitted value.

3.2.3 Contrails

It is known that jet aviation emissions form contrails. However, because the airline industry was not well developed until after the first quarter of the twentieth century, radiative forcing estimates from contrails 1750 to 1928 in IPCC AR5 Table II -1-2 are all zeros. Thus, only data after 1928 are used to fit a logistic function. It is suggested by Bickel et al. [37] that “the contrail cirrus ERF is found to be less than 50% of the respective instantaneous or stratosphere adjusted radiative forcing, with a best estimate of roughly 35%.” So, first of all, fit the non-zero part of the IPCC forcing estimates from 1929 to 2011 with a single logistic function, and then rescale the extrapolation of 2012 to 2019 from the fit by a ratio equal to the quotient of IPCC forcing at 2011 with respect to the fitting forcing at 2011. After that, join the two periods of data and then multiply by 0.35 to get the contrails’ radiative forcing from 1750 to 2019.

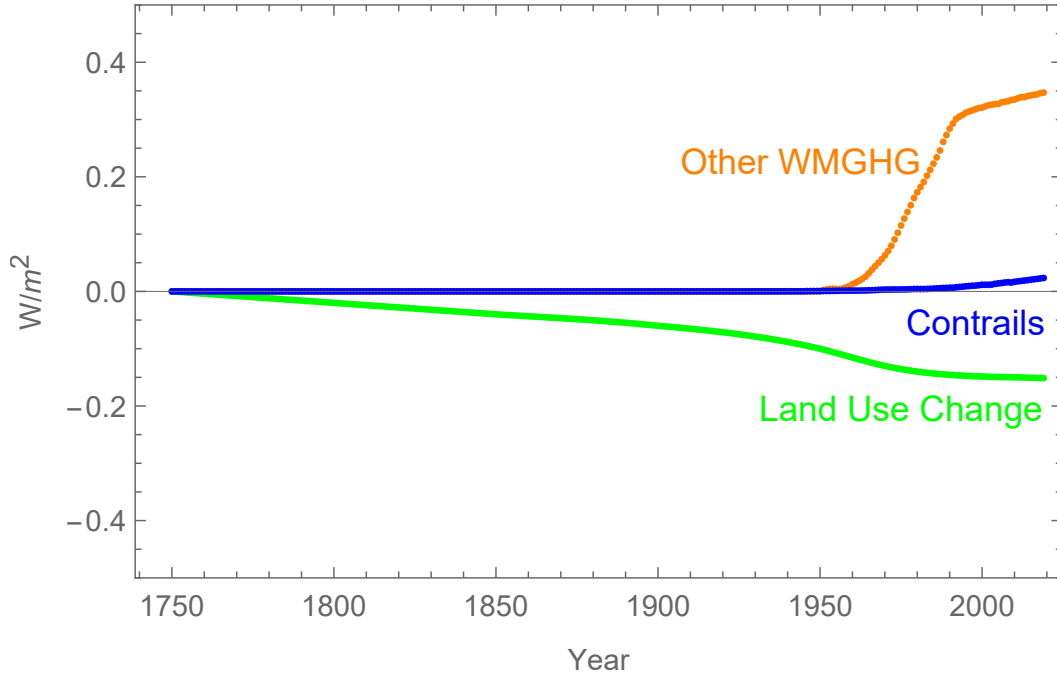


Figure 3.7: Radiative forcing of other WMGHG, LUC, and contrails change with respect to year 1750.

3.3 Volcanoes

In years near large eruptions, volcanoes contribute a large part of the uncertainty when estimating historical radiative forcing. Large volcanoes are treated as transients, because historical large volcanoes caused abrupt drops in global mean surface temperature τ , and then the global cooling effects stay noticeable only for at most a few following years before the evolution of τ returns to its previous trend. Therefore, it is very important to subtract the episodic temperature drop following large volcanic eruptions. However, since there were eruptions every year, the effects from small volcanoes can be seen as continuing small variations around constant. So, they are regarded as small evolving changes in radiative forcing in our case that can be added together with other slowly evolving contributions to radiative forcing when solving the global heat balance equation.

3.3.1 Large Volcanoes

As a starting point, the volcanic historic radiative forcing from 1750 to 2011 of IPCC AR5 is used. Also, in order to extend the volcanic forcing from 2012 to 2015, results from Schmidt et al. [38] data on volcanic SO_2 from 1979 to 2015 are used. To be more specific, for example, volcanic radiative forcing at 2012 is rescaled to Schmidt's radiative forcing by multiplying the quotient of Schmidt's data at year 2012 to 2011. After 2015 when the data of Schmidt et al. end, volcanic forcing from 2016 to 2019 can be approximated as zero with respect to the estimated pre-industrial average because their effects are small and no big volcanoes went off in the world after 2015.

Data from Global Volcanism Program-Volcanoes of the World 4.7.5 [39] are used to identify the dates of large volcanic eruptions. The large volcanoes are operationally defined as those with an IPCC database radiative shielding above a threshold of 0.35 W/m^2 . Any volcanic shielding of less than this threshold is considered to be non-transient and will turn out to have an included but very small effect. In our case, there are 14 large volcanoes in total from 1905 to 2019.

An equation for growth and subsequent decline per unit of (Aerosol Optical Density) AOD

from an eruption is

$$q(t) = c_q(t - t_s)e^{-(t-t_s)/t_v}, \quad \text{for } t > t_s \quad (3.6)$$

where $q(t)$ is the AOD data as a function of time t , and t_s is the time of when an eruption [19] started. c_q is a constant, and for Pinatubo is 0.439. The constant t_v is the 0.63 years from Douglass and Knox that AOD took to reach its maximum after the Pinatubo eruption. The change of volcano climate forcing is assumed to be proportional to AOD as:

$$\Delta F = -A \cdot q(t) \quad (3.7)$$

where A is a constant in unit of W/m^2 and ΔF is the change of volcano climate forcing.

Then, the energy balance model including a response time is expressed as follows:

$$t_d \frac{d\Delta\tau}{dt} + \Delta\tau = \lambda_v \Delta F \quad (3.8)$$

where t_d is the response time which brings a delay between ΔF and $\Delta\tau$. $\Delta\tau$ is the temperature change due to the large volcanoes eruption. λ_v is the volcano climate sensitivity. There exists an exact analytic solution of the above governing equation 3.8 with forcing, which takes the form of equation 3.7.

That solution is

$$\Delta\tau(t) = -0.439\lambda_v A \cdot \frac{t_v t_d}{(t_d - t_v)^2} \cdot \left\{ e^{\frac{-(t-t_s)}{t_d}} - \left[\left(\frac{1}{t_v} - \frac{1}{t_d} \right) (t - t_s) + 1 \right] e^{\frac{-(t-t_s)}{t_v}} \right\} \quad (3.9)$$

where t is time in years from the date of eruption.

Based on analysis of Pinatubo with the largest volcanic shielding in the period 1905–2019, the effect on global average temperature for a maximum of three years after each large eruption is included. For example, the Mount Pinatubo 1991 eruption has radiative shielding accumulated for the eruption year and three years after as $4.7 \text{ W}/\text{m}^2$. And its AOD has a sum over the same time of 0.39. Therefore, the ratio of total IPCC forcing of Pinatubo to AOD sums for its eruption is 12.1. This ratio will be used to rescale other large volcanoes later on. To be more specific, for the other large volcanoes, find the IPCC forcing

to AOD sum ratios including only the subsequent years over threshold 0.35 W/m^2 . However, large volcanoes before 1905 were not used. That is because large volcanic effects on global average temperature are approximated as having transient effects for a maximum of three years after the eruption. Large eruptions after 1905 are included because only global average temperature data from 1905–2019 are used in our analysis.

From Douglass and Knox (2005) [19], the value of the AOD coefficient A is derived from the Douglass and Knox modified temperature data set with $\lambda_v A = -3.72$ and $\lambda_v = 0.15$ as $A = -3.72/0.15 = -24.8$. Then, the total time integrated forcing coefficient in $(\text{W/m}^2)\text{yr}$ for all large volcanoes after year 1883 but Santa Maria are derived by multiply A with ratios of total time-integrated forcing to that for Pinatubo.

The Douglass and Knox formula for the evolution of the impact on global average surface temperature $\Delta\tau(t)$ for Pinatubo can also be written as:

$$\Delta\tau(t) = C_1 \left(e^{-(t-t_s)/t_d} - (C_2(t-t_s) + 1)e^{-(t-t_s)/t_v} \right) \quad (3.10)$$

where

$$C_1 = -c_q \lambda_v A t_v t_d / (t_d - t_v)^2 \quad (3.11)$$

$$C_2 = (1/t_v) - (1/t_d) \quad (3.12)$$

where time t is in years. Here $c_q = 0.439$, $t_d = 0.47$ year, and $\lambda_v = 0.15^\circ\text{C}/(\text{W/m}^2)$.

For other large volcanoes, the same formula 3.10 is used, but with A multiplied by the rescaling ratio with respect to Pinatubo.

To give an idea of the transient nature of large volcano effects on global average temperature before 1905, the results of the analysis from 1880–2019 are plotted in figure 3.8. Volcanic effects on τ for years from 1750 to 1879 are dropped, because large volcano effects last only a few years and only the effects from 1905 to 2019 will be used when calibrating the global heat balance model.

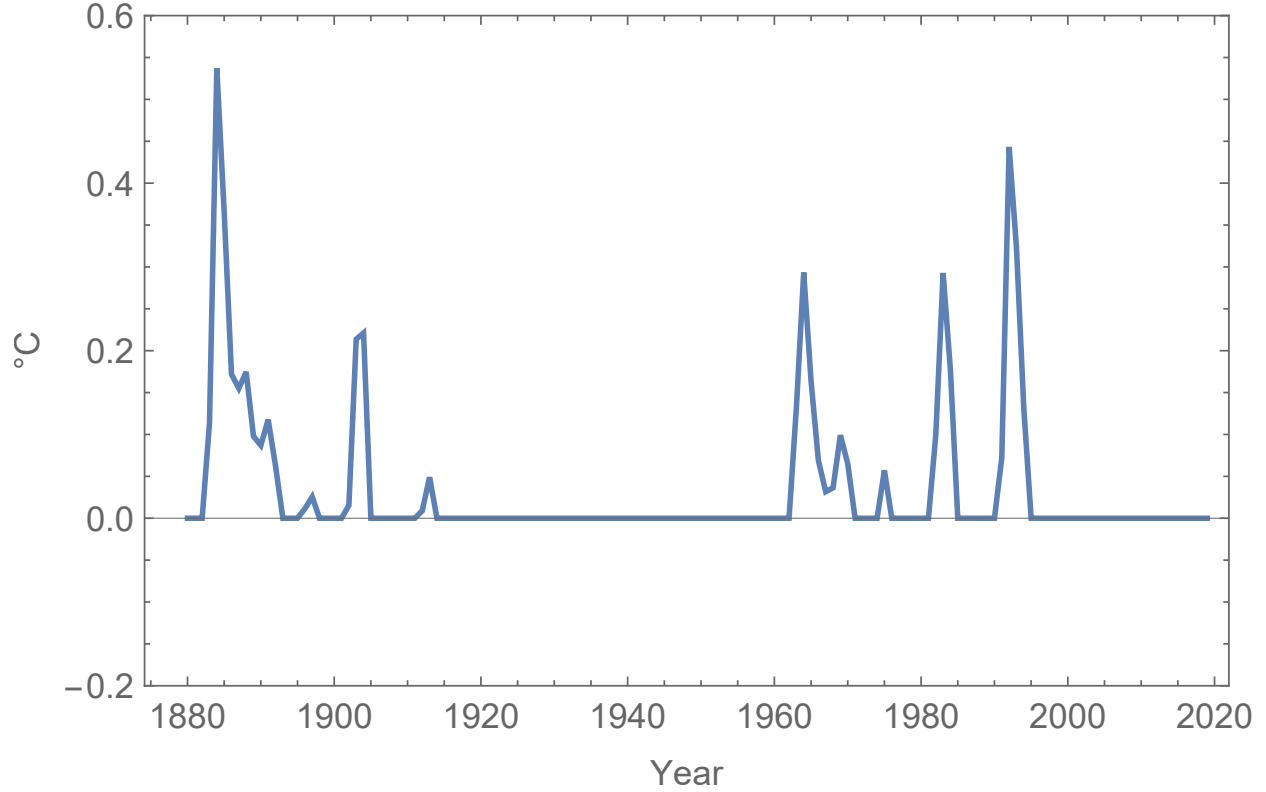


Figure 3.8: Absolute values of large volcanic eruption global average temperature impacts from 1880.

3.3.2 Small Volcanoes

IPCC AR5 have estimates for volcano radiative shielding for years from 1750 to 2011. Missing IPCC forcing were filled for 2012–2015 with ratios that rescale Schmidt’s estimates to match the IPCC number. Remaining missing numbers were filled with the resulting 2015 forcing times the later year’s ratio of Mtonne SO_2 to the 2015 Mtonne SO_2 based on the assumption that more SO_2 is emitted the stronger shielding from the small volcanoes. Volcanic SO_2 emission derived from ultraviolet satellite measurements from October 31, 1978, to present by the Multi-Satellite Volcanic Sulfur Dioxide L4 Long-Term Global Database V4 [40] are used in our analysis to calculate the small volcanoes shielding effects from 2016 to 2018.

The average for small volcanoes from 1838 is used as an estimate of the 1750 value to be subtracted when estimating the impact on the difference in τ from the τ in equilibrium with year 1750 forcing. Early IPCC entries have many zero values, suggesting that there is missing data and that including these would thus incorrectly estimate the average. Although the

last IPCC entry is in 1830, data for the years 1831–1837 is also not included when averaging of small volcanoes for 1838–2019 to avoid the complication of large eruptions in 1831 and 1835.

For this completed small volcanoes forcing data, reset the volcanic shielding at the years where big volcanoes went off as 0.35 W/m^2 . The average of those small volcanoes shielding is 0.16 W/m^2 . This number is subtracted from small volcanoes' shielding based on the assumption that this was the pre-1838 average and thus part of the pre-industrial base that small volcano shielding is an increment over or under. So the small volcanic shielding values used have this number subtracted from them, and the net small volcanoes' shielding from 1838 on are found. For the 1750 to 1837 values, the IPCC data is considered to be so incomplete that the pre-industrial average is assumed, so the difference from the pre-industrial average for 1750–1837 is approximated as zero.

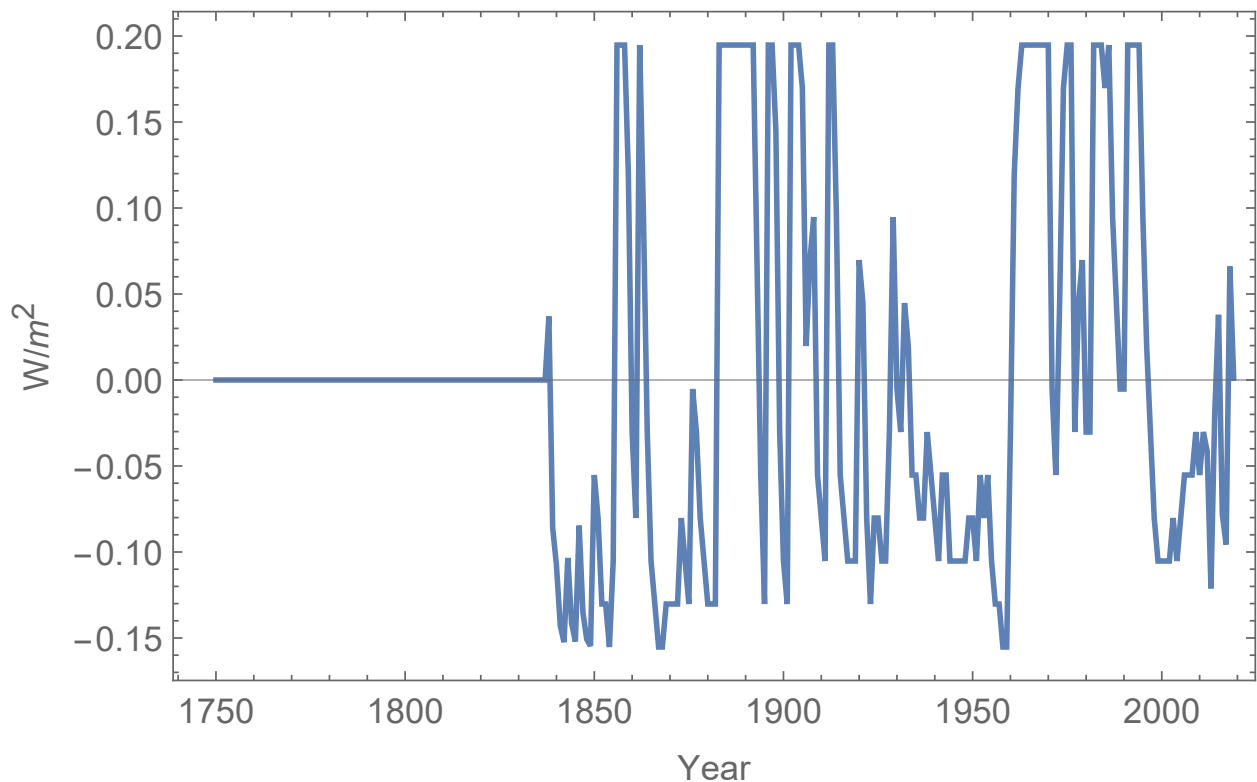


Figure 3.9: Small volcanoes radiative shielding from 1750 to 2019.

Figure 3.9 shows the small volcanoes' radiative shielding estimates from 1750 to 2019. Note that volcanic aerosols blocks the sunlight and cool the planet, so it is a kind of shielding.

The plateaus are the years when transient effects from big volcanic eruptions are included.

3.4 ENSO

This section introduces correlation of the multivariate ENSO index (MEI), with values of $\Delta\tau_{ENSO}$ from 1979–Sept 2020. Use the resulting ratio to estimate $\Delta\tau_{ENSO}$ for 2019 and 2020, and join that with 1872–2018 $\Delta\tau_{ENSO}$ input. The 1871 to 2005 bimonthly MEI values from Wolter and Timlin (2011) are used [41]. Also, their bimonthly MEI values from 1950 to 2018 are used. To extend the MEI values to 2020, the new version of bi-monthly multivariate ENSO index by Wolter are used [42, 43, 44]. Then, the annual MEI index from three different datasets are calculated by take the average over 12 months. From Lean and Rind (2008), it is suggested that the global average temperature response τ lags after the MEI index by four months [17].

Because the more recent 1950 to 2018 MEI index data are assumed to be more accurate, the MEI index from 1871 to 2005 are rescaled to more recent ones by a linear fit of second MEI index on the first MEI index data on overlapping years from 1950 to 2005. Then, regarding the 2019’s MEI index, the increase from 2019 to 2018 of third MEI index data are added to the second MEI index dataset’s value at year 2018. Then, following Foster and Rahmstorf [16], the coefficient between MEI index and changes in global average temperature associated with ENSO is about $0.08\text{ }^{\circ}\text{C}/\text{MEI}$. So, the three MEI index data are joined together to form a complete historical data from 1871 to 2019. The average of MEI index from 1871 to 2019 are subtracted from the data to get the change of MEI index. Then, these corrected MEI index are multiplied by the coefficient to get the ENSO effects on τ .

To give an idea of how the ENSO-related global average temperature variation compared in decades before and after 1905, figure 3.10 shows that variation based on the proportionality coefficient estimated by Foster and Rahmstorf [16].

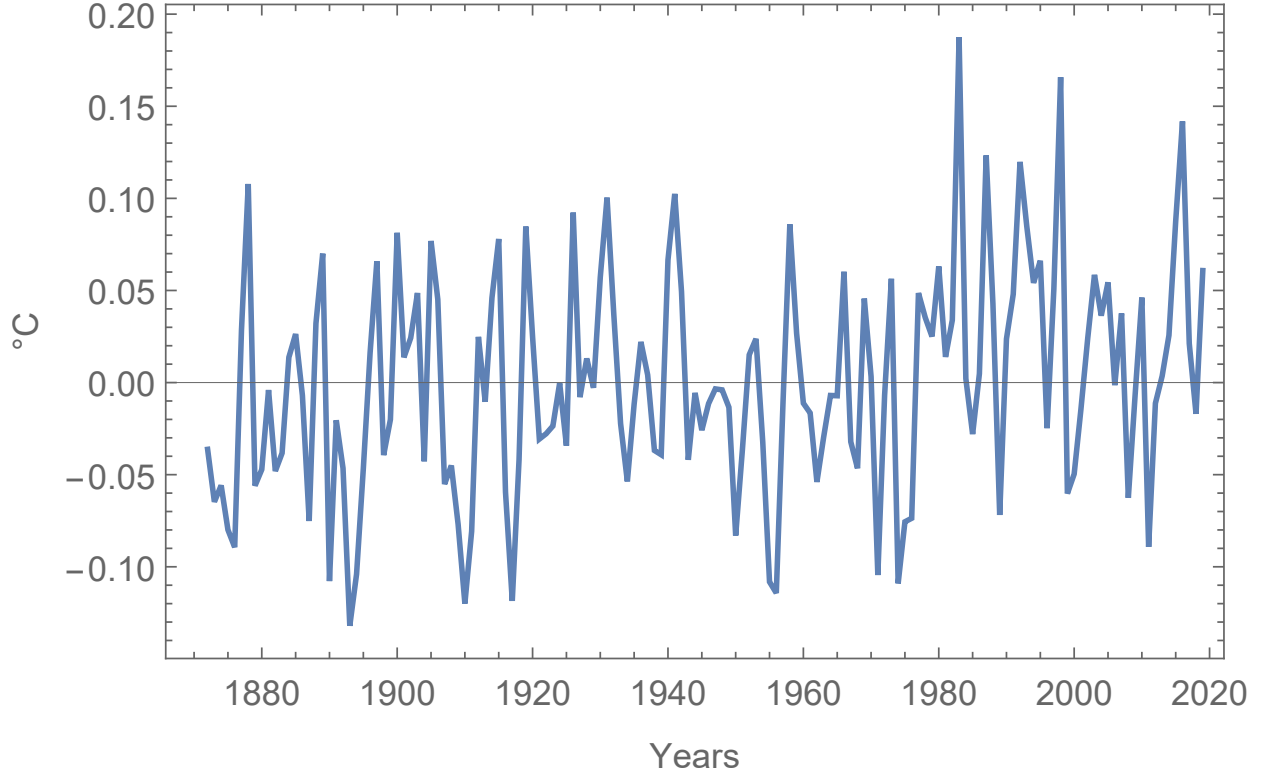


Figure 3.10: ENSO effects on global surface temperature τ from 1872 to 2019.

3.5 Solar Irradiance Variation

As for volcanic shielding, effects of variation of solar irradiance are divided into transients and variations of radiative forcing on longer timescales. The transients in our analysis occur on an approximately 11-year cycle. There have been long records about the sunspot cycles. The duration of the sunspot cycle is, on average, around eleven years. From the first recorded solar cycle beginning in 1755, we are now in solar cycle 25. Besides the short term solar variations, there are also longer term variations with a period of approximate 800 years which is called “Grand Minimum” as well as “Gleissberg cycle” of around 80 years. The slow variations are fitted with a sum of three cosine functions in our case.

3.5.1 Grand Minimum, Gleissberg and “Double Gleissberg”

First of all, the historical Total Solar Irradiance (TSI) data from 1610 to 2018 are used [45]. The 2019 year data are added based on satellite observations [46].

Fit the 1750–2019 increase in annual solar irradiance with a fixed period of cosine function. This cosine function is aiming to search for grand minimum oscillation to avoid continuing linear growth in the secular trend. Based on McCracken’s work, the period of grand minimum oscillation is about 706 to 906 years [47]. However, in our case, due to the lack of data, there is no way to check if this is accurate. So, it is assumed the average of 706 and 906 years is the grand minimum oscillation period. Then, a single Gleissberg cycle is added to the above grand oscillation cosine fit. After that, fix the least squares fits from the previous two cosine terms fits, and then add another cosine term with about twice the Gleissberg period from 1830–2019 to account for successive Gleissberg cycles having different amplitudes. That is to avoid a simultaneous 8-parameter fit losing track of the different amplitudes of successive Gleissberg cycles. Figure 3.11 shows the three cosine fit described above. What is plotted is change in radiative forcing from a 1700–1749 average. For radiative forcing with respect to 1750, the year 1750 forcing shown in figure 3.11 is subtracted from what is plotted in that figure.

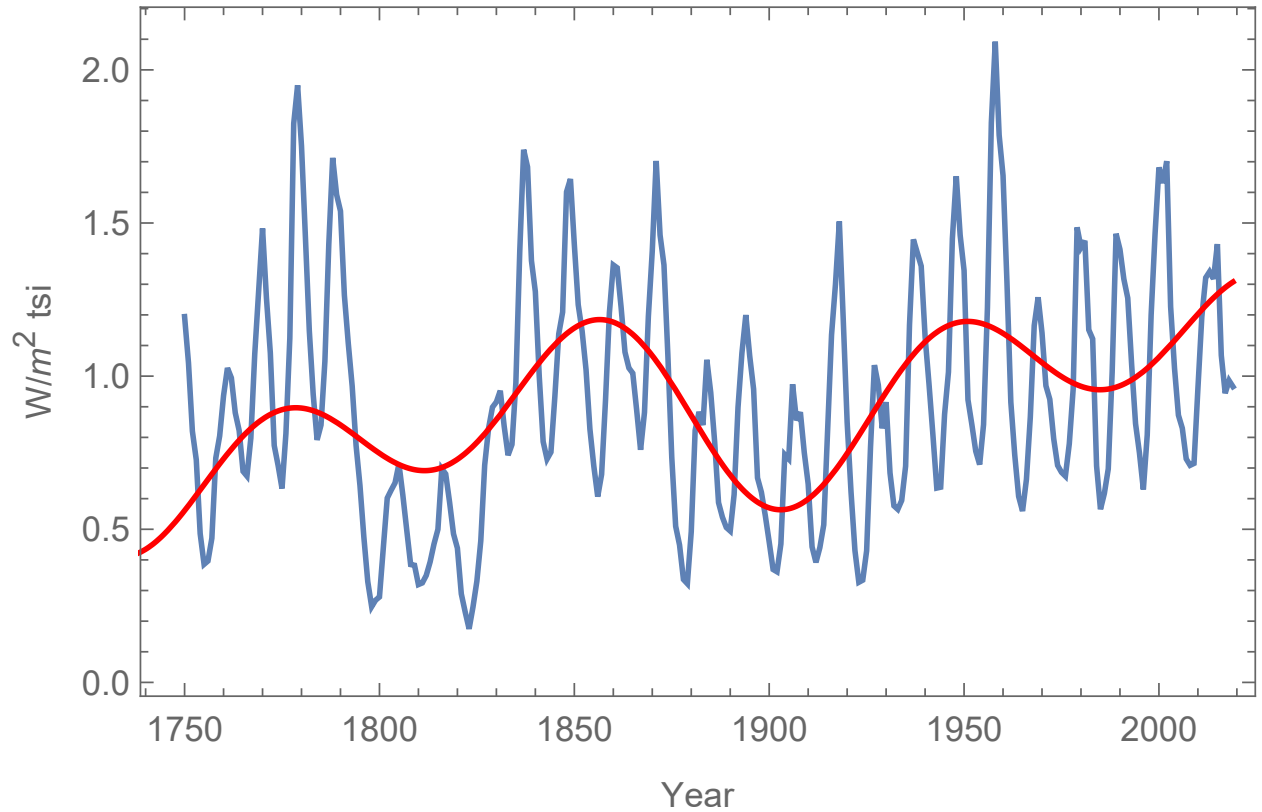


Figure 3.11: Three cosines fit to historical solar irradiance from 1750–2019.

Table 3.1 Total Solar Irradiance Parameters in $b_1 \cos(2\pi(t - b_2)/b_3)$

Type	$b_1(\text{W/m}^2)$	b_2 (Julian Year)	b_3 (Years)
Grand Minimum	0.189	2103.81	842
Gleissberg	0.227	1944.79	85.58
Double Gleissberg	0.153	1994.31	160.20

Table 3.1 summarizes the parameters fitted in three cosines fits of total solar irradiance. Note that solar radiative forcing averaged over the earth's surface is 1/4 of the value of total solar irradiance.

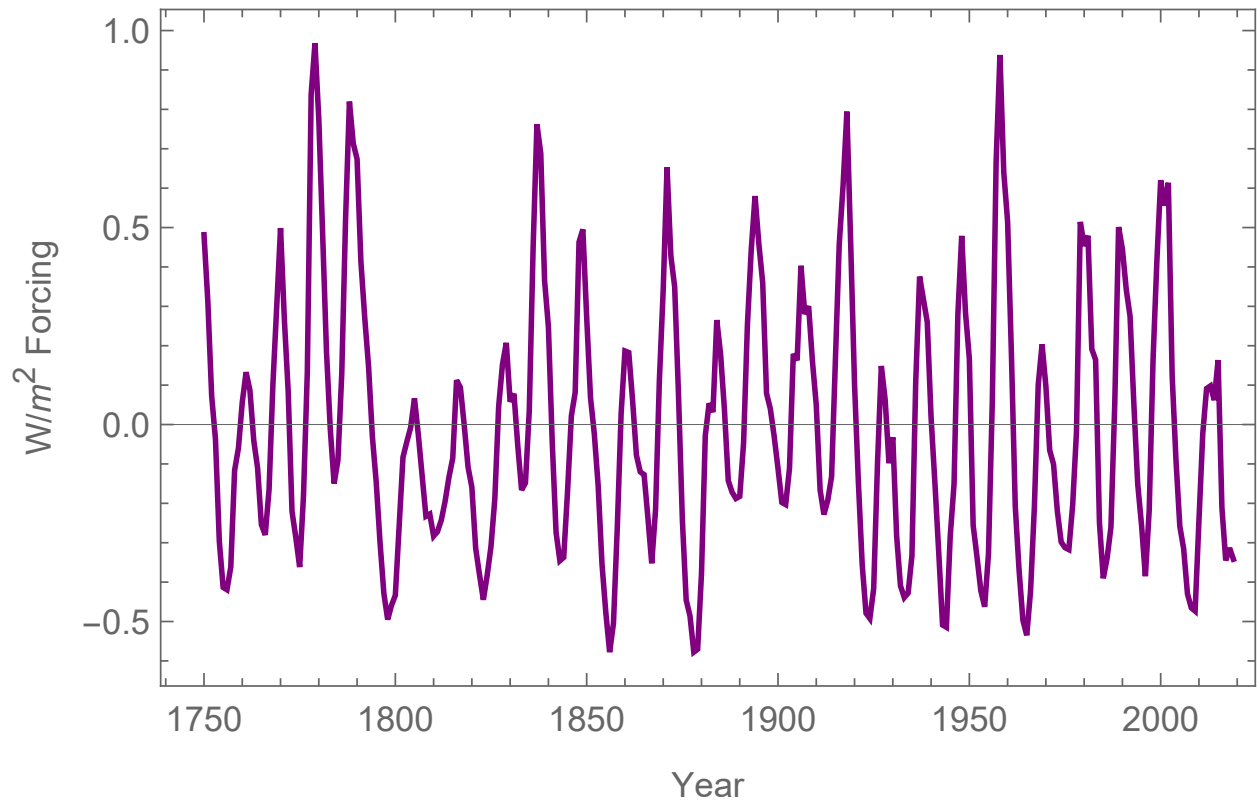


Figure 3.12: Residuals between total solar irradiance changes and a three cosine fit to longer-term evolution of solar irradiance from 1750–2019.

Figure 3.12 shows the residuals from the three cosine fit. These residuals provide a starting point for estimating the transient effects of the approximately 11 year solar irradiance cycle

on global average temperature. Here, for brevity, the word approximately is omitted below when referring to the period of the 11 year solar cycle.

3.5.2 Eleven Year Solar Cycle Effects on τ

The change in τ in each year due to 11-year solar cycle variations in TSI is taken to be proportional to the TSI for that year corrected by adding 31/365 of the irradiance for December of the previous year less 31/365 of the irradiance for December for that year. From the work of Lean and Rind (2008), it is suggested that the global average temperature response τ has a one-month lag on 11-year solar cycle variations [17]. To compute the required differences in December, daily irradiance estimates from 12 May 1797 through 29 May 2017 from Spectral And Total Irradiance REconstructions (SATIRE) (WU et al. 2018), supplemented by NASA Clouds and the Earth’s Radiant Energy System (CERES) project TSI data for 1 December 2015 through 31 December 2019 [48, 49]. These two datasets are used to find the one month lag of TSI on the effects of the 11 year solar cycle on global surface temperature change. To begin with, find the average solar irradiance for December from 1879–2016. Then, to account for a month lag to temperature effects, the following year’s December average TSI is subtracted by previous years’ December average TSI data and then the December’s TSI differences was rescaled by the ratio of days in December which is 31/365. From 1880 to 2016, the rescaled December difference are calculated in this way. The CERES data from 2017 to 2019 are lag corrected in the same way. Then, the one-month lag corrected eleven years’ solar cycle TSI data is obtained by subtracting these rescaled annual December difference from the 11-year cycle TSI data obtained from previous section for year 1880 to 2019 and then subtract the mean of the corrected data as well.

After the TSI lag correction for 1880–2019 has been done, then, for the estimates of short term solar cycle effects on τ , the proportionality constant that is read off from figure 3 of Foster and Rahmstorf (2011) is used. The conversion factor from lagged solar irradiance to effect on τ is 0.084 °C/TSI. However, later on, to account for a large uncertainty remained here, an additional multiplier will be included in a subsequent chapter as a nuisance parameter to be integrated over when the marginal posterior probability distribution for other

parameters is fitted with a 3-D analytic function.

Figure 3.13 shows the eleven year solar cycle effects on global surface temperature τ from 1880 to 2019. Only global average temperature estimates from 1905–2019 are used for calibrating parameters in the global heat balance. The results in figure 3.13 for before 1905 are only shown to illustrate how this solar cycle effect varied over a longer time period.

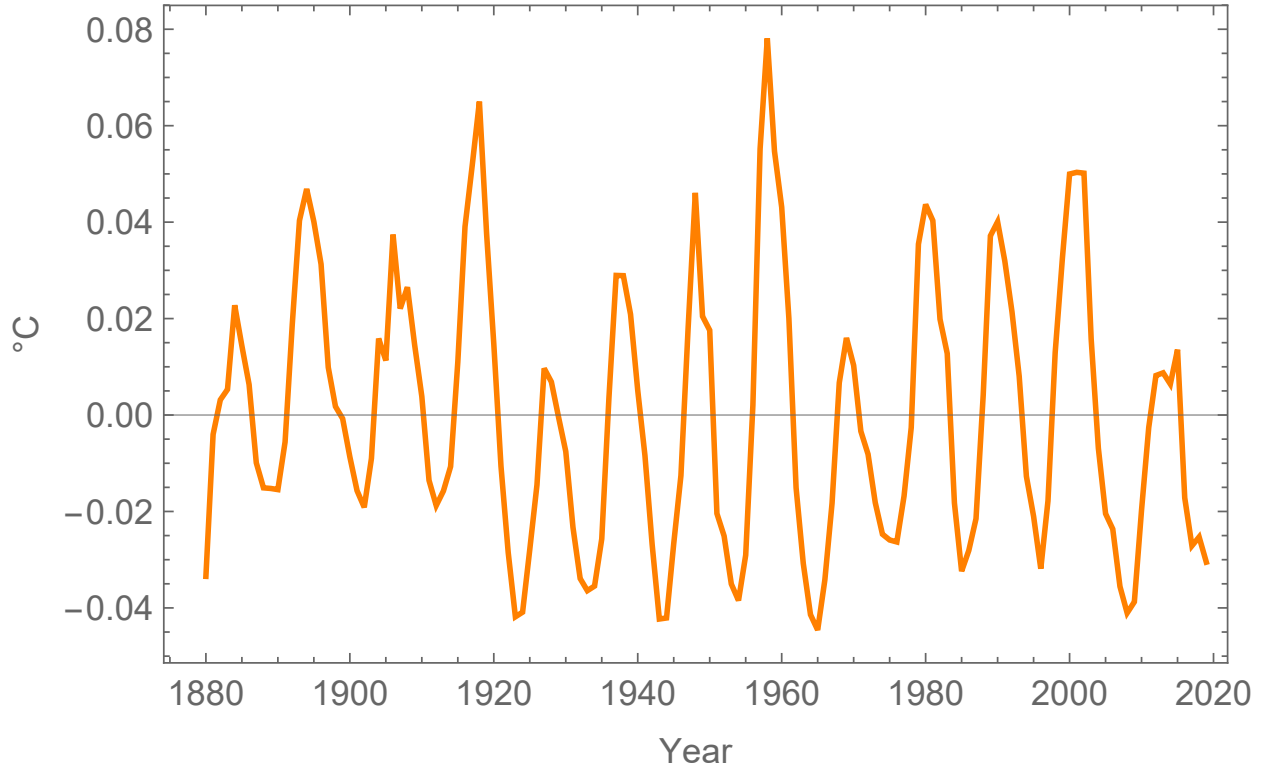


Figure 3.13: Eleven year solar cycle effects on global surface temperature τ from 1880 to 2019.

3.6 Historical Adjustable Radiative Forcing

This section discusses estimates of adjustable radiative forcing from 1750–2019 for the total of tropospheric and stratospheric zone, from direct and indirect effects of tropospheric aerosols, and from black carbon on snow.

The IPCC AR5 radiative forcing contributions from tropospheric and stratospheric ozone are added together with the total tropospheric aerosol forcing from 1750 to 2011. The

Goddard Institute for Space Studies (GISS) forcing [50] for 1850–2011 relative to 1850 from combined tropospheric and stratospheric ozone and total of direct and indirect forcing from tropospheric aerosols are also added together.

The first year that the GISS estimate is decreasing is 1891. An adjustment to convert GISS estimates to be relative to 1750 instead of relative to 1850 is done by adding the difference of previous IPCC and GISS forcing at year 1891 to GISS forcing values. That difference is -0.175215 W/m^2 . The 2013–2019 GISS forcing values are extended by assuming all the same as the value at year 2012, as indicated by the lack of a clear trend over that period reported by Brellouin et al [51].

For black carbon on snow, the IPCC [52] forcing from black carbon on snow is used as being more temporally complete and better matching the above literature estimate than GISS value plus the IPCC 1850 to 1750 difference. The claim that the effective climate sensitivity for radiative forcing could be 3 times greater than for well mixed greenhouse gases is assumed not to be quantitatively accurate enough to implement when solving the global heat balance equation. The overall total aerosol and ozone and black carbon on snow is in any case multiplied by a parameter to be sampled from a probability distribution based on a paper by Shindell [53]. To extend the IPCC black carbon on snow forcing to year 2019, the amount of forcing from 2012 to 2019 are assumed as the same as year 2011 value. Then, the extended IPCC black carbon on snow forcing added by the combined IPCC and GISS forcing of ozone, tropospheric aerosols are plotted in figure 3.14.

3.7 Stratospheric Water Vapor

To extend IPCC stratospheric water vapor radiative forcing for the eight years beyond 2011 through 2019, the IPCC methane concentration increase over 1750 from 2010 to 2017 is multiplied by a ratio. That ratio is the eight year average of IPCC water vapor radiative forcing from 2004 to 2011 divided by the the IPCC methane concentration increase over 1750 from 2002 to 2009. Then, the stratospheric water vapor radiative forcing from 1750 to 2019 is obtained by joining the two datasets together. In this calculation, it is assumed that the stratospheric water vapor radiative forcing has a two-year lag on the methane atmospheric

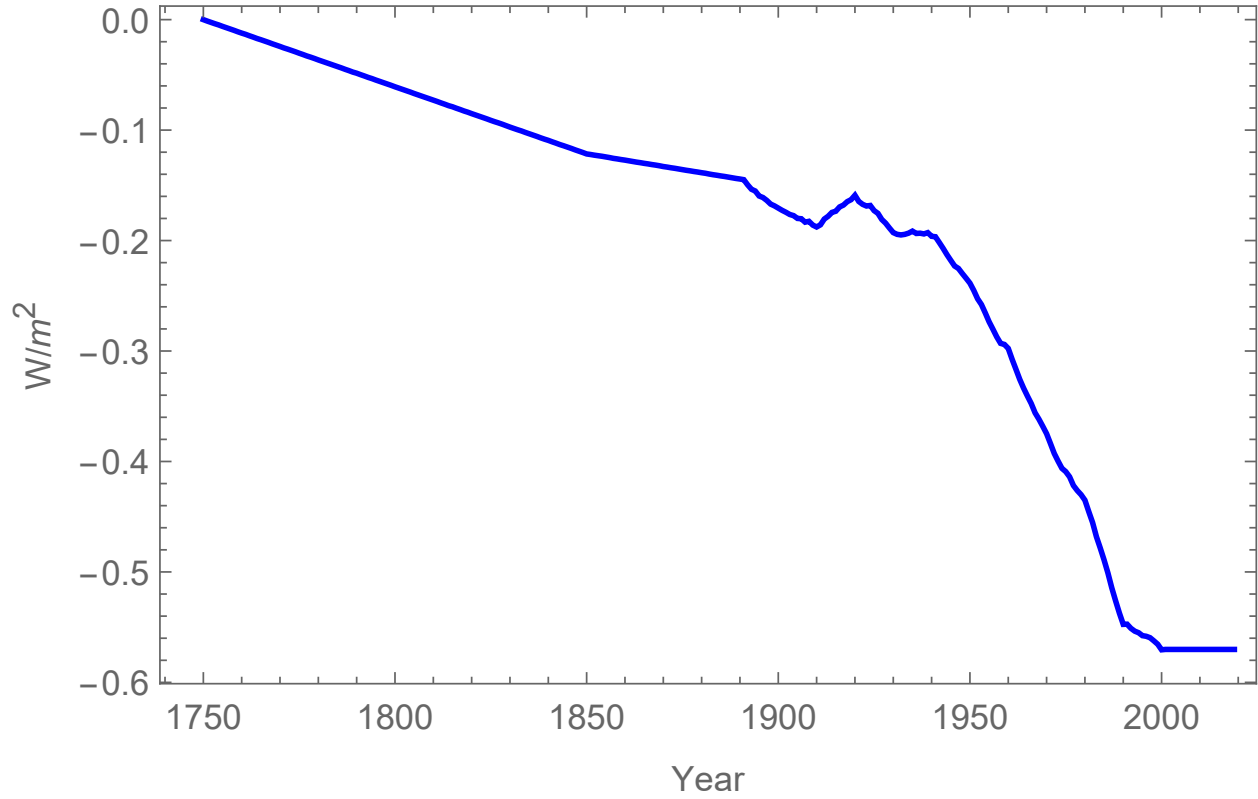


Figure 3.14: Radiative forcing estimates for the total from ozone, total from tropospheric aerosols, and from black carbon on snow from 1750 to 2019.

concentration discussed by Miller et al. (2014) [50].

Figure 3.15 shows the radiative forcing estimates for stratospheric water vapor from 1750 to 2019.

3.8 Radiative Forcing Time Series Data Summary

All the above radiative forcing estimates are combined in this section to analyze the total radiative forcing time series data.

Here, the previously discussed forcing contributions from CO_2 , CH_4 , N_2O , halogens, land use changes, contrails, and stratospheric H_2O forcing are all added together to get the forcing that is going to be used without any adjustable multiplier. Figure 3.16 shows the increase over 1750 of sum of the non-adjustable anthropogenic radiative forcing.

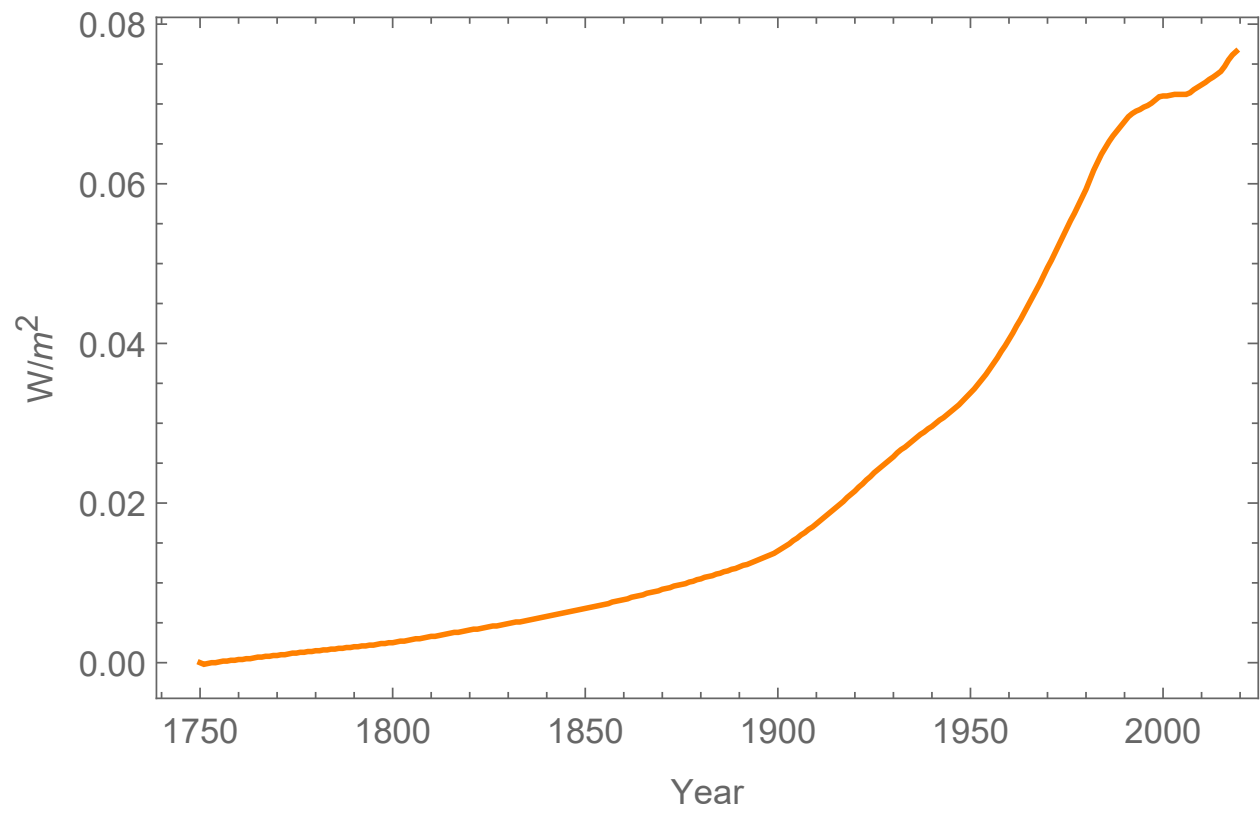


Figure 3.15: Radiative forcing estimates for stratospheric water vapor from 1750 to 2019.

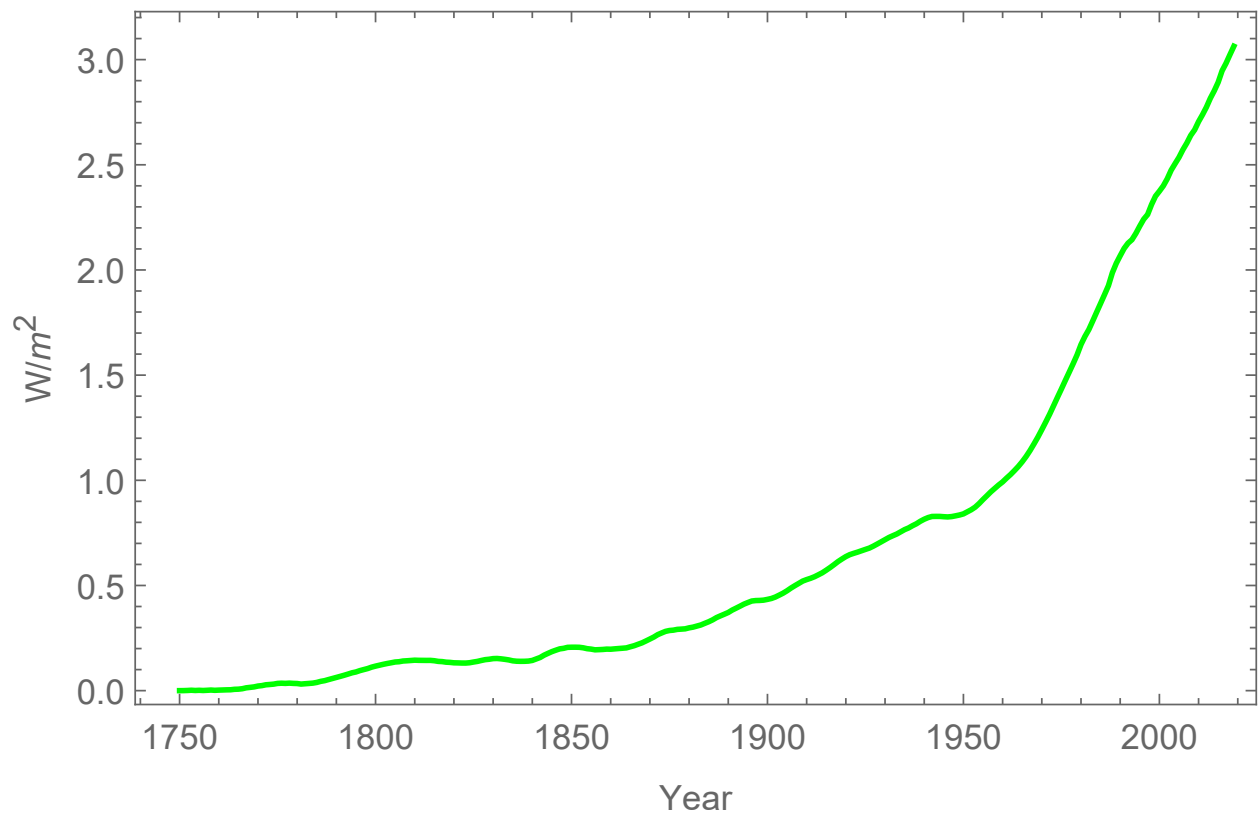


Figure 3.16: Sum of non-adjustable anthropogenic radiative forcing from CO_2 , CH_4 , N_2O , halogens, land use changes, contrails, and stratospheric H_2O increase over 1750 level.

CHAPTER 4

MAXIMUM LIKELIHOOD ESTIMATION

After the total radiative forcing F and natural transients effects on τ have been figured out, the global mean surface temperature response τ is approximated as the solution to an inhomogeneous linear first order differential equation. However, only three parameters are important to us for the purpose of multi-decadal extrapolation of future increases in global average temperature in times when shielding from large volcanic eruptions are small and averaged over cyclic transient effects. Those parameters are λ , c_{th} , and c_{reg} . All the other parameters are treated as nuisance parameters by integrating over them to find a marginal probability distribution as a function of λ , c_{th} , and c_{reg} .

Maximum marginal probability estimation is used here to find parameters given the historical temperature data and ocean heat energy data observed. However, the numerical integration over the nuisance parameters is not trivial and so needs further discussion in this chapter. Also, temporally auto-correlated residuals from the fitting of ocean heat content are considered. This chapter finally gives a 3-D marginal posterior distribution for $p(\lambda, c_{th}, c_{reg})$ that maximizes the derived marginal probability function and draws samples from the solved distribution to make extrapolations on τ into future.

To discuss derivation of a joint marginal posterior probability distribution for three parameters in the global heat balance equation 3.1, first of all look at all the remaining radiative forcing without F_{reg} included, as follows:

$$F' = f_1 + f_2 + f_3 \tag{4.1}$$

where

$$f_3 = c_{volc}(\lambda_v/\lambda) \cdot volc \tag{4.2}$$

Here, F' is the sum respectively of the radiative forcing described in previous chapter. f_1 is slowly evolving solar irradiance forcing fitted by summation of three cosine functions, f_2 is the non-adjustable anthropogenic radiative forcing contributions from CO_2 , CH_4 , N_2O , halogens, land use changes, contrails, and stratospheric H_2O forcing, f_3 is the corrected small volcanoes radiative forcing. c_{volc} is an adjustable parameter. λ_v is $0.15^\circ\text{C}/(\text{W}/\text{m}^2)$, represents the volcano climate sensitivity suggested by Douglass and Knox (2005) [19]. λ is the climate sensitivity of global heat balance model in $^\circ\text{C}/(\text{W}/\text{m}^2)$. $volc$ is the small volcanoes (for under threshold volcanoes) radiative forcing in W/m^2 which is equal to -1 times the shielding function plotted in figure 3.9.

Here, the total radiative forcing F can be rewritten as following:

$$F = F' + c_{reg}F_{reg} \quad (4.3)$$

where F_{reg} is the above-mentioned reference estimate of global radiative forcing from the sum of tropospheric aerosols, stratospheric ozone, tropospheric ozone, and black carbon on snow. F_{reg} is called adjustable radiative forcing. F' includes all the remaining radiative forcing after $c_{reg}F_{reg}$ is subtracted. F' is called non-adjustable radiative forcing. Primarily due to uncertainties in the value of radiative forcing from tropospheric aerosols, uncertainty about the value $c_{reg}F_{reg}$ is the largest uncertainty about total radiative forcing [52, 2]. c_{reg} is the regionally dependent industrial forcing efficacy. Cast here in the form of a prior probability distribution, there is a constraint on appropriate values for c_{reg} from detailed analysis of the global response to regional variations in the components of F_{reg} [53]. There are also constraints on appropriate values of the thermal inertia parameter, c_{th} , based on data about the evolution of changes in stored energy primarily in the top one to two kilometers of global oceans. Historical evolution of changes, τ , in global average temperature puts constraints on appropriate values of the climate sensitivity, λ .

To solve the global heat balance equation 3.1, define variables as follows:

$$\mu = 1/(c_{th}\lambda) \quad (4.4)$$

$$\beta = \lambda(1 - e^{-\mu})e^{-\mu/2} \quad (4.5)$$

Approximating radiative forcing in year k from 1749 as a different constant F_k in each year, the solution is

$$\begin{aligned} \tau_1 &= 0 \\ \tau_n &= \lambda(1 - e^{-\mu/2})F_n + \beta \sum_{k=1}^{n-1} F_k e^{-(n-k)\mu} \quad \text{for } n = 2, \dots, 270 \end{aligned} \quad (4.6)$$

We set year 1750 as the starting point with total radiative forcing at that time being 0, so, $\tau_1=0$. Details about the derivation of this solution can be found in Appendix A. Here, it is assumed that the previous years' radiative forcing effects on the current year temperature τ_n decay exponentially with time.

A joint probability distribution for the global heat balance model parameters is integrated here over all of the other adjustable parameters in the model. The result is suitable for extrapolation of global average temperature, except for brief transients from large volcanic eruptions, averaged over ENSO-correlated variations in τ and small transients associated with the 11 year solar cycle.

4.1 Coordinate Transformation for c_{th} and λ

Approximating historical total radiative forcing as having grown exponentially with time gives an analytic solution to the global heat balance equation. The equation in this approximation is:

$$c_{th} \frac{d\tau}{dt} = F_0 e^{\nu(t-2019)} - \frac{\tau}{\lambda} \quad \text{for } t=1750, \dots, 2019 \quad (4.7)$$

where ν is a constant growing rate fit to the total radiative forcing F and F_0 is the radiative forcing at year 2019 in W/m^2 . Using the initial condition of $\tau=0$ in Julian year 1750, the

solution of equation 4.7 is:

$$\tau = \frac{F_0}{1/\lambda + \nu c_{th}} e^{\nu(t-2019)} \quad \text{for } t=1750, \dots, 2019 \quad (4.8)$$

It suffices to use the applied initial condition, since the impact any departure from this initial condition decays exponentially by orders of magnitude by 1905, when the first global average temperature data are used.

Let $\zeta = 1/(1/\lambda + \nu c_{th})$. This means that any combination of λ and c_{th} that gives the same value of ζ will give almost exactly the same results for the temperature data used here. In this approximation, there is a lower limit of ζ on λ since physically c_{th} is not negative, but λ can be very large if c_{th} is large due to rapid thermal transport into the deep ocean. This observation suggests that the probability distribution being sought here may be skewed.

Efficiently computing a set of results for the probability of the data given the model parameters requires choosing values of λ and c_{th} that lie along a curve of constant ζ . Small deviations from this restriction are explored by choosing values of λ and c_{th} that lie on a set of curves orthogonal to the curve of constant ζ . Therefore, the new orthogonal coordinates of c_1 and c_2 are defined as follows:

$$c_1 = \nu \cdot c_{th} + 1/\lambda = 1/\zeta \quad (4.9)$$

$$c_2 = \nu \cdot c_{th} + \lambda^3/3 \quad (4.10)$$

4.2 Corrections to Global Mean Temperature and Ocean Heat Content

In this section, the global land-ocean temperature index from 1880 to 2019 by NASA Goddard's Global Surface Temperature Analysis (GISTEMP) [54, 55] is used. The January to December average for years between 1941 and 1945 from GISTEMP data $\tau_{gistemp}$ is corrected for a WWII warming anomaly. Then the natural transients ENSO, solar variation, and large

volcano effects are subtracted out from the corrected GISTEMP data. Finally, a constant is added to the GISTEMP data to get an estimate of the difference between that data and the temperature that would be in equilibrium with the radiative forcing in Julian year 1750.

Also, there are coefficients that are multiplied before each category of natural transients respectively. From year 1905 to 2019, there are 115 yearly global surface mean temperature data points going to be used. That is because there are concerns about the data accuracy and unusually frequent and strong volcanic activities during the 1800's and in 1902. Also, the ocean heat content data from 1995 to 2014 are used, as noted above. So there are 20 data points energy stored in ocean used for the according years.

4.2.1 Corrections to Global Mean Surface Temperature

Natural transients and WWII Temperature Anomaly corrections to GISTEMP data are now discussed. The land-ocean global mean temperature difference from 1951–1980 base period average from GISS is used from 1905–2019 [54, 55]. For 1941–1945, there is a correction for WWII measurement anomalies [23] of multiplied a constant c_{sea} equal to the fraction 0.7 of earth surface area covered by oceans, resulting in a correction for those years of $ww_2 = -0.31^\circ\text{C}$ and 0 correction in other years. From the discussion in the previous chapter, there are three adjustable parameters that multiply estimates of corrections to the temperature data to account for effects of ENSO, 11 year solar irradiance cycle variations, and large volcanic eruptions. A temperature offset parameter, τ_0 , is also included because the difference between the GISS data set reference temperature and a temperature in equilibrium with radiative forcing of year 1750 is not precisely known [56].

With these corrections, the historical temperature data τ' from 1905 to 2019 can be defined as a function of several adjustable parameters.

$$\tau' = \tau_{gistemp} + c_{sea} * ww_2 - c_{enso} * c_{ensof} * MEI - c_{solar} * c_{solarf} * TSI + c_{volc} * \Delta\tau_{volc} + \tau_0 \quad (4.11)$$

Here $\tau_{gistemp}$ is the raw GISTEMP data before any corrections. As noted above, the temperature correction lag the MEI by four months and the TSI differences from a three-cosine

fit by one month. c_{ensof} and c_{solarf} are $0.08^{\circ}\text{C}/\text{MEI}$ and $0.084^{\circ}\text{C}/\text{TSI}$ respectively, the constant coefficients suggested from Foster and Rahmstorf [16]. $\Delta\tau_{volc}$ is the historical large volcanoes effect on τ shown in figure 3.8. The other time series values of $\tau_{gistemp}$, ww_2 , MEI , TSI are all constants. The adjustable coefficients c_{enso} , c_{solar} , and c_{volc} multiply estimates of corrections to the temperature data to account for effects of ENSO, 11-year solar variations, and large volcanic eruptions respectively.

This corrected historical global mean surface temperature data τ' is calibrated against the analytic solution of τ from equation 4.6 to get the initial trial range for c_1 and c_2 . From the previous discussions, it is known that F depends on c_{reg} . Thus, in order to have estimates of historical total radiative forcing F , trial ranges for c_{reg} from 1 to 1.8 with an increment step of 0.1 are examined along with a set of values of c_1 and c_2 defined in equations 4.9 and 4.10.

4.2.2 Ocean Heat Content

Additional constraints are put on the parameter c_{th} by using the ocean energy budget estimates from 1960 to 2014 that are relative to the 1958–1962 base period as accessed from Cheng et al. (2017) [21]. However, only data from 1995 to 2014 are used because it is better to avoid Pinatubo effects and there are comparatively sparse ocean energy content measurements before that.

The global stored energy change is expressed in units of decaZJ. To convert to W/m^2 per annual decaZJ increase by the earth, a coefficient of c_e needs to be multiplied with the ocean energy budget estimates from Cheng et al. (2017) [21].

$$c_e = 10^{22} / (0.93 \times 5.1 \times 10^{14} \times 365.25 \times 24 \times 3600) = 0.668102 \quad (4.12)$$

Here, it is assumed that approximately 93% of the excess energy is stored in the oceans [21]. The earth surface area is approximated as $5.1 \times 10^{14} \text{ m}^2$. There are approximately 365.25 days every year accounting for leap years, so the number of seconds in a year that is used is 31557600.

Like for τ_0 , an adjustable constant E_0 is added to the ocean energy content data to get the difference in ocean energy content and the ocean energy content that would be in equilibrium with radiative forcing in 1750.

4.3 Prior Probability Distribution for c_{reg}

A log-normal distribution is used as the prior probability distribution for c_{reg} . This distribution is based on the supplementary material to an article by Shindell [53]. That article gives five estimates of the efficacy of radiative forcing from a combination of tropospheric aerosols and ozone. These estimates are not normally distributed about their mean, which suggested use of a log-normal distribution. Also, black carbon on snow is included here in the adjustable radiative forcing, because it is also regionally dependent. Black carbon on snow makes a small contribution to radiative forcing, but that contribution is the opposite sign to that of the sum of tropospheric aerosols and ozone. Thus, the efficacy estimates from Shindell need to be multiplied by a number that is close to but less than 1. That correction factor, 0.865, is the ratio of the radiative forcing for 2011 from tropospheric aerosols and ozone plus black carbon on snow to that just for tropospheric aerosols and ozone, after multiplying the black carbon on snow forcing by an efficacy factor from Hansen et al. [57]. Fitting the results for the largest and smallest estimates from Shindell and assuming they span a 95% confidence interval based on comparisons in Shindell's article with other studies, the result is:

$$p_{reg} = e^{-(1/2)(\ln(c_{reg}) - \mu_{reg})^2 / \sigma_{reg}^2} / (c_{reg} \sigma_{reg} \sqrt{2\pi}) \quad (4.13)$$

where $\mu_{reg} = 0.28$ and $\sigma_{reg} = 0.159$.

4.4 Integration over Nuisance Parameters

4.4.1 Trial Ranges in Orthogonal Coordinates

Before doing integration of a likelihood function given historical global mean surface temperature and ocean heat content data for choices of orthogonal coordinates c_1 and c_2 , the trial ranges for c_1 , c_2 and c_{reg} need to be found. Cases for parameter c_{reg} from 1 to 1.8 with an increment step of 0.1 are examined along with a set of values of c_1 and c_2 .

To be more specific, first select one of the nine different values of c_{reg} with the input historical forcing F represented in equation 4.3. Then, approximate the fitted total radiative forcing F as a exponential function as:

$$F = F_0 e^{\nu(s-270)} \quad \text{for } s=1, \dots, 270 \quad (4.14)$$

where F_0 is the radiative forcing at year 2019 in W/m^2 . ν is a constant growth rate in units of yr^{-1} fit to F . Here, $s = 1$ starts at year 1750, and $s = 270$ ends at 2019. By minimizing the sum of squared errors from F versus the exponential fitted values, fitted values of ν and F_0 are found.

From equation 4.8, we know that $\zeta = \tau_{270}/F_0$, then $c_1 = 1/\zeta$. So, in this way, an estimate of c_1 is obtained. Thus, in our analysis, the initial trial range of c_1 is as follows:

$$c_1 = 0.92 \cdot 1/\zeta + 0.01 \cdot i \cdot (0.92 \cdot 1/\zeta) \quad \text{for } i = 1, \dots, 25 \quad (4.15)$$

There are nine different values of c_{reg} , so the same procedure is carried out to get the corresponding trial ranges for c_1 . Those nine optimum values of ν are all very close to 0.02, so in our analysis, ν is set to be 0.02 as the approximate value of growth rate in yr^{-1} of radiative forcing. This approach is sufficient, since the only use of ν is for helping find approximately an appropriate range of trial values at which likelihood values are calculated.

For the parameter c_2 , the initial trial range is as follows:

$$c_2 = 0.7 + 0.05 \cdot j \quad \text{for } j = 1, \dots, 20 \quad (4.16)$$

Trial ranges for new orthogonal coordinates c_1 and c_2 are found for each one of c_{reg} . This provides us a more efficient way to find values of λ , c_{th} , and c_{reg} that are more likely to give a match to the historical temperature data. It is clear that for each c_0 , there are 25×20 combinations of c_1 and c_2 to be used to generate same amount of pairs of λ and c_{th} for calculation. Thus, in total, there are $9 \times 25 \times 20$ combinations of λ , c_{th} , and c_{reg} used for numerical integration.

4.4.2 Numerical Integration

For nine different cases of c_{reg} , solve the values of λ and c_{th} for each pair of c_1 and c_2 using following equations:

$$\lambda^4/3 - 1 + (c_1 - c_2)\lambda = 0 \quad (4.17)$$

The real and positive root of this quadratic equation is chosen. Also,

$$c_{th} = (c_1 - 1/\lambda)/\nu \quad (4.18)$$

Here, $\nu=0.02$.

Then plug in solved λ and c_{th} in equation 4.6 to get the estimates of τ from 1905 to 2019. Also, from Cheng et al. (2017), the ocean energy budget from 1995 to 2014 data are used together with the same period of estimates of τ . Therefore, there are totally 20 data points here to calibrate ocean heat content.

For the first ocean heat content data in year 1995, white noise error is assumed as follows:

$$\epsilon_{E_1} = E_1 - c_{th}\tau_{91} + E_0 \quad (4.19)$$

Ocean thermal energy change is subtracted by $c_{th}\tau$, with the adjustable parameter E_0 added. The constant E_0 is an a priori uncertain difference between the global energy content change from a later base period versus a value in equilibrium with radiative forcing in 1750. τ_{91} is the temperature data in year 1995.

For the other 19 data points, ϵ_E follows a moving average of order 1 (MA1) recursion

formula. A statistical test on autocorrelations of residuals has been done to check this approach to the time series model for accounting the correlated residuals. By looking at autocorrelation function (ACF) and partial autocorrelation function (PACF) plots, it is suggested that a MA1 model is sufficient for the correlated residuals from ocean heat content data [58].

$$\epsilon_{E_{m+1}} = E_{m+1} - c_{th}\tau_{91+m} - \theta\epsilon_{E_m} + E_0, \quad \text{for } m=1, \dots, 19 \quad (4.20)$$

Moving average autocorrelation affects the size of confidence contours for the model parameters, and example of which will be plotted below in subsection 4.6.2.

For the global average temperature data, moving average autocorrelation effects did not need to be included, which greatly simplified the analysis. Since the purpose of the exercise was to sample a probability distribution for extrapolating averages over transients and random fluctuations of future global average temperature observations, the statistical model used here was sufficient.

The notation τ_{91+m} indicates that the 20 values of E_n start at the time corresponding to the 91th time in the series of annual values of τ_m which is equal the τ at year 1995. It is assumed that ϵ_{E_1} is normally distributed with zero mean, i.e. $N(0, \sigma_2^2)$.

Similarly, for the estimates of τ from 1905 to 2019, there are also residuals by subtracting the estimates of τ from τ' data. Let ϵ_{τ_n} represents the residuals from global mean surface temperature:

$$\epsilon_{\tau_n} = \tau_n - \tau', \quad \text{for } n=1, \dots, 115 \quad (4.21)$$

Here, ϵ_τ follows $N(0, \sigma_1^2)$. $n = 1$ means counts start at year 1905, and $n = 115$ means counts end at year 2019.

Then, the sum of squares of ocean heat content residuals can be obtained as $\epsilon_E \cdot \epsilon_E$, where ϵ_E is vector of the ϵ_{E_m} for 1995 to 2014. Similarly, the sum from 1905 to 2019 of squares of global mean surface temperature residuals is obtained as $\epsilon_\tau \cdot \epsilon_\tau$.

For the parameters σ_1 and σ_2 in the following expression for probability, uninformative

prior probability distributions of $1/\sigma_1$ and $1/\sigma_2$ are used respectively [59]. Then

$$L = \left(\prod_{i=1}^N p_n\right) \left(\prod_{n=1}^M q_m\right) / (\sigma_1 \sigma_2) \quad (4.22)$$

where $N=115$, and $M=20$. Here, p_n are likelihoods for the yearly global mean surface temperature data from 1905 to 2019. The q_m are likelihoods for the accumulated yearly ocean heat content data from 1995 to 2014. Thus,

$$p_n = (2\pi\sigma_1^2)^{-1/2} e^{-(1/2)\epsilon_{\tau_n}^2/\sigma_1^2}, \quad \text{for } n=1, \dots, 115 \quad (4.23)$$

and

$$q_m = (2\pi\sigma_2^2)^{-1/2} e^{-(1/2)\epsilon_{E_m}^2/\sigma_2^2}, \quad \text{for } m=1, \dots, 20 \quad (4.24)$$

For each set of trial values of λ , c_{th} , and c_{reg} , the likelihood function L is integrated analytically over σ_1 and σ_2 giving a result proportional to [59]:

$$(\epsilon_{\tau} \cdot \epsilon_{\tau})^{-n_{\tau}/2} (\epsilon_E \cdot \epsilon_E)^{-m_E/2} \quad (4.25)$$

where $n_{\tau} = 115$, and $m_E = 20$.

Then, in order to get an appropriate integration range for unknown parameters τ_0 and E_0 , the previous least square fits for τ_0 and E_0 are plugged into the expression 4.25 along with other nuisance parameters. Maximum likelihood value of τ_0 and E_0 will be the center point of interval for numerical integration over those parameters.

Add and subtract $\delta E_0 = 4.5$ and $\delta \tau_0 = 0.045$ around the center point of E_0 and τ_0 to get integration intervals for τ_0 and E_0 . That results in integration ranges that are large enough, but not so large that the integration method fails to converge too often.

Finally, the expression is integrated numerically over θ , E_0 , τ_0 , c_{enso} , c_{solar} , and c_{volc} , in total 6 parameters. For the integration parameters other than τ_0 and E_0 , failure of the integration method to converge due to too wide an integration method did not prove to be a significant problem. By varying upper and lower bounds, adjustable parameters c_{enso} , c_{solar} , and c_{volc} were found.

The number of resulting integrals is $9 \times 25 \times 20$. Denote the resulting integrals as P_{kij} where $k=1,\dots,9$, $i=1,\dots,25$, and $j=1,\dots,20$.

There are in total nine parameters in the expression for L that are adjustable. All nine parameters except λ , c_{reg} and c_{th} are nuisance parameters, and are to be integrated over numerically.

4.5 Gaussian Fit to Marginal Posterior Probability

In the last section, the numerical integrals P_{kij} are described. Only points for which the probability is greater than 0.0001 times the maximum probability for each column of the integrated probabilities matrix are kept.

Then, do Gaussian fitting to the numerical integrals of probabilities obtained above. Let

$$\delta_{kij} = P_{kij} - b_1 e^{-0.5 \left((c_{1,i} - b_2) / b_3 \right)^2} \quad \text{for } k = 1, \dots, 9, i = 1, \dots, 25, \text{ and } j = 1, \dots, 20 \quad (4.26)$$

For each k and j , find values of b_1 , b_2 , and b_3 that minimize the sum of the squares of δ_{kij} . Here b_1 is the height of a Gaussian function, b_2 is the shift of the Gaussian function, and b_3 is the width of the Gaussian function.

The starting searching points for height parameters b_1 are set to be the maximum values of probability numbers in each column. For the b_2 parameters, the starting points for search shift parameters are equal to the maximum over each column, for each different pair of c_2 and c_{reg} . The starting searching points for width parameters b_3 are as follows:

$$0.037 - 0.001k + 0.0002j \quad \text{for } k=1,\dots,9, \text{ and } j = 1, \dots, 20 \quad (4.27)$$

For a fixed set of c_{reg} and c_2 , then fit each column to a Gaussian function, and search the optimum parameters of b_1 , b_2 and b_3 from the starting points that are found before, then minimize the sum of squared errors δ_{kj}^2 to get the best estimates. Thus, each column is fitted by a Gaussian function. Each set of three fitted parameters b_1 , b_2 and b_3 is recorded for further analysis in the next section.

Parameters that can be used to construct a marginal posterior probability function as a function of orthogonal coordinates c_1 and c_2 , and c_{reg} are found here. This is done in two steps. First of all, the Gaussian fits found in the previous section for each column of probabilities numbers are used here.

For the parameter b_1 , in order to find an appropriate Gaussian function to fit it, probabilities less than 0.001 times the maximum for the same value of c_{reg} will not be used, in order to avoid multiple irrelevant points affecting the fit. Thus, the points that are used to be find a Gaussian fit for b_1 are found as well as the corresponding relevant range of c_2 .

For each k , i.e. a fixed c_{reg} , Gaussian least squares fits to the amplitudes b_1 are of the form

$$b_1 = d_{11}e^{-0.5(c_2-d_{12})^2/d_{13}} \quad \text{for } k=1, \dots, 9 \quad (4.28)$$

Quadratic fits to the shift b_2 are of the form

$$b_2 = d_{21} + d_{22}(c_2 - d_{23})^2 \quad \text{for } k=1, \dots, 9 \quad (4.29)$$

Linear fits to the width b_3 are of the form.

$$b_3 = d_{31} + d_{32}c_2 \quad \text{for } k=1, \dots, 9 \quad (4.30)$$

where d_{31} is intercept and d_{32} is the slope.

Then least squares fits as functions of c_2 are found for the parameters denoted here as d_{11} , d_{12} , d_{13} , d_{21} , d_{22} , d_{23} , d_{31} and d_{32} respectively.

As noted above, c_{reg} is taken to have a log-normal prior distribution shown in equation 4.13. The nine trial values of c_{reg} are plugged into this prior distribution to update the parameter d_{11} . The resulting fits of d_{11} are multiplied by the prior probability distribution for c_{reg} to get an analytic function proportional to the joint marginal posterior probability of the data as a function of λ , c_{th} , and c_{reg} .

Join the updated estimates of d_{11} with all the other parameters estimates such as d_{12} , d_{13} , d_{21} , d_{22} , d_{23} , d_{31} and d_{32} , then, fit those estimates with respect to parameter c_{reg} .

To be more specific, for the three parameters in amplitude fits, fit updated d_{11} with a

Gaussian function of e_{111} , e_{112} and e_{113} like the following:

$$d_{11} = e_{111} e^{-\frac{1}{2} \left(\frac{c_{reg} - e_{112}}{e_{113}} \right)^2}$$

Then, fit d_{12} with a quadratic function of e_{121} , e_{122} and e_{123} .

$$d_{12} = e_{121} + e_{122} (c_{reg} - e_{123})^2$$

Fit d_{13} with a quadratic function of e_{131} , e_{132} and e_{133} .

$$d_{13} = e_{131} + e_{132} (c_{reg} - e_{133})^2$$

For the three parameters in shift fits, fit d_{21} with a linear function of e_{211} , e_{212} .

$$d_{21} = e_{211} + e_{212} c_{reg}$$

Then, fit d_{22} with a quadratic function of e_{221} , e_{222} and e_{223} .

$$d_{22} = e_{221} + e_{222} (c_{reg} - e_{223})^2$$

Fit d_{23} with a quadratic function of e_{231} , e_{232} and e_{233} .

$$d_{23} = e_{231} + e_{232} (c_{reg} - e_{233})^2$$

For the two parameters in width fits, fit d_{31} as a constant as e_{311} . Here, the constant is the average of the values of d_{31} , because the variation on the ordinate is small and there no obvious parsimonious (small number of parameters) alternative formula that is appropriate.

Then, fit d_{32} with a linear function of e_{321} and e_{322} as follows:

$$d_{32} = e_{321} + e_{322} c_{reg}$$

Each set of those fitted parameters are recorded for further analysis in next section. Table

4.1 includes the fitted values of the e_{ijk} 's.

Table 4.1: Marginal Posterior Probability Function Fitting Parameters

Symbol	Value	Description
e_{111}	102.36	amplitude
e_{112}	1.30	shift
e_{113}	0.19	width
e_{121}	0.91	intercept
e_{122}	0.36	amplitude
e_{123}	0.93	shift
e_{131}	0.003	intercept
e_{132}	0.012	amplitude
e_{133}	1.056	shift
e_{211}	2.547	intercept
e_{212}	-0.563	slope
e_{221}	-0.119	intercept
e_{222}	0.278	amplitude
e_{223}	1.238	shift
e_{231}	1.228	intercept
e_{232}	1.661	amplitude
e_{233}	1.515	shift
e_{311}	0.026	constant
e_{321}	0.024	intercept
e_{322}	-0.013	slope

4.6 3-D Maximum Marginal Probability and Sampling

In this section, use input parameters from last section to construct a marginal posterior probability function as a function of orthogonal coordinates c_1 , c_2 , and c_{reg} . Find its maximum and use a rejection method to find random samples and convert the results to values of λ , c_{th} and c_{reg} .

4.6.1 Maximum Marginal Posterior Probability Parameters

First of all, find the values of λ , c_{th} , and c_{reg} that maximize the marginal posterior probability distribution. Values of these parameters are listed in Table 4.2.

Table 4.2: Maximum Marginal Posterior Probability Parameters Values

Symbol	Value	Units	Description
λ	0.91	$^{\circ}\text{C}/(\text{W}/\text{m}^2)$	Climate sensitivity
c_{reg}	1.30	1	Regionally dependence industrial forcing efficacy
c_{th}	35.17	$(\text{W}/\text{m}^2) \text{ yr}/^{\circ}\text{C}$	Thermal inertia parameter

Figure 4.1 shows how the maximum marginal posterior probability case fits the historical data with ENSO, 11 year solar cycle, and large volcano effects on temperature removed from the data. Since the values of λ , c_{th} , and c_{reg} listed in Table 4.2 result from an integration over nuisance parameters that include τ_0 , c_{enso} , c_{solar} , and c_{volc} no specific values of those parameters are associated with the smooth curve in figure 4.1 except for a very weak dependence on c_{volc} . However, for the jagged line in that figure, specific values of those parameters are chosen by fixing the parameters in Table 4.2 and then maximizing the probability given in equation 4.22.

4.6.2 Random Samples

Find the leading coefficient in a normalized probability function that integrates to very close to 1. Then, the number of values of λ for which probability formulas were computed is 161, and 119 for c_{th} , and 85 for c_{reg} , giving a total of 1,628,515 combinations of these parameters. Figure 4.2 below shows the 3-D contour plot which cover 50% of the total probability in orthogonal coordinates of c_1 and c_2 . Use rejection sampling to randomly pick 98 samples of these combinations that lie within a 99% contour. The portion of those 98 random samples that lie outside of the 50% contour are visible as dots in figure 4.2.

Then, solve as above for λ and c_{th} for each of the samples using equations 4.17 and 4.18 and plot in figure 4.3 the same 98 samples shown in figure 4.2, but in original coordinates

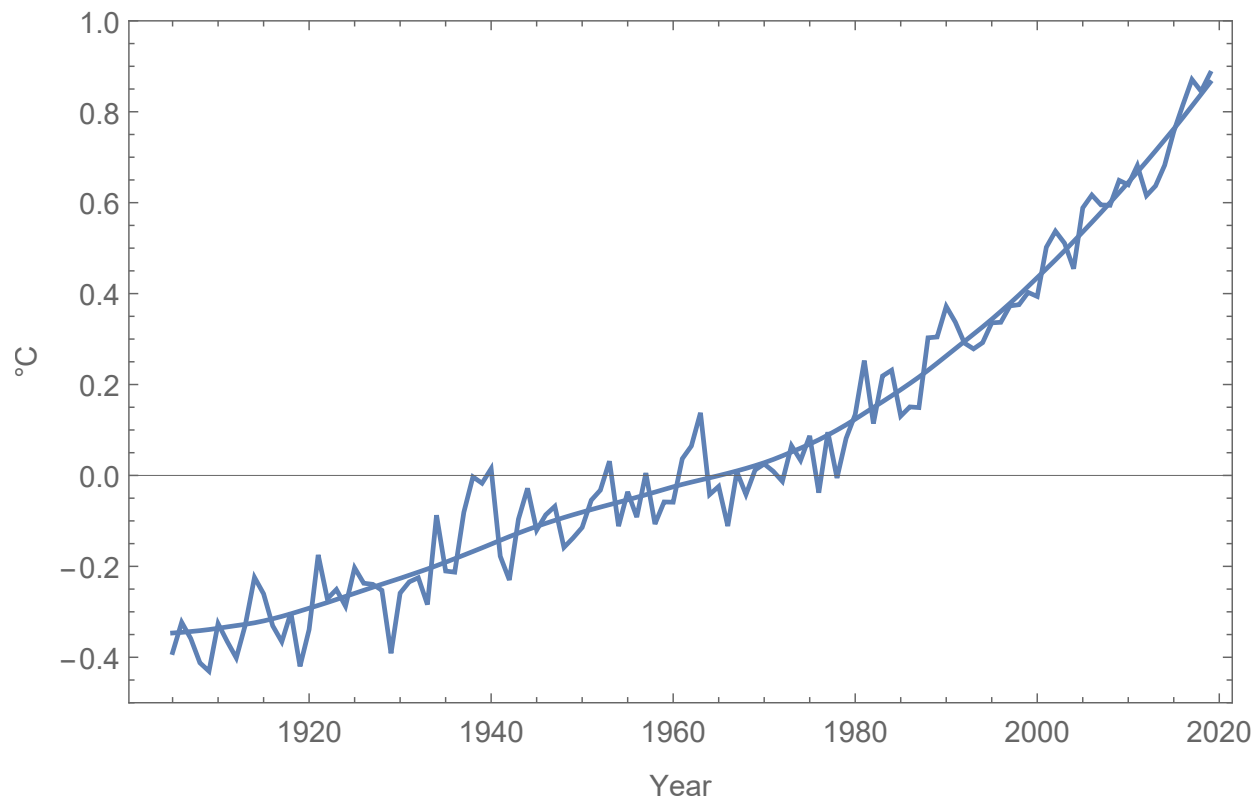


Figure 4.1: The maximum marginal posterior probability case fits versus the adjusted historical temperature data.

of λ , c_{th} , and c_{reg} .

Figure 4.3 shows the 98 random samples picked distribute in the 3-D space defined by λ , c_{th} , and c_{reg} .

The graphs in figures 4.4–4.9 indicate that there is a range of sets of values of λ , c_{th} , and c_{reg} sampled from their probability distribution that lead to comparable fits to transient-adjusted global average temperature data.

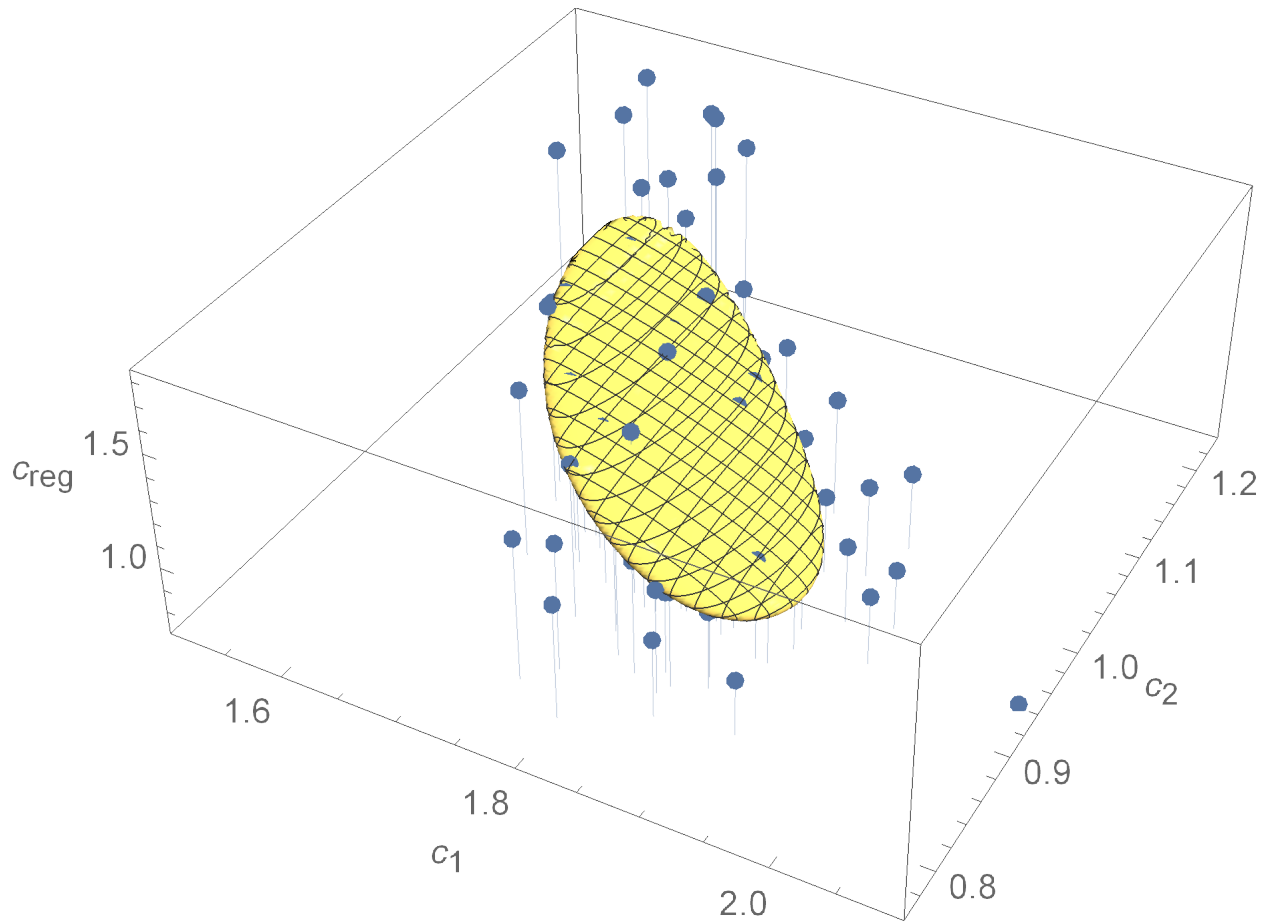


Figure 4.2: 3-D contour plot covering half of the total probability space shown in transformed coordinates of c_{reg} , c_1 and c_2 .

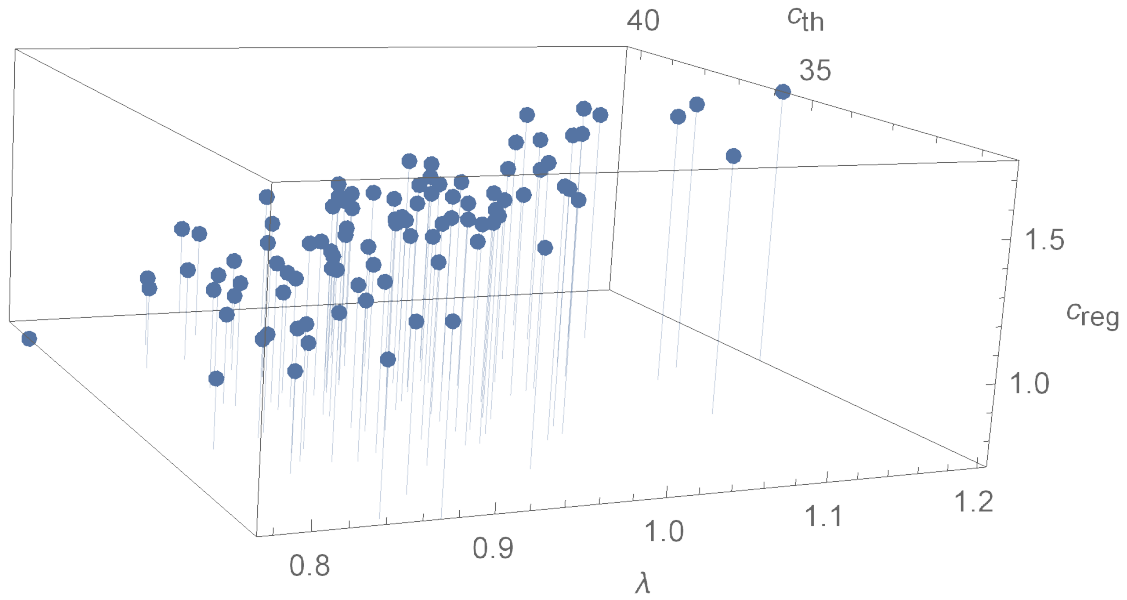


Figure 4.3: 98 samples that cover 99% of the total probability space shown in original coordinates of λ , c_{th} , and c_{reg} .

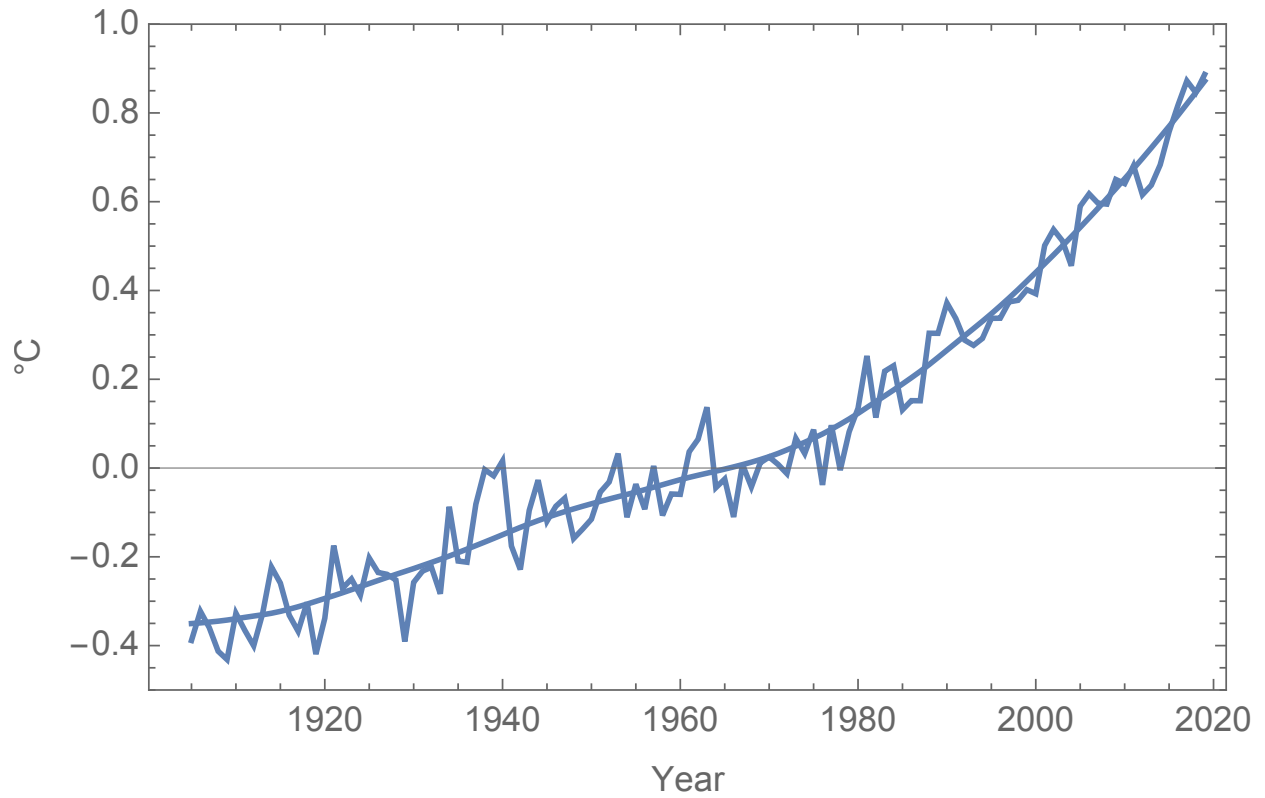


Figure 4.4: The first of 98 samples of λ , c_{th} , and c_{reg} fit versus the adjusted historical temperature data.

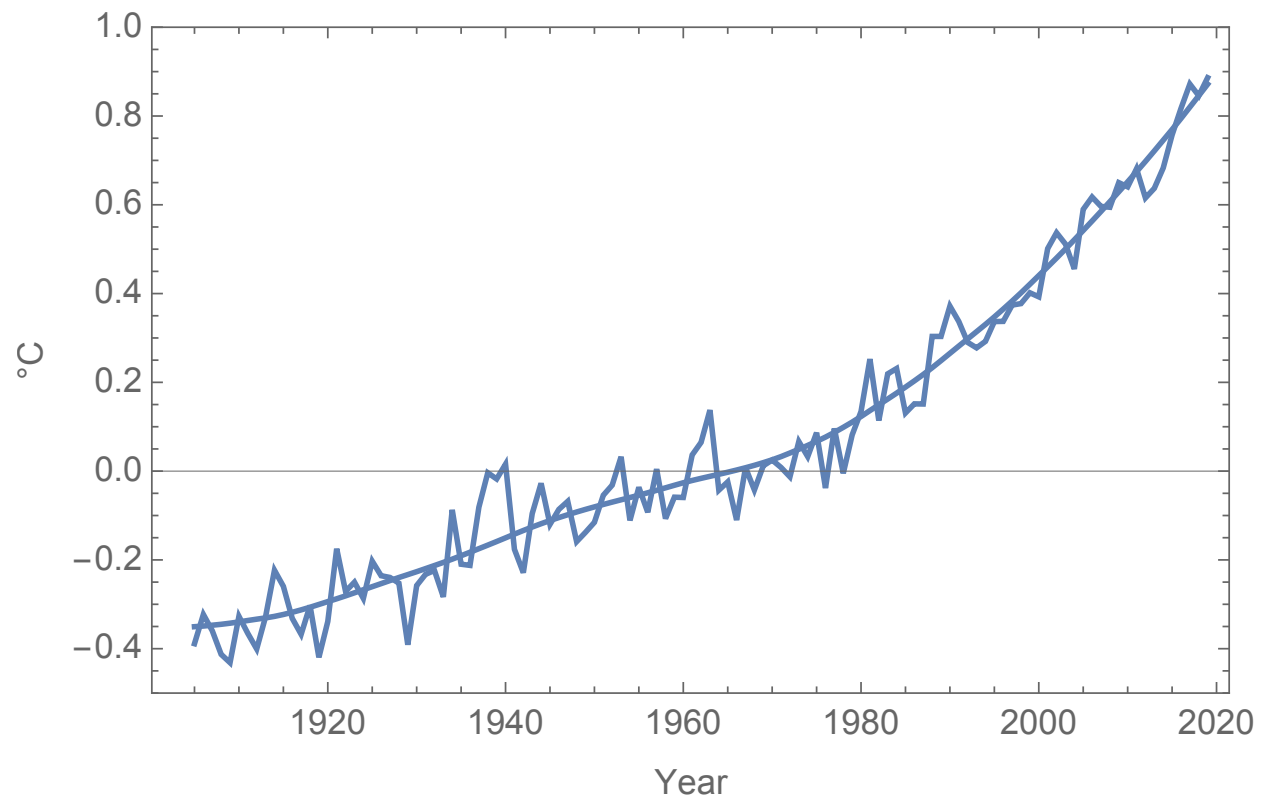


Figure 4.5: The second of 98 samples of λ , c_{th} , and c_{reg} fit versus the adjusted historical temperature data.

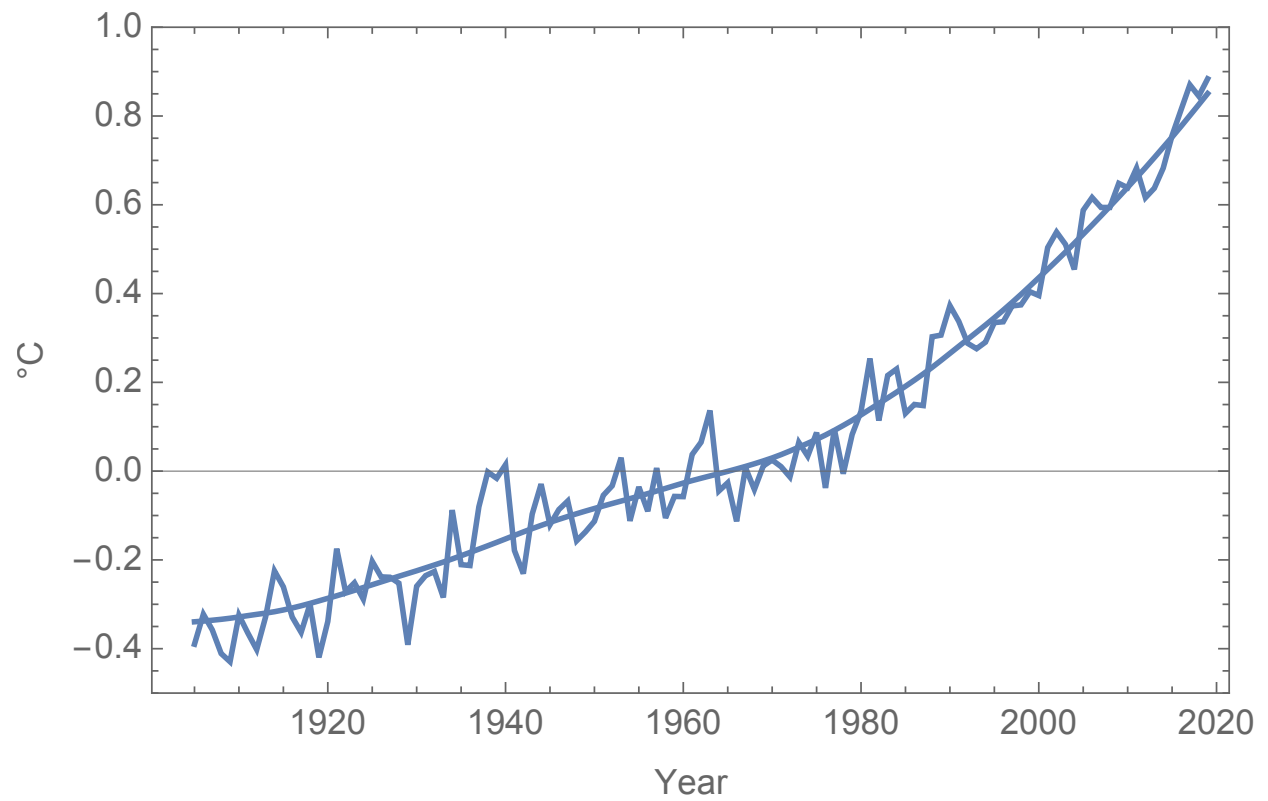


Figure 4.6: The third of 98 samples of λ , c_{th} , and c_{reg} fit versus the adjusted historical temperature data.

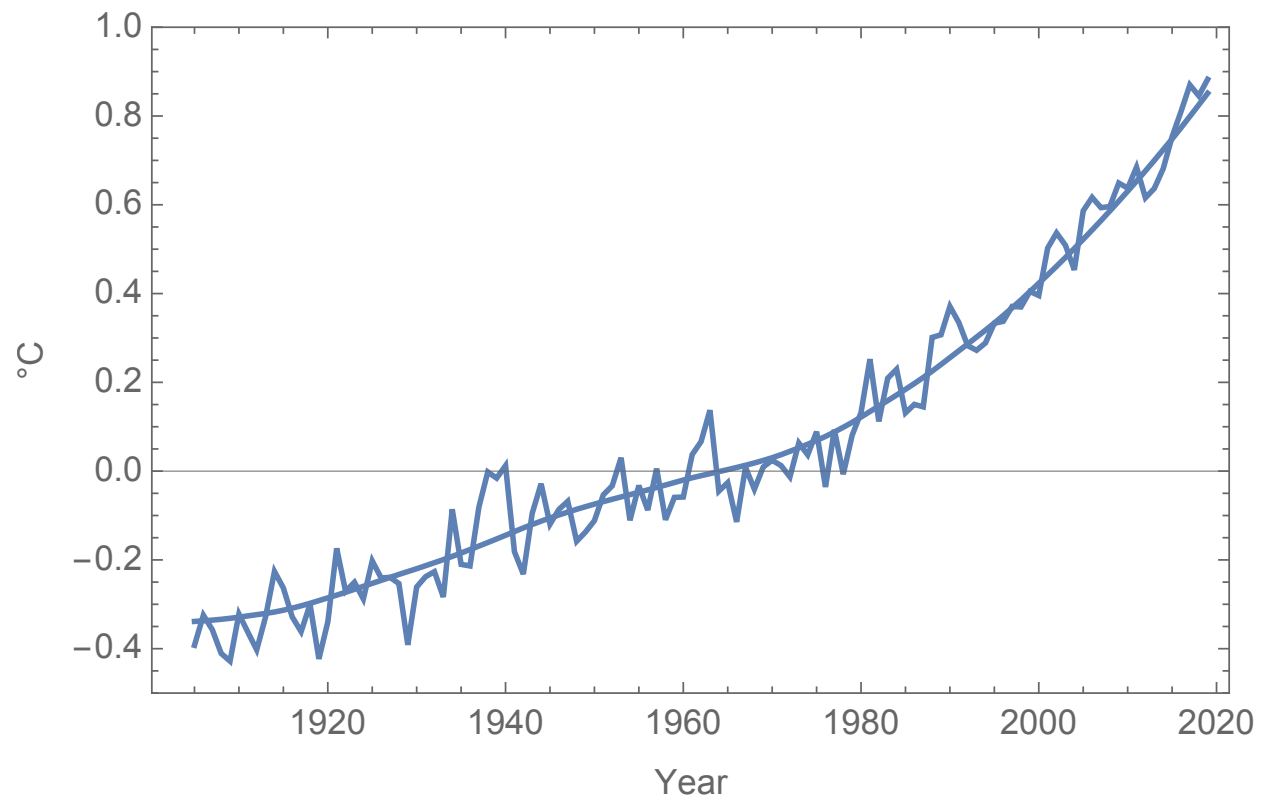


Figure 4.7: The fourth of 98 samples of λ , c_{th} , and c_{reg} fit versus the adjusted historical temperature data.

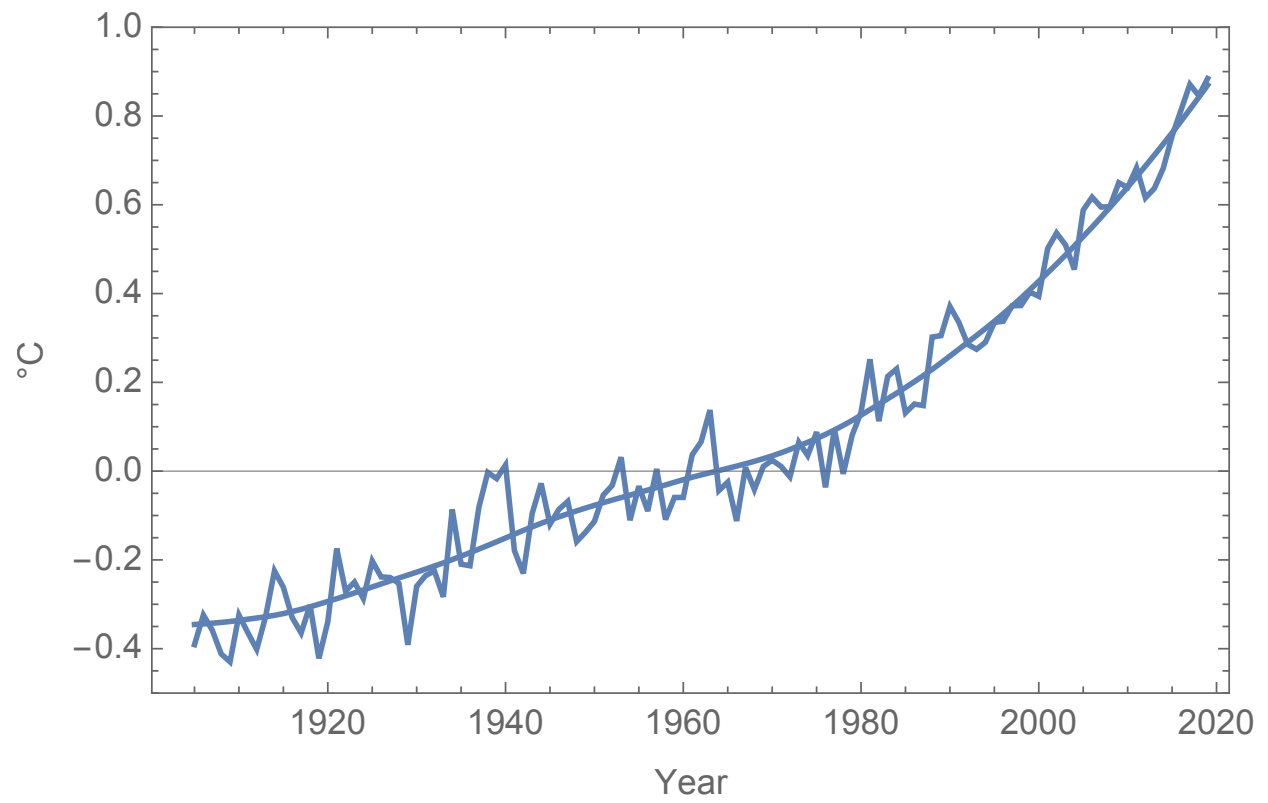


Figure 4.8: The fifth of 98 samples of λ , c_{th} , and c_{reg} fit versus the adjusted historical temperature data.

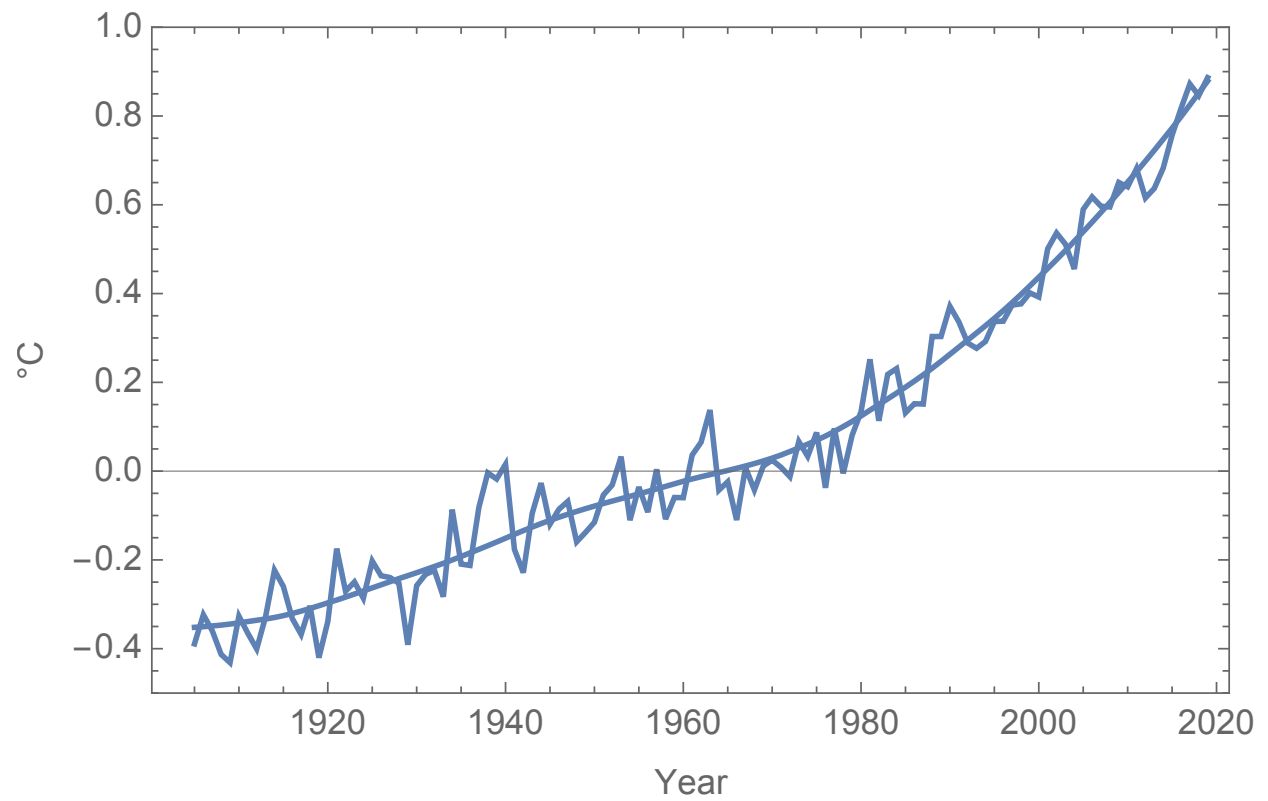


Figure 4.9: The sixth of 98 samples of λ , c_{th} , and c_{reg} fit versus the adjusted historical temperature data.

CHAPTER 5

RADIATIVE FORCING AND GLOBAL AVERAGE TEMPERATURE EXTRAPOLATIONS

The purpose of this exercise is to find and sample a probability distribution for use in extrapolating global average temperature responses to future changes in radiative forcing. However, averages over transient effects are assumed to have zero mean.

This chapter extrapolates the maximum marginal posterior case and an input set of random samples of λ , c_{th} , and c_{reg} . Then, it plots the maximum probability case and some random sample cases of the evolution of radiative forcing and the increase in global average temperature over its year 2019 value. Finally, it finds the cumulative probability distribution for that increase in a future year.

First of all, the random 98 samples picked in the previous chapter are used here along with a set of λ , c_{th} , and c_{reg} in Table 4.2 that maximize the joint marginal posterior probability distribution. So, there are in total 99 cases of λ , c_{th} , and c_{reg} used in this part.

The starting point for the extrapolation exercise is fits to historical data for use in extrapolating contributions to radiative forcing. For this purpose, define a unit logistic function as follows:

$$u = \frac{1}{1 + e^{-(t-a_1)/a_2}} \quad (5.1)$$

Here, the a_1 is the inflection point and a_2 is the inverse of the early logistic function growth rate.

The time derivative of above unit logistic function is proportional to:

$$\frac{1}{1 + e^{-(t-a_1)/a_2}} \left(1 - \frac{1}{e^{-(t-a_1)/a_2}} \right) = u(1 - u) \quad (5.2)$$

Logistic functions are used for N_2O and CH_4 emissions, halogen, land use change effects including albedo, and contrail forcing, and for industrial atmospheric carbon emissions.

Functions proportional to the time derivative of a logistic function are used for two additive functions for carbon emissions from land use, and also for radiative forcing from the regionally inhomogeneous adjustable contribution shown in figure 3.14. Using extrapolations of emissions, atmospheric balance equations for CO₂, N₂O and CH₄ are solved for their concentrations, and radiative forcing formulas are used based on those concentrations. All contributions to radiative forcing are increases over year 1750 values.

First of all, fit the historical contributions to non-adjustable anthropogenic radiative forcing and the adjustable forcing from 1750 to 2019. Then, multiply the adjustable forcing by c_{reg} and add the result to the non-adjustable forcing. Then, solve the global heat balance equation for τ driven by the radiative forcing of non-adjustable anthropogenic and adjustable radiative forcing by solving the following equation,

$$\frac{d\tau}{dt} = (F - \tau/\lambda)/c_{th} \quad (5.3)$$

with the initial condition of $\tau=0$ at year 1750.

Plug the previous 99 sets of λ , c_{th} , and c_{reg} into the above global heat balance equation, and solve the 99 results of τ at year 2019. Later on, those values will be used as starting values for extrapolations.

5.1 Extrapolate Atmospheric Concentration of Nitrous Oxide and Methane

Logistic fits are made to nitrous oxide and methane emissions by finding logistic function parameters and initial atmospheric concentrations X_0 that produce a least squares fit to residuals between data and analytic solutions for atmospheric concentrations X of the balance equations:

$$dX/dt = S_X - X/t_X \quad (5.4)$$

where $t_X=116$ years for N₂O and 9.1 years for CH₄ from IPCC WG1 AR6. In view of the lower temporal resolution of the ice core data used before 1978, only every fifth data point is used from 1752–1977. Annual estimates of global average concentrations based on direct

atmospheric concentrations are used from 1978–2019.

Table 5.1 shows the parameters used when calculating the source term S_X , i.e. annual emissions of N_2O and CH_4 . Here, S_X takes a form of constant times a unit logistic function which is defined in equation 5.1.

Table 5.1: Parameters in N_2O and CH_4 Emission Equations

Symbol	Value	Units	Description
a_{n1}	4.949	ppb/yr	N_2O maximum emission rate
a_{n2}	2059.82	Julian year	inflection time of N_2O emission
a_{n3}	50.7557	year	the inverse of logistic growth rate of N_2O emission
a_{m1}	135.6	ppb/yr	CH_4 maximum emission rate
a_{m2}	1955.26	Julian year	inflection time of CH_4 emission
a_{m3}	26.37	year	the inverse of logistic growth rate of CH_4 emission
X_{0m}	778.638	ppb	atmospheric concentrations of CH_4 at 1750
X_{0n}	270.581	ppb	atmospheric concentrations of N_2O at 1750

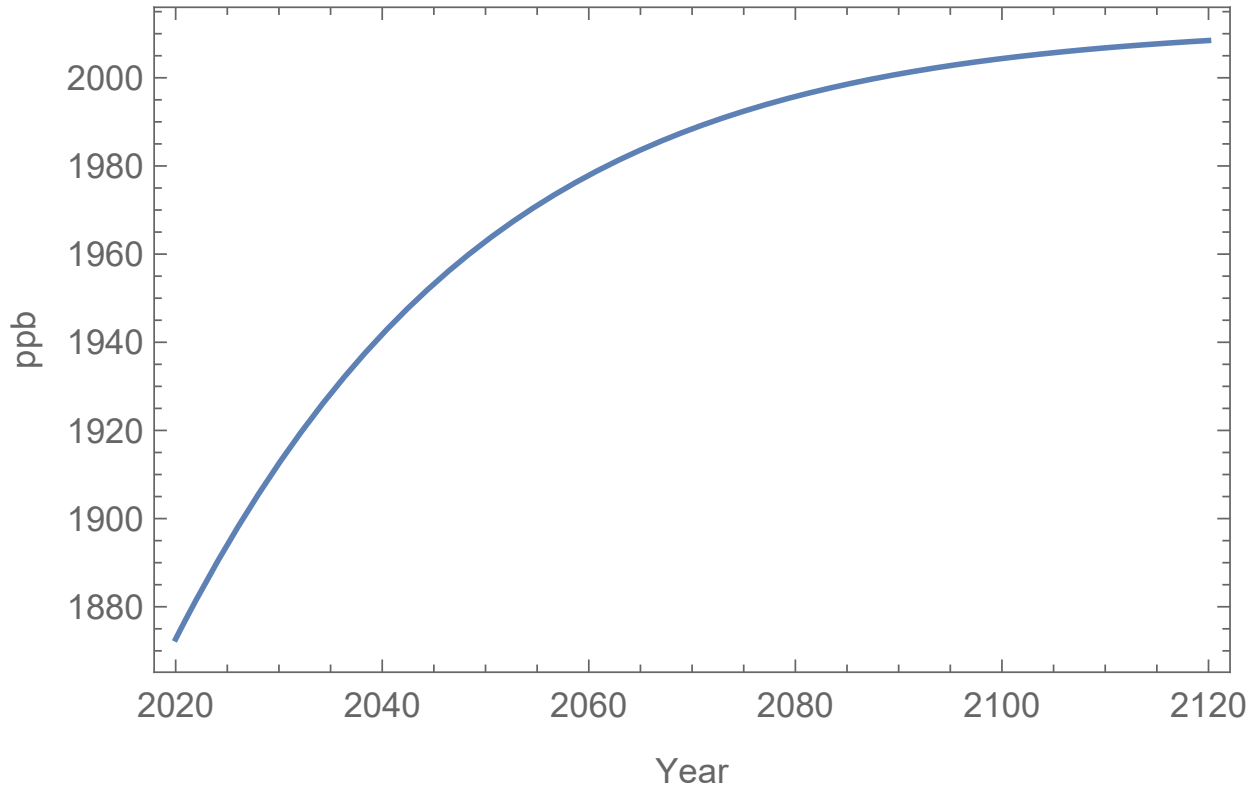


Figure 5.1: Extrapolation of CH_4 concentration from 2020 to 2120.

Figure 5.1 shows the extrapolated methane atmospheric concentration from 2020 to 2120 in ppb.

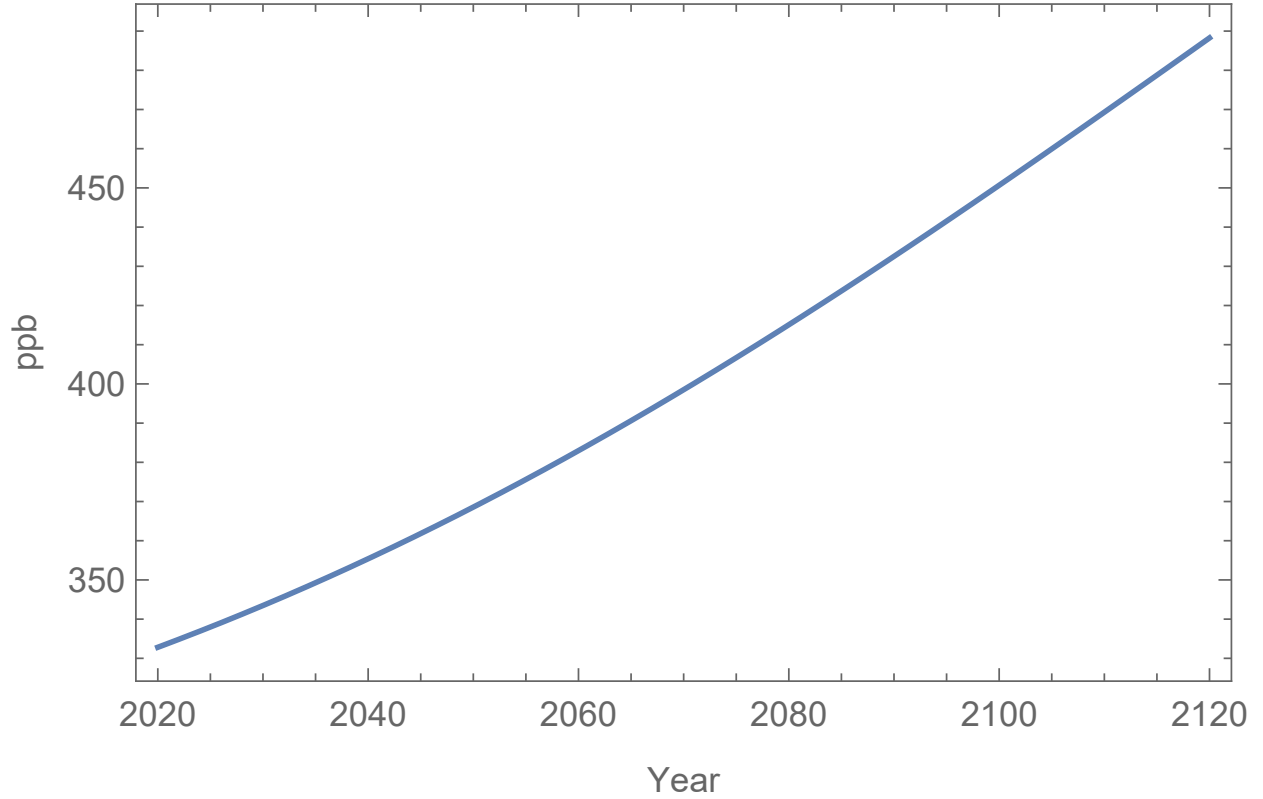


Figure 5.2: Extrapolation of N₂O concentration from 2020 to 2120.

Figure 5.2 shows the extrapolated N₂O atmospheric concentration from 2020 to 2120 in ppb.

5.2 Extrapolate Atmospheric Carbon Content and Carbon Dioxide Concentration

In this analysis, a new carbon balance model is used which allows modeling the case when there is substantial CO₂ atmospheric concentration reduction after substantial reduction of emissions [60].

The carbon content of CO₂ emissions e_c is as follows:

$$e_c = c_3 u_1 + c_4 u_2 (1 - u_2) + c_5 u_3 (1 - u_3) \quad (5.5)$$

where u_1 , u_2 and u_3 are unit logistic function defined in equation 5.1 but with different parameters. c_3 , c_4 and c_5 are constants. The parameters used in equation 5.5 are shown in Table 5.2.

Table 5.2: Carbon Emissions Fitting Parameters

Symbol	Value	Units	Description
c_3	0.015	TtonneC/yr	Long term limit of emission rate
a_{31}	2002.57	Julian year	Date of the maximum emission rate
a_{32}	27.82	year	Time scale in years
c_4	0.006	TtonneC/yr	Four times maximum of emission rate
a_{41}	1950.98	Julian year	Date of the maximum emission rate
a_{42}	46.1959	year	Time scale in years
c_5	0.00297	TtonneC/yr	Four times maximum of emission rate
a_{51}	2021.63	Julian year	Date of the maximum emission rate
a_{52}	8.91425	year	Time scale in years

The anthropogenically emitted carbon has three destinations. Part of it is promptly and permanently sequestered. The rest partly goes into the atmosphere and then gradually exchanges into a non-atmospheric reservoir. These amounts in each are respectively designated here as a and s . The governing equations for a and s are:

$$ds/dt = \nu(f_{sa}a - s) \quad (5.6)$$

$$da/dt = f_e e_c - ds/dt \quad (5.7)$$

Here e_c is emissions in TtonneC/yr. The constant ν is 0.01285/yr, which is the rate to reach equilibrium between a and s . Without emissions, the system reached a steady state eventually with a constant ratio $f_{sa} = s/a$ is 1.53, represents s/a ratio in equilibrium. a_0 is 0.592, the year 1750 atmospheric carbon content in CO₂.

A fraction $(1-f_e)$ of the carbon emissions e_c promptly goes somewhere where it is never accessible for exchange into the atmosphere. The rest, $f_e e_c$, partitions between the atmosphere and a reservoir that contains an amount s . Some of s is in the part of the ocean not

right near the surface, and the rest is on land. It is assumed the fraction $1-f_e$ goes either with cold or salty water that sinks into the deep ocean, or is trapped in soil that was formed when the atmospheric CO_2 concentration was lower than in the industrial era. Up to 1750, a and s are assumed to be constant with ratio f_{sa} of amount in s to amount in a . The content in s increases because a increases as anthropogenic carbon emissions grow. So, the rate of change for s is shown as equation 5.6. That flow of carbon into reservoir s decreases the rate of growth of a below $f_e e_c$ to give equation 5.7.

The fraction f_e of emissions that partition between a and s is

$$f_e = f_m + (1 - f_m)(1 - e^{-(b-b_m)^2}) \quad (5.8)$$

where $b = a/a_0$ and b_m is 0.65. Initially, a fraction $1-0.6=0.4$ of the emitted carbon promptly becomes permanently unavailable ever to enter either the atmosphere or the reservoir containing s . As emissions continue, the place where the fraction $(1 - f_e)e_c$ goes apparently gradually approaches being saturated, since in limit of very large a and $b - a/a_0$ gives $f_e \rightarrow 1$ from equation 5.8.

These numbers are chosen to match historical data on atmospheric CO_2 concentrations and those of Jones et al. [60] for simulations of the evolution of atmospheric carbon content after a hypothetical abrupt future termination of anthropogenic CO_2 emissions [60].

Figure 5.3 shows the extrapolation of CO_2 atmospheric concentration from 2019 to 2120.

5.3 Major Greenhouse Gases Radiative Forcing Extrapolations

In this section, radiative forcing of CO_2 , CH_4 and N_2O is computed using Butler and Montzka formulas [31]. The method used here are the same as what was used in Ding (2018) section 4.4 [29].

Figure 5.4 shows the extrapolation of CO_2 radiative forcing from 2019 to 2120. From this figure, the radiative forcing of CO_2 increases steadily from 2 W/m^2 to over 5 W/m^2 , and thus CO_2 is always the most important factor to cause global warming.

Equation 3.5 is used to extrapolate N_2O radiative forcing. Similarly, equation 3.3 is used

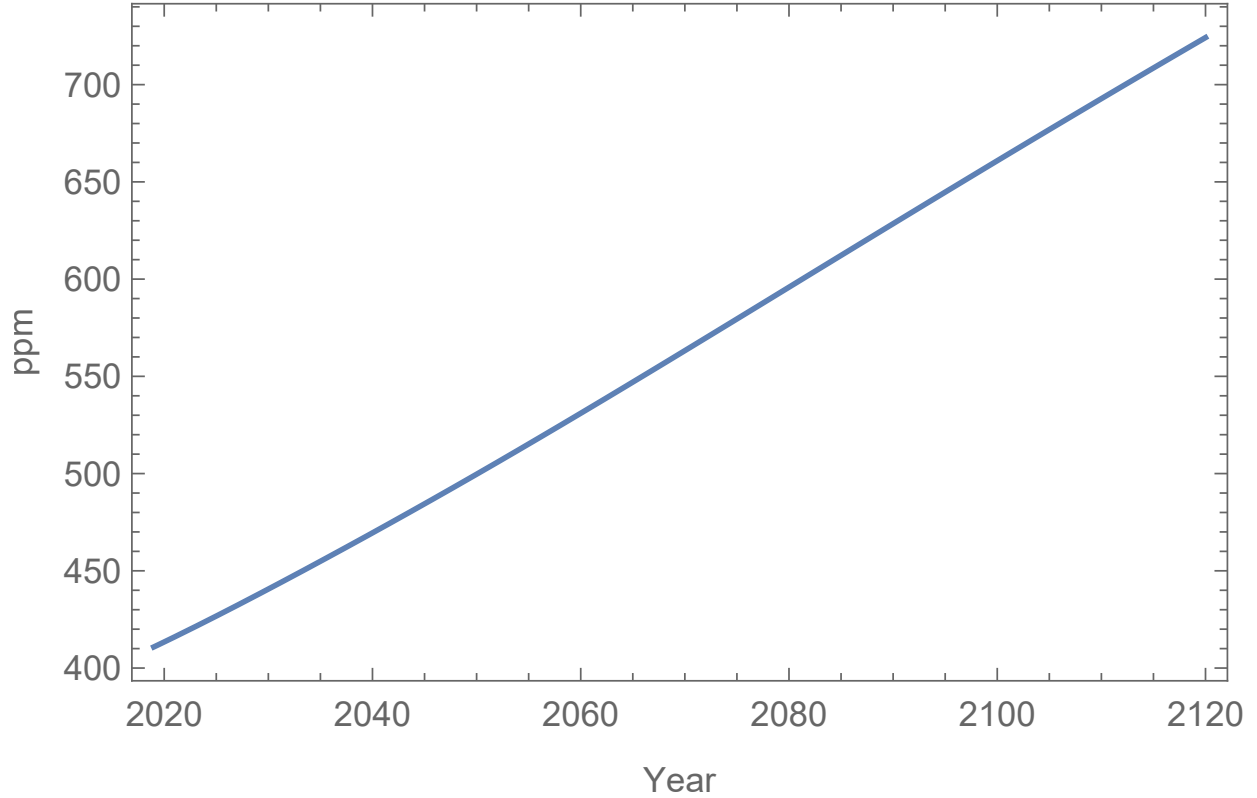


Figure 5.3: Extrapolation of CO₂ atmospheric concentration from 2019 to 2120.

to extrapolate CH₄ radiative forcing.

Figure 5.5 shows the extrapolation of CH₄ and N₂O radiative forcing from 2019 to 2120. In the beginning, the radiative forcing from N₂O is less than CH₄, however, the forcing from N₂O increases much faster than CH₄, and takes over CH₄ before year 2095. CH₄ radiative forcing is almost saturated by 2019 and does not change very much when extrapolated.

5.4 Extrapolations of F and τ for 21 Cases

In this section, the case of λ , c_{th} , and c_{reg} which gives maximum joint probability is extrapolated along with the first 20 random samples of those 98 samples found as described above.

Figure 5.6 shows 21 cases of extrapolated total radiative forcing relative to year 1750. The maximum joint probability case is plotted in red. The most probable extrapolated radiative forcing reached in year 2120 is 6.5 W/m².

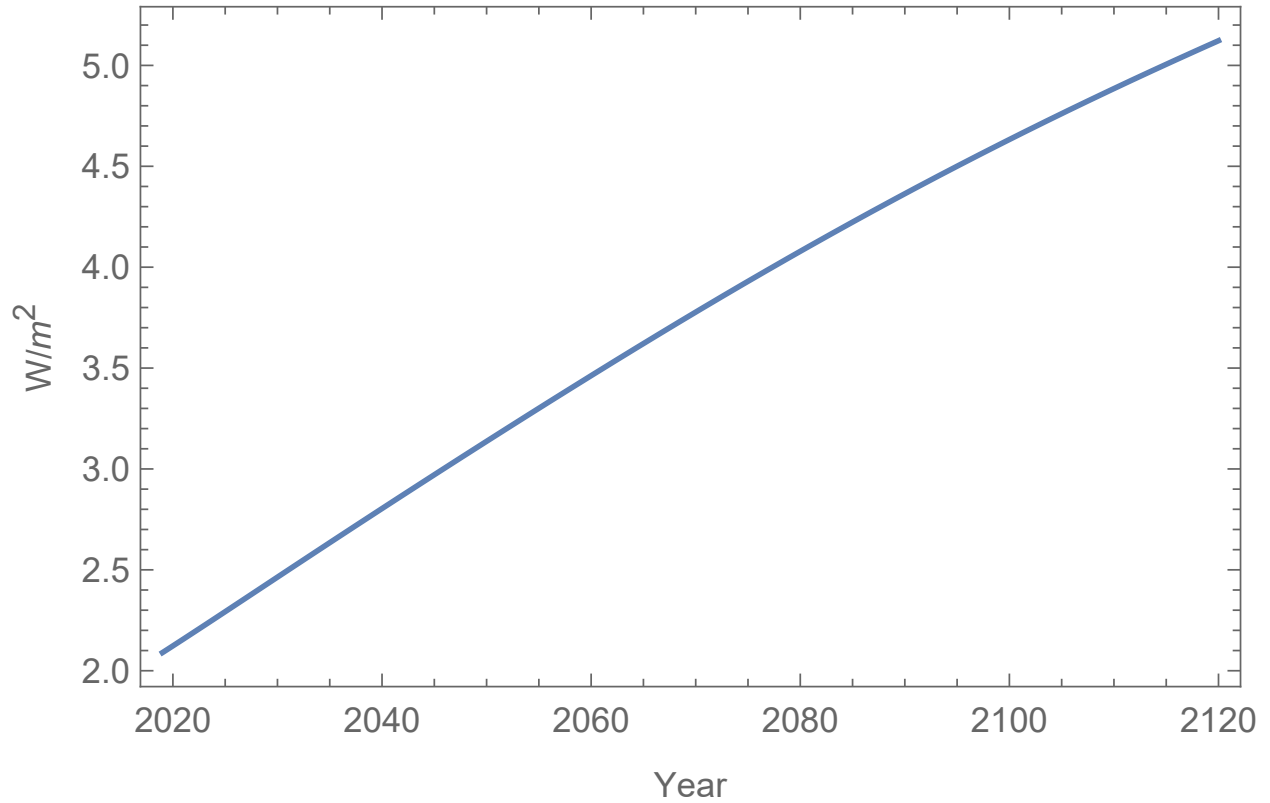


Figure 5.4: Extrapolation of CO₂ radiative forcing from 2019 to 2120.

Figure 5.7 shows 21 cases of extrapolated global surface mean temperature from 2019 to 2120 with the maximum marginal posterior probability case plotted in red. Note that what is shown is relative to year 2019's value.

5.5 Cumulative Distribution Function for 98 Samples

The cumulative probability distribution for the increase in τ over its input value at future year 2100 is plotted in figure 5.8.

Figure 5.8 shows the cumulative distribution function for 98 samples of extrapolated global surface mean temperature from 2019 to 2100. However, it is the increase over year 2019's value. In the context of this analysis, the probability a warming increase over 2019 level of less than 1 °C with extrapolation of historical radiative forcing is less than 1%. In the same context, there is a 50% probability of at least a 2.9 °C increase from 2019 to 2100.

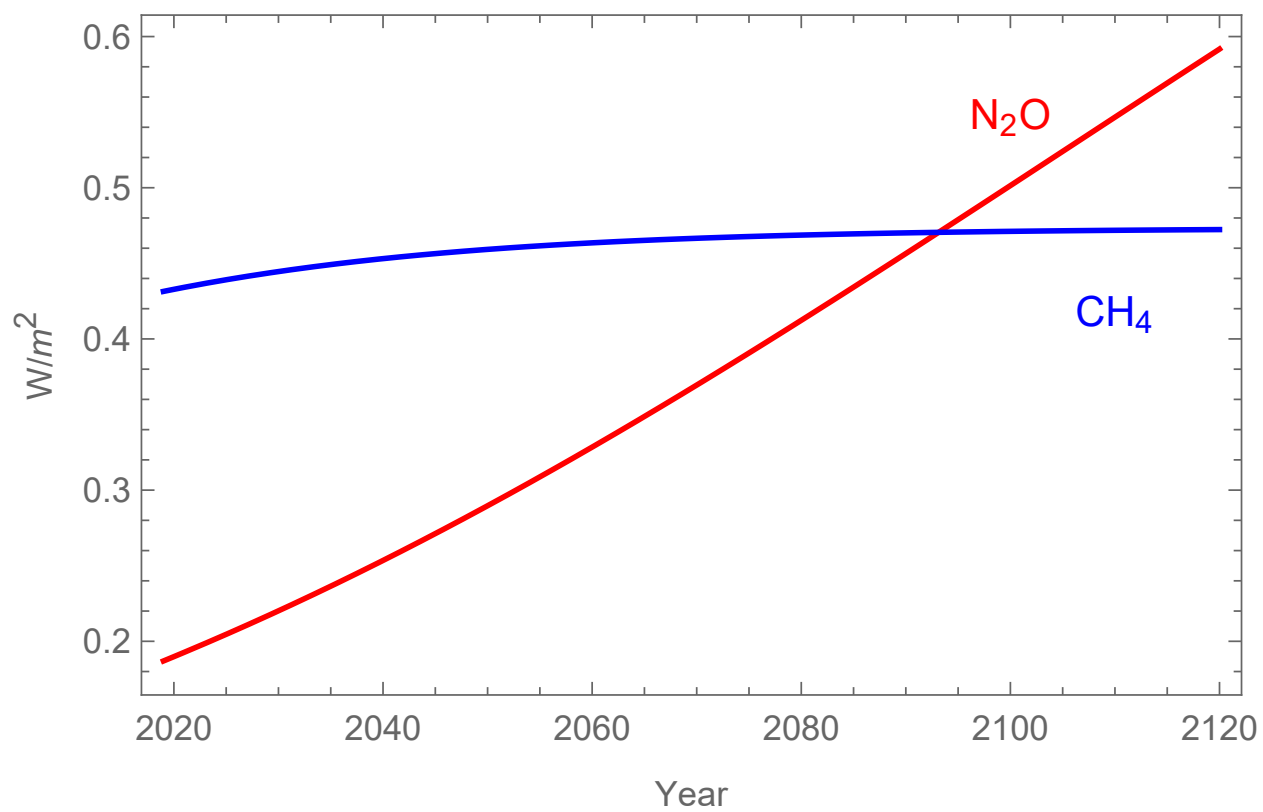


Figure 5.5: Extrapolation of CH_4 and N_2O radiative forcing from 2019 to 2120.

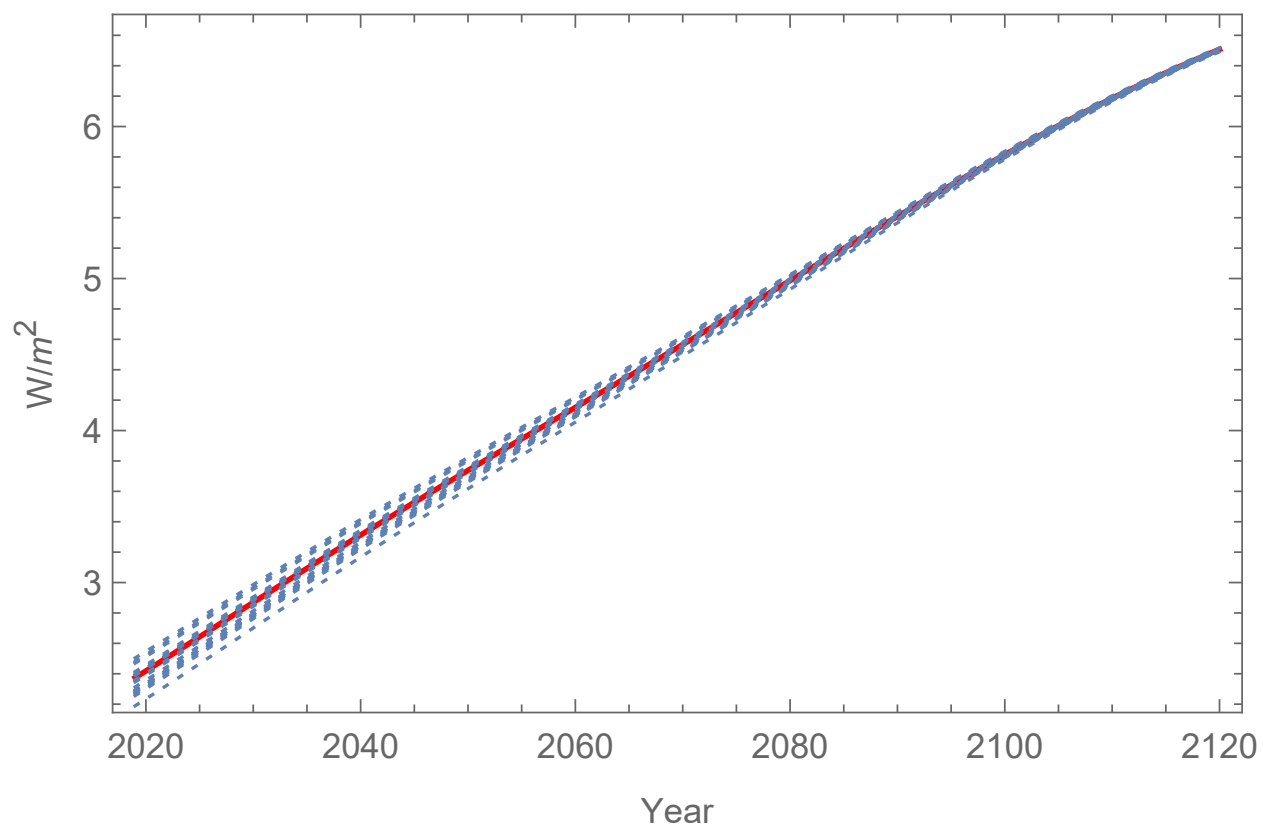


Figure 5.6: The first 20 samples of extrapolation of total radiative forcing from 2019 to 2120 with the maximum joint probability case in red.

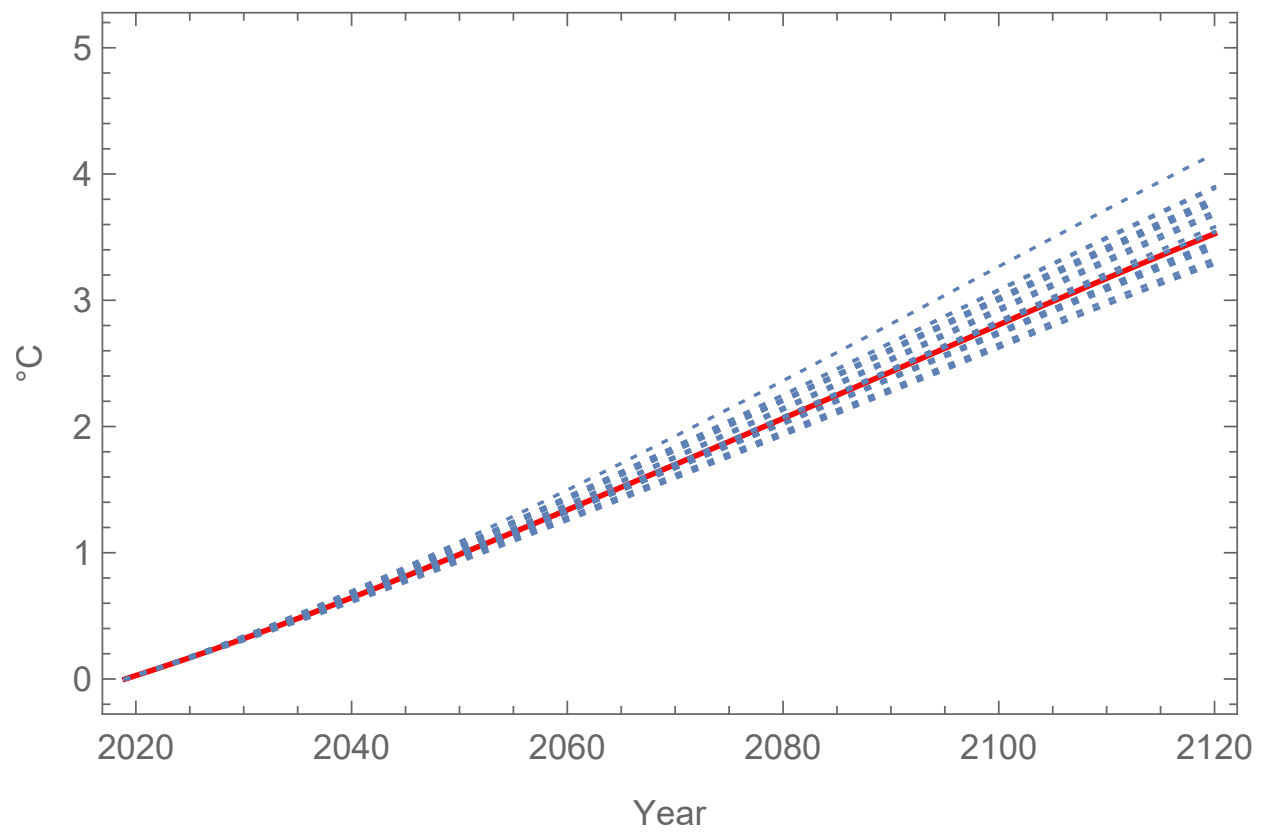


Figure 5.7: The first 20 samples of extrapolation of global mean temperature from 2019 to 2120 with the maximum joint probability case in red.

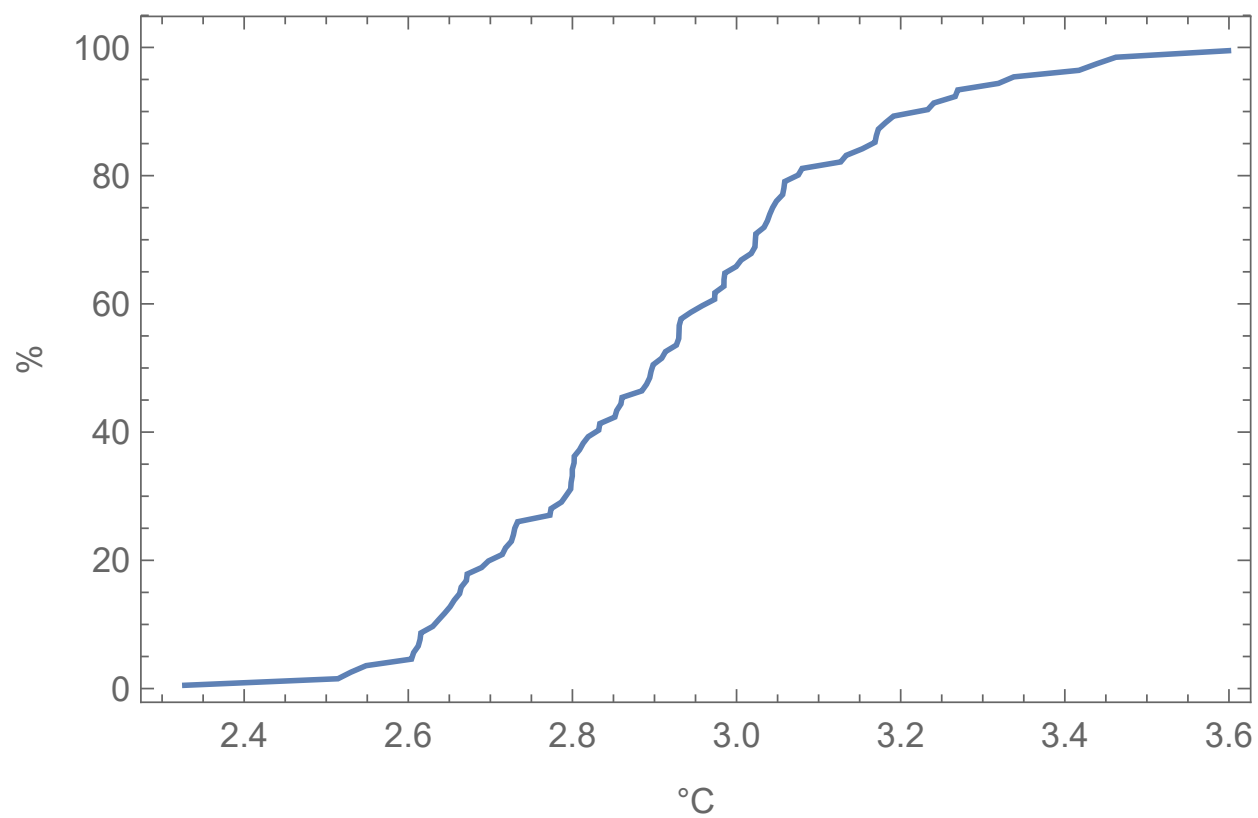


Figure 5.8: Cumulative distribution function for 98 samples of extrapolation of global surface mean temperature to 2100 relative to year 2019 temperature.

CHAPTER 6

CONCLUSIONS AND FUTURE WORK

In this work, combining data and climate physics together to analyze the response of temperature to the variation of radiative forcing allowed derivation of an analytic formula for a trivariate probability distribution for three important parameters influencing solutions of a global heat balance equation. Thanks to removing the natural transients out from the global mean temperature observations, it is possible to use this efficient yet effective model to analyze uncertainty of future global warming. It is concluded that if no measures are taken, then the goal of Paris Agreement has a very low probability of being accomplished.

Compared to simpler probability ranges for climate sensitivity λ in W/m^2 or equilibrium climate sensitivity in $^{\circ}\text{C}$, this trivariate probability distribution has the advantage of being able to provide rapid feedback on extrapolations of global warming, which is particularly useful when used in human participant simulations of international negotiation on carbon emissions policies [6].

That the adjustable part of radiative forcing extrapolates to becoming less negative implies that global warming would continue even if the sum of all other contributions to radiative forcing were held constant. Inclusion here of c_{reg} in the probability distribution used for extrapolations is thus appropriate. The thermal inertia timescale $c_{th}\lambda$ is comparable to an economic discounting timescale (e.g. about 40 years in Bei's work). This is significant when the type of analysis presented here is used with an integrated assessment model. It allows the exploration of uncertainties in how long it takes to approach a thermal equilibrium, not just what the value of the equilibrium ends up being.

In addition to the correlations between λ , c_{th} , and c_{reg} in the results in Chapter 4 (c.f. figure 4.3) an interesting feature of the trivariate probability distribution is an extended tail at high values of these parameters that is evident in figure 4.2. This made it difficult to

make a simpler trivariate normal approximation due justice to this potentially important feature of the result.

However, this work needs more careful analysis based on the evolving analyses of historical contributions to radiative forcing. Particular attention is needed to developments in the literature on radiative shielding from tropospheric aerosols. It could also be interesting to examine how results would depend on the length of time-series data streams used for calibrating the adjustable parameters in the global heat balance equation. Also, in the future, there is need to consider the warming results under different carbon emission policies. In particular, more work on stability of potential international agreements on climate change policy done by Bei Yang could make good use of the results presented in this thesis [12].

This work will also be helpful for a series of planned human participant simulation exercises in an educational context and possible extensions to related research aimed at shedding more light on the interplay between natural science, economics, and the how members of the climatologically important species *Homo sapiens* reacts to systematically organized information about that interplay.

CHAPTER 7

REFERENCES

- [1] *Climate Change 2013: The Physical Science Basis*. Cambridge University Pr., 2014. [Online]. Available: https://www.ebook.de/de/product/22180258/climate_change_2013_the_physical_science_basis.html
- [2] M.-D. V., P. Zhai, A. Pirani, S.L.Connors, C. Péan, S. Berger, N. Caud, Y. Chen, L. Goldfarb, M. Gomis, M. Huang, K. Leitzell, E. Lonnoy, J.B.R.Matthews, T. Maycock, T. Waterfield, O. Yelekçi, R. Yu, and B. Zhou, “Ipcc, 2021: Climate change 2021: The physical science basis. contribution of working group i to the sixth assessment report of the intergovernmental panel on climate change,” Cambridge University Press. InPress., Tech. Rep., 2021.
- [3] P. Friedlingstein, M. O'Sullivan, M. W. Jones, R. M. Andrew, J. Hauck, A. Olsen, G. P. Peters, W. Peters, J. Pongratz, S. Sitch, C. L. Quéré, J. G. Canadell, P. Ciais, R. B. Jackson, S. Alin, L. E. O. C. Aragão, A. Arneeth, V. Arora, N. R. Bates, M. Becker, A. Benoit-Cattin, H. C. Bittig, L. Bopp, S. Bultan, N. Chandra, F. Chevallier, L. P. Chini, W. Evans, L. Florentie, P. M. Forster, T. Gasser, M. Gehlen, D. Gilfillan, T. Gkritzalis, L. Gregor, N. Gruber, I. Harris, K. Hartung, V. Haverd, R. A. Houghton, T. Ilyina, A. K. Jain, E. Joetzjer, K. Kadono, E. Kato, V. Kitidis, J. I. Korsbakken, P. Landschützer, N. Lefèvre, A. Lenton, S. Lienert, Z. Liu, D. Lombardozzi, G. Marland, N. Metzl, D. R. Munro, J. E. M. S. Nabel, S.-I. Nakaoka, Y. Niwa, K. O'Brien, T. Ono, P. I. Palmer, D. Pierrot, B. Poulter, L. Resplandy, E. Robertson, C. Rödenbeck, J. Schwinger, R. Séférian, I. Skjelvan, A. J. P. Smith, A. J. Sutton, T. Tanhua, P. P. Tans, H. Tian, B. Tilbrook, G. van der Werf, N. Vuichard, A. P. Walker, R. Wankhoff, A. J. Watson, D. Willis, A. J. Wiltshire, W. Yuan, X. Yue, and S. Zaehle, “Global carbon budget 2020,” vol. 12, no. 4, pp. 3269–3340, dec 2020.
- [4] C. E. Singer and H. von Brevern, “Uranium price versus cumulative use,” vol. 176, no. 2, pp. 227–237, nov 2011.
- [5] C. Singer, T. Milligan, and T. Rethinaraj, “How china’s options will determine global warming,” *Challenges*, vol. 5, no. 1, pp. 1–25, dec 2013.
- [6] C. Singer and L. Matchett, “Climate action gaming experiment: Methods and example results,” *Challenges*, vol. 6, no. 2, pp. 202–228, sep 2015.
- [7] J. W. Bae, C. E. Singer, and K. D. Huff, “Synergistic spent nuclear fuel dynamics within the european union,” vol. 114, pp. 1–12, jul 2019.

- [8] J. Zhou, H. Abdel-Khalik, P. Talbot, and C. Rabiti, “A hybrid energy system workflow for energy portfolio optimization,” vol. 14, no. 15, p. 4392, jul 2021.
- [9] J. Zhou, “An optimization workflow for energy portfolio in integrated energy systems,” 2021.
- [10] C. E. Singer, T. S. G. Rethinaraj, S. Addy, D. Durham, M. Isik, M. Khanna, B. Kuehl, J. Luo, W. Quimio, K. Rajendran, D. Ramirez, J. Qiang, J. Scheffran, T. N. Tiouririne, and J. Zhang, “Probability distributions for carbon emissions and atmospheric response,” *Climatic Change*, vol. 88, no. 3-4, pp. 309–342, apr 2008.
- [11] R. M. Cooke and B. Wielicki, “Probabilistic reasoning about measurements of equilibrium climate sensitivity: combining disparate lines of evidence,” vol. 151, no. 3-4, pp. 541–554, nov 2018.
- [12] B. Yang, “Economic analysis of international climate cooperation,” Ph.D. dissertation, University of Illinois at Urbana-Champaign, 2021. [Online]. Available: <http://hdl.handle.net/2142/110488>
- [13] A. H. MacDougall, T. L. Frölicher, C. D. Jones, J. Rogelj, H. D. Matthews, K. Zickfeld, V. K. Arora, N. J. Barrett, V. Brovkin, F. A. Burger, M. Eby, A. V. Eliseev, T. Hajima, P. B. Holden, A. Jeltsch-Thömmes, C. Koven, N. Mengis, L. Menviel, M. Michou, I. I. Mokhov, A. Oka, J. Schwinger, R. Séférian, G. Shaffer, A. Sokolov, K. Tachiiri, J. Tjiputra, A. Wiltshire, and T. Ziehn, “Is there warming in the pipeline? a multi-model analysis of the zero emissions commitment from CO₂,” vol. 17, no. 11, pp. 2987–3016, jun 2020.
- [14] B. Vega-Westhoff, R. L. Sriver, C. A. Hartin, T. E. Wong, and K. Keller, “Impacts of observational constraints related to sea level on estimates of climate sensitivity,” vol. 7, no. 6, pp. 677–690, jun 2019.
- [15] C. A. Hartin, P. Patel, A. Schwarber, R. P. Link, and B. P. Bond-Lamberty, “A simple object-oriented and open-source model for scientific and policy analyses of the global climate system – hector v1.0,” vol. 8, no. 4, pp. 939–955, apr 2015.
- [16] G. Foster and S. Rahmstorf, “Global temperature evolution 1979–2010,” vol. 6, no. 4, p. 044022, jan 2011.
- [17] J. L. Lean and D. H. Rind, “How natural and anthropogenic influences alter global and regional surface temperatures: 1889 to 2006,” *Geophysical Research Letters*, vol. 35, no. 18, sep 2008.
- [18] J. L. Lean and D. H. Rind, “How will earth's surface temperature change in future decades?” *Geophysical Research Letters*, vol. 36, no. 15, pp. n/a–n/a, aug 2009.
- [19] D. H. Douglass, “Climate forcing by the volcanic eruption of mount pinatubo,” *Geophysical Research Letters*, vol. 32, no. 5, 2005.

- [20] C. M. Ammann and P. Naveau, “A statistical volcanic forcing scenario generator for climate simulations,” vol. 115, no. D5, mar 2010.
- [21] L. Cheng, K. E. Trenberth, J. Fasullo, T. Boyer, J. Abraham, and J. Zhu, “Improved estimates of ocean heat content from 1960 to 2015,” *Science Advances*, vol. 3, no. 3, p. e1601545, mar 2017.
- [22] T. J. Osborn, P. D. Jones, D. H. Lister, C. P. Morice, I. R. Simpson, J. P. Winn, E. Hogan, and I. C. Harris, “Land surface air temperature variations across the globe updated to 2019: The CRUTEM5 data set,” vol. 126, no. 2, jan 2021.
- [23] D. CHAN and P. Huybers, “Identifying and correcting the world war 2 warm anomaly in sea surface temperature measurements,” aug 2020.
- [24] A. P. Schurer, G. C. Hegerl, and S. P. Obrochta, “Determining the likelihood of pauses and surges in global warming,” vol. 42, no. 14, pp. 5974–5982, jul 2015.
- [25] A. P. Sokolov, P. H. Stone, C. E. Forest, R. Prinn, M. C. Sarofim, M. Webster, S. Paltsev, C. A. Schlosser, D. Kicklighter, S. Dutkiewicz, J. Reilly, C. Wang, B. Felzer, J. M. Melillo, and H. D. Jacoby, “Probabilistic forecast for twenty-first-century climate based on uncertainties in emissions (without policy) and climate parameters,” vol. 22, no. 19, pp. 5175–5204, oct 2009.
- [26] A. L. Marten, “Transient temperature response modeling in IAMs: The effects of over simplification on the SCC,” vol. 5, no. 1, oct 2011.
- [27] W. Nordhaus, *Warming the world : economic models of global warming*. Cambridge, Mass: MIT Press, 2000.
- [28] C. Hope, “The marginal impact of co2 from page2002: An integrated assessment model incorporating the ipcc’s five reasons for concern,” *Integrated Assessment*, vol. 6, pp. 19–56, 01 2006.
- [29] C. Ding, “Global heat balance without and with solar radiation management,” M.S. thesis, University of Illinois at Urbana Champaign, 2018.
- [30] C. M. Meure, D. Etheridge, C. Trudinger, P. Steele, R. Langenfelds, T. van Ommen, A. Smith, and J. Elkins, “Law dome CO₂, CH₄ and n₂o ice core records extended to 2000 years BP,” *Geophysical Research Letters*, vol. 33, no. 14, 2006.
- [31] J. H. Butler and S. A. Montzka, “The noaa annual greenhouse gas index (aggi),” Dec. 2020. [Online]. Available: <https://www.esrl.noaa.gov/gmd/aggi/aggi.html>
- [32] D. M. Etheridge, L. P. Steele, R. L. Langenfelds, R. J. Francey, J.-M. Barnola, and V. I. Morgan, “Natural and anthropogenic changes in atmospheric CO₂ over the last 1000 years from air in antarctic ice and firn,” *Journal of Geophysical Research: Atmospheres*, vol. 101, no. D2, pp. 4115–4128, feb 1996.

- [33] C. M. Meure, “The natural and anthropogenic variations of carbon dioxide, methane and nitrous oxide during the holocene from ice core analysis,” Ph.D. dissertation, University of Melbourne, 2004.
- [34] D. F. Ferretti, “Unexpected changes to the global methane budget over the past 2000 years,” *Science*, vol. 309, no. 5741, pp. 1714–1717, sep 2005.
- [35] D. M. Etheridge, L. P. Steele, R. J. Francey, and R. L. Langenfelds, “Atmospheric methane between 1000 a.d. and present: Evidence of anthropogenic emissions and climatic variability,” *Journal of Geophysical Research: Atmospheres*, vol. 103, no. D13, pp. 15 979–15 993, jul 1998.
- [36] P. T. Ed Dlugokencky, “Noaa/esrl (www.esrl.noaa.gov/gmd/ccgg/trends/).”
- [37] M. Bickel, M. Ponater, L. Bock, U. Burkhardt, and S. Reineke, “Estimating the effective radiative forcing of contrail cirrus,” vol. 33, no. 5, pp. 1991–2005, mar 2020.
- [38] A. Schmidt, M. J. Mills, S. Ghan, J. M. Gregory, R. P. Allan, T. Andrews, C. G. Bardeen, A. Conley, P. M. Forster, A. Gettelman, R. W. Portmann, S. Solomon, and O. B. Toon, “Volcanic radiative forcing from 1979 to 2015,” *Journal of Geophysical Research: Atmospheres*, vol. 123, no. 22, pp. 12 491–12 508, nov 2018.
- [39] E. Venzke, “Global volcanism program, 2013. volcanoes of the world, v. 4.9.1.” [Online]. Available: <https://doi.org/10.5479/si.GVP.VOTW4-2013>
- [40] S. Carn, “Multi-satellite volcanic sulfur dioxide l4 long-term global database v4,” 2021.
- [41] K. Wolter and M. S. Timlin, “El niño/southern oscillation behaviour since 1871 as diagnosed in an extended multivariate ENSO index (MEI.ext),” *International Journal of Climatology*, vol. 31, no. 7, pp. 1074–1087, apr 2011.
- [42] K. Wolter and M. Timlin, “Monitoring enso in coads with a seasonally adjusted principal component index.” proc. of the 17th Climate Diagnostics Workshop, Norman, OK, NOAA/NMC/CAC, NSSL, Oklahoma Clim. Survey, CIMMS and the School of Meteor., Univ. of Oklahoma, 52-57.
- [43] K. Wolter and M. S. Timlin, “Measuring the strength of ENSO events: How does 1997/98 rank?” vol. 53, no. 9, pp. 315–324, sep 1998.
- [44] K. Wolter and M. S. Timlin, “Multivariate enso index (mei).” [Online]. Available: <https://psl.noaa.gov/enso/mei.old/table.html>
- [45] SORCE, “Historical total solar irradiance reconstruction, time series,” solar Radiation and Climate Experiment,, University of Colorado, Boulder, Laboratory for Atmospheric and Space Physics,TIM Daily,accessed June 18, 2021. [Online]. Available: https://lasp.colorado.edu/lisird/latiis/dap/historical_tsi.csv?&time=1610-01-01T00:00:00.000Z&time=2021-10-28T19:44:00.000Z

- [46] LASP, “Lasp interactive solar irradiance datacenter. 2021. historical total solar irradiance reconstruction, time series.” [Online]. Available: https://lasp.colorado.edu/lisird/latis/dap/historical_tsi.csv?&time\>=1610-01-01T00:00:00.000Z&time\<=2021-09-07T23:10:00.000Z
- [47] K. G. McCracken, J. Beer, F. Steinhilber, and J. Abreu, “A phenomenological study of the cosmic ray variations over the past 9400 years, and their implications regarding solar activity and the solar dynamo,” *Solar Physics*, vol. 286, no. 2, pp. 609–627, apr 2013.
- [48] C.-J. Wu, N. A. Krivova, S. K. Solanki, and I. G. Usoskin, “Solar total and spectral irradiance reconstruction over the last 9000 years,” vol. 620, p. A120, dec 2018.
- [49] N. Loeb and NCAR., “The climate data guide: Ceres ebaf: Clouds and earth’s radiant energy systems (ceres) energy balanced and filled (ebaf).” [Online]. Available: https://ceres.larc.nasa.gov/documents/TSIdata/CERES_EBAF_Ed2.8_DailyTSI.txt
- [50] R. L. Miller, G. A. Schmidt, L. S. Nazarenko, N. Tausnev, S. E. Bauer, A. D. DelGenio, M. Kelley, K. K. Lo, R. Ruedy, D. T. Shindell, I. Aleinov, M. Bauer, R. Bleck, V. Canuto, Y. Chen, Y. Cheng, T. L. Clune, G. Faluvegi, J. E. Hansen, R. J. Healy, N. Y. Kiang, D. Koch, A. A. Lacis, A. N. LeGrande, J. Lerner, S. Menon, V. Oinas, C. P. García-Pando, J. P. Perlwitz, M. J. Puma, D. Rind, A. Romanou, G. L. Russell, M. Sato, S. Sun, K. Tsigaridis, N. Unger, A. Voulgarakis, M.-S. Yao, and J. Zhang, “CMIP5 historical simulations (1850-2012) with GISS ModelE2,” *Journal of Advances in Modeling Earth Systems*, vol. 6, no. 2, pp. 441–478, jun 2014.
- [51] N. Bellouin, W. Davies, K. P. Shine, J. Quaas, J. Mülmenstädt, P. M. Forster, C. Smith, L. Lee, L. Regayre, G. Brasseur, N. Sudarchikova, I. Bouarar, O. Boucher, and G. Myhre, “Radiative forcing of climate change from the copernicus reanalysis of atmospheric composition,” vol. 12, no. 3, pp. 1649–1677, jul 2020.
- [52] U. Cubasch, D. Wuebbles, D. Chen, M. Facchini, D. Frame, N. Mahowald, and J.-G. Winther, “Introduction. in: Climate change 2013: The physical science basis,” Contribution of Working Group I to the Fifth Assessment Report of the Intergovernmental Panel on Climate Change [Stocker, T.F., D. Qin, G.-K. Plattner, M. Tignor, S.K. Allen, J. Boschung, A. Nauels, Y. Xia, V. Bex and P.M. Midgley (eds.)]. Cambridge University Press, Cambridge, United Kingdom and New York, NY, USA., Tech. Rep., 2013.
- [53] D. T. Shindell, “Inhomogeneous forcing and transient climate sensitivity,” *Nature Climate Change*, vol. 4, no. 4, pp. 274–277, mar 2014.
- [54] N. J. L. Lenssen, G. A. Schmidt, J. E. Hansen, M. J. Menne, A. Persin, R. Ruedy, and D. Zyss, “Improvements in the GISTEMP uncertainty model,” *Journal of Geophysical Research: Atmospheres*, vol. 124, no. 12, pp. 6307–6326, jun 2019.
- [55] G. Team, “Giss surface temperature analysis (gistemp), version 4.” 2021, dataset accessed 2021-08-22. [Online]. Available: <https://data.giss.nasa.gov/gistemp/>

- [56] E. Hawkins, P. Ortega, E. Suckling, A. Schurer, G. Hegerl, P. Jones, M. Joshi, T. J. Osborn, V. Masson-Delmotte, J. Mignot, P. Thorne, and G. J. van Oldenborgh, “Estimating changes in global temperature since the preindustrial period,” vol. 98, no. 9, pp. 1841–1856, sep 2017.
- [57] J. Hansen, M. Sato, R. Ruedy, P. Kharecha, A. Lacis, R. Miller, L. Nazarenko, K. Lo, G. A. Schmidt, G. Russell, I. Aleinov, S. Bauer, E. Baum, B. Cairns, V. Canuto, M. Chandler, Y. Cheng, A. Cohen, A. D. Genio, G. Faluvegi, E. Fleming, A. Friend, T. Hall, C. Jackman, J. Jonas, M. Kelley, N. Y. Kiang, D. Koch, G. Labow, J. Lerner, S. Menon, T. Novakov, V. Oinas, J. Perlwitz, J. Perlwitz, D. Rind, A. Romanou, R. Schmunk, D. Shindell, P. Stone, S. Sun, D. Streets, N. Tausnev, D. Thresher, N. Unger, M. Yao, and S. Zhang, “Climate simulations for 1880–2003 with GISS modelE,” vol. 29, no. 7-8, pp. 661–696, jun 2007.
- [58] W. Wei, *Time series analysis : univariate and multivariate methods*. Boston: Pearson Addison Wesley, 2006.
- [59] G. E. Box and G. C. Tiao, *Bayesian Inference in Statistical Analysis*. John Wiley & Sons, Inc., apr 1992.
- [60] C. D. Jones, T. L. Frölicher, C. Koven, A. H. MacDougall, H. D. Matthews, K. Zickfeld, J. Rogelj, K. B. Tokarska, N. P. Gillett, T. Ilyina, M. Meinshausen, N. Mengis, R. Séférian, M. Eby, and F. A. Burger, “The zero emissions commitment model inter-comparison project (ZECMIP) contribution to c4mip: quantifying committed climate changes following zero carbon emissions,” vol. 12, no. 10, pp. 4375–4385, oct 2019.

APPENDIX A

SOLUTION OF GLOBAL HEAT BALANCE EQUATION

From the global heat balance equation, we have

$$c_{th} \frac{d\tau}{dt} = F - \frac{\tau}{\lambda} \quad (\text{A.1})$$

Divide both sides by c_{th} ,

$$\frac{d\tau}{dt} = \frac{F}{c_{th}} - \frac{\tau}{\lambda c_{th}} \quad (\text{A.2})$$

$$\frac{d\tau}{dt} + \mu\tau = \frac{F}{c_{th}} \quad (\text{A.3})$$

Here, $\mu = \frac{1}{\lambda c_{th}}$.

Rewrite the left side of above equation,

$$e^{-\mu t} d(e^{\mu t} \tau) = \frac{F}{c_{th}} \quad (\text{A.4})$$

Assume a constant F_i in year i , then for each year i , the contribution τ_i is as follows:

$$d(e^{\mu t} \tau_i) = \left(\frac{F_i}{c_{th}}\right) e^{\mu t}, \quad \text{for } i = 1, \dots, 270 \quad (\text{A.5})$$

since the contribution from F_i to τ is 0 before year i .

$$e^{\mu t} \tau_i = \left(\frac{F_i}{c_{th}}\right) \int_{t_i}^t e^{\mu t} dt = \lambda F_i (e^{\mu t} - e^{\mu t_i}) \quad (\text{A.6})$$

Thus, during year i , we have

$$\tau_i = \lambda F_i (1 - e^{-\mu(t-t_i)}) \quad (\text{A.7})$$

Half way into year t_i , we have $t - t_i = 0.5$, so,

$$\tau_i(t_i + 0.5) = \lambda F_i (1 - e^{-\frac{\mu}{2}}) \quad (\text{A.8})$$

At the beginning of the year after year t_i , we would have

$$\tau_{i+1} = \lambda F_i (1 - e^{-\mu/2}) \quad (\text{A.9})$$

From then on, the contribution from F_i satisfies the equation

$$c_{th} \frac{d\tau}{dt} = \frac{-\tau}{\lambda} \quad (\text{A.10})$$

, which gives $d(e^{\mu t} \tau_i) = 0$.

Solve this with initial condition

$$\tau_{i+1} = \lambda F_i (1 - e^{-\mu/2}) \quad (\text{A.11})$$

at $t = t_i$ and evaluate the result at each $t = t_{i+0.5}$ for $i=1,2,\dots,269$.

It is assumed that all the previous years' radiative forcing effects on the current year temperature τ_i decays exponentially with time. Thus, the second term in the equation below add the cumulative exponentially decay radiative forcing effects on τ_i from years before it. For τ_1 , it is zero at Julian year 1750. From year 1751 to 2019, we have

$$\tau_i = \lambda(1 - e^{-\mu/2})F_i + \beta \sum_{k=1}^{n-1} F_k e^{-(n-k)\mu} \quad \text{for } i = 2, \dots, 270 \quad (\text{A.12})$$

where $\beta = \lambda(1 - e^{-\mu})e^{-\mu/2}$.